Selective Membrane Transport Systems studied by Solid-State NMR Spectroscopy

Christian Ader

ISBN 978-90-393-5117-8

Doctoral thesis

Selective Membrane Transport Systems studied by Solid-State NMR Spectroscopy

Christian Ader

NMR Spectroscopy Research Group, Bijvoet Center for Biomolecular Research, Utrecht University, The Netherlands

September 2009

Financial support for the publication of this thesis was kindly provided by the Stiftung Stipendien Fonds des Verbandes der Chemischen Industrie e. V., Germany.

The cover picture shows the crystal structure of full-length KcsA (PDB ID 3EFF)

Printed by Klingel Gerhard Druckerei, Eisingen, Germany.

Selective Membrane Transport Systems studied by Solid-State NMR Spectroscopy

Selectieve Membraan Transportsystemen bestudeerd met Vaste Stof NMR Spectroscopie

(met een samenvatting in het Nederlands)

Proefschrift

ter verkrijging van der graad van doctor aan de Universiteit Utrecht op gezag van de rector magnificus, prof. dr. J.C. Stoof, ingevolge het besluit van het college voor promoties in het openbaar te verdedigen op maandag 21 september 2009 des middags te 12.45 uur

door

Christian Ader

geboren op 7 januari 1981 te Pforzheim, Duitsland

Promotor: Prof. dr. M. Baldus

Table of contents

Chapter 1

General Introduction

Christian Ader

Bijvoet Center for Biomolecular Research, Utrecht University, The Netherlands

Membrane-associated proteins

Biological membranes are a cornerstone of life. They are established by lipid bilayers and separate cells and cell organelles acting as very efficient insulators. However, membranes do generally not act as firm barriers but are heavily involved in the compartmentation, direction and organization of countless cellular processes. Membrane-associated proteins provide a powerful arsenal of molecular machinery to functionalize membranes (**Fig. 1**). Thus, the lipid and protein compositions strongly depend on the biological function of the membrane and are highly regulated. Many enzymatic reactions as fundamental as carbon fixation and ATP synthesis take place in a membrane setting and signal transduction depends on bilayer spanning receptors that pass information from one compartment to the other. Moreover, membrane proteins are integral to molecular trafficking, cell-cell recognition, cell adhesion and fulfill architectural functions as scaffolds and part of the cytoskeleton. Other than many cytosolic proteins, membrane-associated proteins reside in a highly anistropic environment at the interface of the aqueous cytosole, the ionic region of the membrane surface, and the hydrophobic bilayer core. To account for these dielectric differences, the molecular structure of membrane proteins has evolved in a very specialized manner.

Detailed knowledge of the molecular structure provides insight into protein function and contributes to research in such different fields as molecular biology, nano-technology, pharmacy, and food science. The large majority of protein structures published and deposited in the Protein Data Bank (PDB) of the Research Collaboratory for Structural Bioinformatics (RCSB)[1] was solved by x-ray crystallographic techniques and solution-state Nuclear Magnetic Resonance (NMR) spectroscopy. These methods rely on the availability of protein crystals and protein solutions, respectively, and therefore require the lipid bilayer to be replaced by detergent molecules if membrane proteins are under investigation. The detergent-solubilized state of membrane proteins is often an insufficient mimicry of the native environment leading to instable proteins and eventually to a lack of structural information or the detection of structural artifacts. About one quarter of the human genome encodes membrane proteins[2] and 60% of the available pharmaceuticals target membrane proteins.[3] This reflects their striking functional importance and diversity sketched above. On the other hand, at present less than 1% of the proteins listed in the Protein Data Bank are natively membrane-associated (for current information refer to refs. 4, 5). This highlights the need for methodological development in both membrane protein crystallization and NMR spectroscopy. Specialized techniques like two-dimensional protein crystallization, electron-microscopy and solid-state NMR spectroscopy allow for the structural characterization of membrane proteins in a native lipid setting. The protein of interest is recombinantly expressed, purified and subsequently reconstituted in defined lipid bilayers. Solid-state NMR spectroscopy provides the advantage that it also grants access to dynamical information in addition to structural constraints. Moreover, this method gives great freedom in terms of sample preparation. Many parameters like ionic strength, pH, temperature, lipid composition and the presence of effector molecules such as ligands can be adjusted to match functionally relevant

conditions and to study structure-function relations in complex membrane systems closely mimicking the cellular setting.

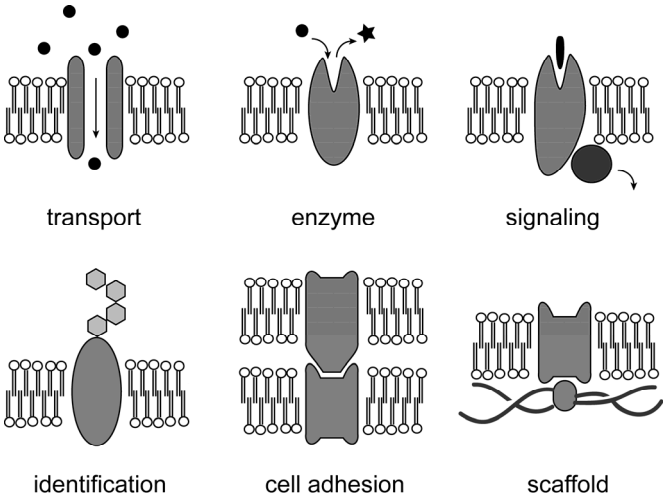

Figure 1. Classification of cellular functions executed by membrane proteins including cellular transport, enzymatic catalysis, signal recognition and transduction, cell-cell recognition and molecular identification, cell adhesion and contact as well as scaffold for example providing attachment to cytoskeleton and extracellular matrix.

Solid-state NMR spectroscopy

The term "solid-state" may be misleading at first view. Lipid bilayers exist depending on the temperature as a liquid-crystalline or gel phase. Thus, to some extend even high but anisotropic molecular mobility can be expected. The advantages of solid-state (ss)NMR spectroscopy over other biophysical techniques employed for membrane investigations are the lack of a size restriction for the system to be investigated, the ability to study samples without the introduction of artificial chemical modifications in an adjustable environment, and the option to use samples that are not highly ordered or aligned, if magic angle spinning (MAS)[6,7] is performed.

Expression, purification, and reconstitution of membrane proteins follow diverse and delicate protocols (for review see e.g. ref. 8). Labeling with stable isotopes such as ^{13}C and ^{15}N is essential for a detailed characterization of the protein by ssNMR spectroscopy. This is achieved by feeding isotope enriched sugars and ammonium salts as exclusive nutrition source of the bacteria expressing the protein. For larger membrane proteins specific or reverse labeling approaches are often used to reduce spectral ambiguities.[9-11] Generally, over-expressed membrane proteins have to be solubilized from inclusion bodies or membrane fractions employing detergents. Recently, also in vitro expression systems are developed focusing on transmembrane proteins.[8] After purification of the solubilized membrane protein, it may be reconstituted in lipid bilayers. In most present protocols, this occurs spontaneously if proper lipid mixtures are provided and the detergent is removed. As an example the purification and reconstitution protocol for the chimeric potassium channel KcsA-Kv1.3 is sketched in **Figure 2** and will be briefly described following previous publications.[12-14] The channel is expressed with a polyhistidine-tag in *Escherichia coli* using a pQE32 expression construct. The minimum medium is supplemented by ^{13}C labeled glucose, ^{15}N ammonium sulfate, and necessary antibiotics. The cells are disrupted with a French Press and

the membrane-bound protein is solubilized with n-decyl-β-D-maltopyranoside. After purification on Ni^{2+}-nitrotriacetic acid agarose and concentration, the buffer is exchanged as desired using a desalting column. Liposomes prepared in the same buffer are added usually in a 100:1 lipid-to-protein ratio and the suspension is incubated for two hours. Subsequently, adsorbent is added to remove the detergent. Before packing the proteoliposomes in magic angle spinning rotors for ssNMR they are pelleted by ultracentrifugation.

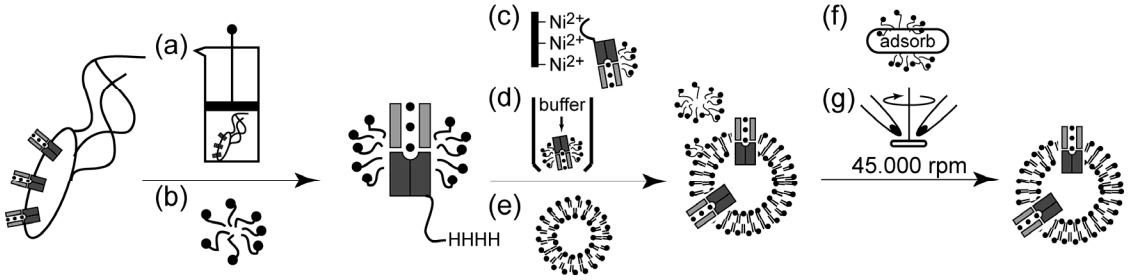

Figure 2. KcsA-Kv1.3 is expressed with a polyhistidine-tag in *Escherichia coli*. After disruption of the cells with a French Press (a), the potassium channel is solubilized from the membrane fraction by adding detergent (b). Purification proceeds via Ni^{2+}-nitrotriacetic acid agarose (c) and a desalting column for buffer exchange (d). Multilamellar vesicles are prepared and added for reconstitution (e). Detergent is removed by adsorbents (f) and proteoliposomes are pelleted by ultracentrifugation (g).

In order to gain insight into the secondary or tertiary structure of a peptide or protein by ssNMR spectroscopy, similar to liquid-state NMR structure determination the first step is the spectral assignment. This means that the observed spectral signals have to be identified and attributed to the spins expected for the molecule under investigation. The NMR spectra of randomly oriented molecules in the solid phase are extensively broadened by anisotropic interactions. Therefore, macroscopically oriented systems and site-specific single or pair-wise isotope labeling has frequently been employed for the measurement of intermolecular distances and torsion angles in membrane proteins and their natural ligands.[15,16] The combination of magic angle spinning (MAS), radio frequency decoupling schemes, and ultrahigh magnetic fields, however, enables high resolution for solid-state NMR spectroscopy on multiply or even uniformly isotope labeled proteins (**Fig. 3**).[13] While solution-state NMR structure determination relies heavily on proton (^{1}H) NMR spectroscopy, ^{1}H signals are still considerably broadened for solids due to strong homonuclear dipolar interactions that cannot be removed entirely by the methods mentioned above. Thus, dilute spins – especially ^{13}C and ^{15}N – play an essential role for the investigation of proteins. Frequently, heteronuclear magnetization transfer is obtained by cross polarization (CP)[17] matching the Hartmann-Hahn condition.[18] Two- and three-dimensional homonuclear and heteronuclear correlation spectra can be acquired under high-resolution condition and are used iteratively during the assignment process. Especially ^{13}C,^{13}C correlation experiments conducted under weak coupling conditions[19] and NCOCA and NCACB-type experiments[20] assist in the

identification of sequential correlations leading to the assignment of spin networks of adjacent residues in the polypeptide chain. Often, NMR signals originating from the lipid bilayer or from an unlabeled protein environment can complicate the ssNMR assignment. In such a case, double-quantum (^{13}C, ^{13}C) correlation methods which suppress natural abundance background signals by a factor of 10^4 can become mandatory. Furthermore, biochemical approaches such as selective forward or reverse labeling of certain amino acids and fragmentation of large proteins systems in functional domains can assist to reduce spectral ambiguities (compare **Chapter 4**). This leads to a simplified assignment process linking the NMR-active atoms within the protein to chemical shift values representing relative differences in resonance frequencies given in parts per million (ppm). The isotropic chemical shifts of peptide backbone atoms depend significantly on the torsion angles Φ and Ψ and, therefore, provide direct information on the local molecular conformation.[21] The observed chemical shifts are compared to average ('random coil') chemical shifts for backbone atoms and secondary structure information can be deduced from the respective differences. **Chapters 3** and **7** of this thesis provide two examples for the use of residue or amino acids specific assignments to elucidate secondary structural features of polypeptide chains in the solid phase. Chemical shifts are sensitive even to subtle changes in the local structure and chemical environment. Thus, the mapping of chemical shift perturbations induced for example by introducing a ligand helps to identify the interaction surface as shown for the binding of a synthetic pore blocker to a potassium channel (**Chapter 3**) and for the regulating effects of K^+ and lipids on potassium channel gating (**Chapters 4** and **5**). Moreover, the dependence of chemical shift and local protein structure can be combined with computational approaches predicting chemical shifts based on given structures in order to follow local rearrangements of proteins as a response to functional features or even to compute *ab initio* structures from isotropic chemical shifts.[22,23] This approach was utilized to characterize the different gating states of a potassium channel in a membrane setting (**Chapter 3**).

In order to elucidate the three-dimensional fold of a protein, internuclear distances and torsion angles have to be determined in strict analogy to solution-state NMR structure determination. Consecutively, families of molecular conformations are calculated using for example molecular dynamics simulated annealing procedures that obey the experimental data by introducing energetical penalty functions. The final structures are ranked based on their energies and general parameters like torsion angle distribution and molecular packing. An increasing number of techniques is available nowadays for ssNMR based structure determination, including chemical-shift selective recoupling techniques[24,25], broadband exploitation of $^{15}N/^{13}C$,^{13}C[26-28] or ^{1}H,^{1}H[29,30] dipolar couplings, and advanced preparative approaches like ^{19}F[31] or nitroxide spin labeling.[32] **Chapters 3** and **7** contain examples for structural distance constraints obtained by CHHC and NHHC experiments. In order to establish sufficient distance constraints for a reliable structure determination, ongoing spectroscopic improvements have to go along with efforts to streamline and automate the assignment process as well as structure determination and the development of specialized labeling and sample preparation techniques.

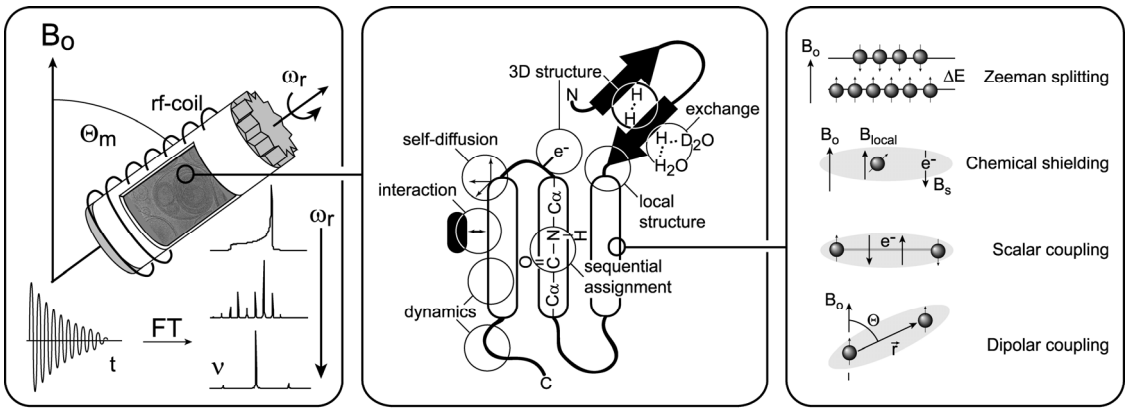

Figure 3. (a) Spinning of a solid-phase sample at an angle of 54.7º (Θ_m, magic angle) with respect to the static magnetic field B_o creates a favorable time dependence of anisotropic spin-interactions. If the spinning rate (ω_r) exceeds the largest couplings of the considered spin species (fast spinning limit), their influence is averaged out and "solution-like" spectra are obtained. (b) Cartoon illustration of a protein summarizing spectroscopic parameters accessible by ssNMR (for details see text). (c) NMR active nuclei reside in energetically distinct spin states (Zeeman splitting) in a static magnetic field B_o. Population differences result in a macroscopic magnetic moment whose time dependence represents the basic observable of NMR spectroscopy. States can be manipulated using radiofrequency pulses. Sin-spin interactions like chemical shielding, scalar- and dipolar coupling as well as spin-lattice interactions can be utilized to encode spatial and motional information in NMR spectra obtained by custom-tailored pulse sequences.

The topology of proteins and peptides reconstituted in lipid bilayers can be probed by ssNMR pulse schemes adapting the Goldman-Shen experiment.[33] In these experiments, signals arise from polarization transfer between selectively excited water or lipids and the protein. Important pathways for magnetization transfer are chemical exchange of fast exchanging protein protons and ^{1}H-^{1}H dipolar couplings.[34,35] The general notion of these experiments is that the magnetization transferred from to the protein over time, reports on solvent exposure, bilayer interaction, and accessibility of the membrane protein. In **Chapter 2**, such transfer efficiencies are compared for a series of α-helical transmembrane proteins and the magnetization transfer is approximated by a general diffusion model. In addition, ^{1}H, ^{2}H exchange experiments and the introduction of paramagnetic quenchers might help to probe protein topologies and molecular arrangements. Protonation states are frequently essential for structural and catalytical integrity of proteins. ssNMR chemical shifts can be used to follow local protonation states in the solid phase and even allows to probe pK_a values and their relation with protein function, as shown for the pH-sensor of the potassium channel KcsA-Kv1.3 in **Chapter 4**.

In addition to structural parameters, ssNMR spectroscopy provides information on molecular dynamics occurring on different timescales. Primarily, molecular motion is directly related to a reduction in anisotropic spin-spin interactions. Consequently, measurement of dipolar and quadrupolar interactions as well as chemical shift

anisotropy provides motional parameters obtained for individual atoms.[36] Internal motion in multiply labeled proteins can be assessed by multidimensional experiments encoding ^{15}N longitudinal relaxation rates[37], H-N and H-Cα dipolar couplings[38] or ^{15}N chemical shielding parameters.[39] The spin-lattice relaxation process is induced by local field fluctuation due to molecular motion and the associated relaxation rates (R1), therefore, provide a direct measure of site resolved dynamics. Results discussed in **Chapter 6** establish the use of ^{15}N R1's to study local mobility in membrane associated proteins as shown for the K^+ channel KcsA-Kv1.3. In the extreme case of molecular motion with frequencies much faster than the observed anistropic spin-spin interaction, the resonances of the respective spins are removed from dipolar based spectra typically obtained in ssNMR spectroscopy. Such dynamics are frequently found for unstructured parts of membrane proteins or protein aggregates. These segments can be investigated independently from the rigid protein domains by through-bond transfer units in analogy to NMR investigations of molecules free in solution.[40] The protein hydrogel discussed in **Chapter 7** of this thesis contains segments that reside in distinct motional regimes and can be studied in parallel using through-space and through-bond magnetization transfer. Lipids in membranes also experience significant degrees of motional freedom. Thus, high-resolution ^1H NMR spectra can be obtained for bilayers under moderate MAS allowing the characterization of membrane organization and interaction with associated molecules.[41] **Chapter 3** provides an example for the use of ^1H-^1H cross-relaxation rates obtained by Nuclear Overhauser Enhancement Spectroscopy (NOESY)[42] to study the location of an organic compound within a lipid bilayer.
Application of pulsed field gradients (PFG), furthermore, allows measurement of molecular self-diffusion.[43] The Lamor frequency of an individual spin in a field gradient encodes spatial coordinates and signal attenuation observed in gradient echo experiments can be related to the self-diffusion coefficient of the molecule of interest. The technique is well suited to probe lateral diffusion of lipids and membrane associated molecules.[44] Only very recently MAS ssNMR probes became available that combine field gradients and high power application necessary for high resolution spectroscopy in the solid phase. This development provides a powerful setup to study protein aggregation and folding as illustrated in **Chapter 7** for the gelation of a protein hydrogel.

In summary, ssNMR spectroscopy offers a variety of approaches to investigate inhomogeneous and insoluble systems such as proteoliposomes on structural and dynamical levels. Recent examples show that high resolution structures of proteins in the solid phase are accessible by a combination of spectroscopic, computational, and biochemical approaches. Complimentary ssNMR methods are available to probe protein dynamics and molecular interactions with the surrounding environment. In the future these experiments have to be standardized in order to increase experimental accuracy and allow for reliable quality validation. Combination of ssNMR spectroscopy with other biophysical techniques such as x-ray crystallography, small angle x-ray scattering, and solution-state NMR spectroscopy employing micelle or bicelle preparations might allow to balance methodological downsides, thus improving data quality and accelerating structural studies.

Scope of this thesis

Membrane associated proteins assemble transport machineries which facilitate for example translocation of molecules with high precision. These transport actions are often very selective and tightly regulated. Molecular understanding of such processes touches the core of the functionalities of biological membranes. This thesis discusses improvements in ssNMR methodology, sample preparation, and data analysis for the investigation of structure-function relations in selective membrane transport systems.

First, we investigated structure-function relations related to potassium channel gating. Gating of K^+ and other ion channels regulates the selective conduction of ions down their electrochemical gradient. In this process, the ion channel opens and closes for a defined duration of time in response to specific stimuli and external modulators of channel activity. The KcsA-Kv1.3 potassium channel (**Fig. 4**) served as model system for regulated ion transport across membranes essential for cellular excitability. **Chapter 2** introduces a technique to probe the topology of membrane proteins based on magnetization transfer from water to protein spins. This provides initial parameters describing the molecular rearrangement of the potassium channel during pH-induced activation. The different gating states of KcsA-Kv1.3 are then further characterized in **Chapter 3** and are compared to structural changes induced by small molecule ligand binding. **Chapter 4** deals with the effect of the permeant ion, K^+, on the functional elements of the channel and defines protonation states of the channel linked to activation and inactivation. Influences of the lipid environment on structure and function of the potassium channel are described in **Chapter 5** revealing the lipid bilayer as potential regulator of channel function. Finally, the use of ^{15}N longitudinal relaxation rates to study local dynamics in membrane associated proteins is demonstrated in **Chapter 6** for the KcsA-Kv1.3 K^+ channel.

Second, we studied basic components of the nuclear pore complex (NPC) which regulates all nuclear-cytoplasmic transport in eukaryotes (**Fig 5a**, **b**). FG-repeat domains are essential building blocks of the permeability barrier of NPCs. They allow free passage of small molecules, but suppress the flux of larger macromolecules and thereby prevent an uncontrolled intermixing of nuclear and cytoplasmic contents. However, the permeability barrier also permits a rapid passage of even large cargoes, provided these are bound to appropriate nuclear transport receptors (NTRs). These fundamental properties are well reproduced by hydrogels formed by isolated FG-domains providing an *in vitro* model for nuclear transport. **Chapter 7** provides a structural and dynamical study of such a protein hydrogel based on the yeast nuclear pore protein Nsp1p. The described ssNMR study establishes a structural link between two fundamental biological processes, i.e., nuclear transport and protein assembly.

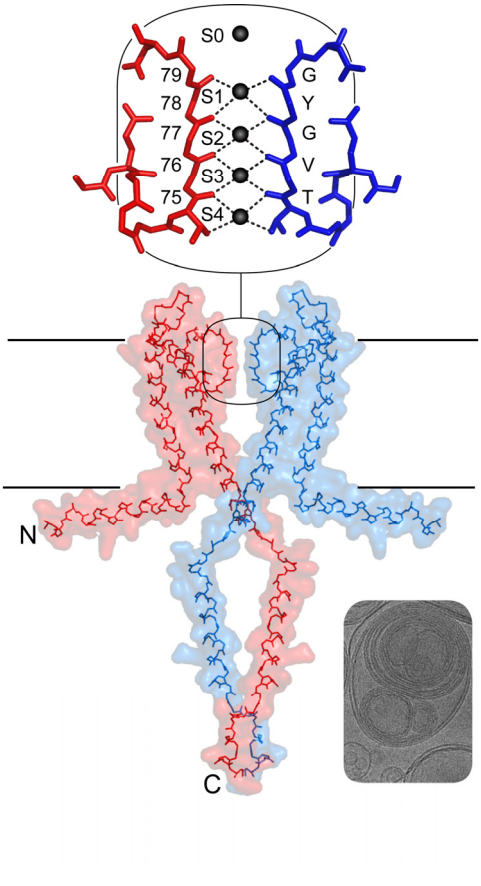

Figure 4. The bacterial K^+ channel KcsA[45] is a homotetramer and each subunit contains 160 amino acids. Here, the backbone conformation of a structural model based on x-ray[46] and magnetic resonance data[10,47] is shown. Only two opposite subunits are depicted in red and blue, respectively for visual clarity. The subunits comprise an amphipathic N-terminal helix, followed by a first transmembrane helix (TM1) that is connected to the short pore helix by an extracellular loop the forms the major part of the so called turret of the channel. The pore helix leads to the selectivity filter which connects via a short linker to the second transmembrane helix (TM2) that extends on the intracellular site to a C-terminal four helix bundle. The close-up provides details for the selectivity filter which is highly conserved among known cation channels. The carbonyl oxygens of the filter backbone create the potassium binding sites S0-S4 that favorably replace the hydrogen shell of potassium ions. The K^+ channel is studied reconstituted in liposomes similar to those seen in the electron microscopic picture shown in lower right corner.

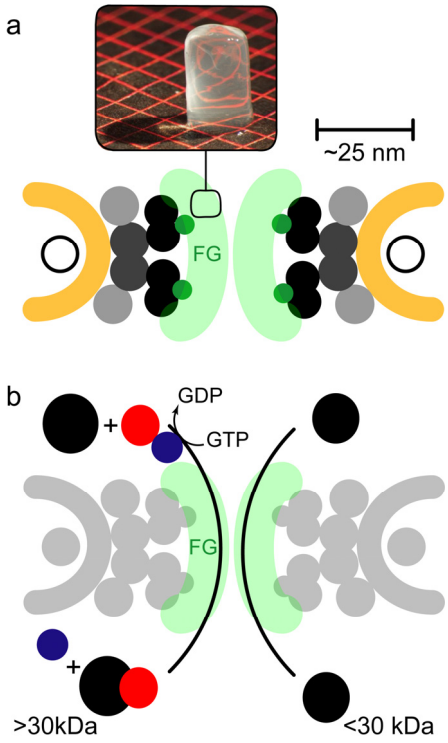

Figure 5. (***a***) Suggested architecture of the nuclear pore complex (NPC) adapted from ref. 48. Proteins of the outer and inner rings (light and dark grey) form the main scaffold of the NPC. They interact with the membrane ring proteins (white) anchoring the NPC in the nuclear envelope (yellow). Linker proteins (black) bridge this scaffold to the FG nuclearporins (green). The latter provide FG-rich domains (light green) that form the selectivity barrier of the NPC. The isolated FG domain of the nuclearporin Nsp1p forms a functional hydrogel (inlaid picture) selective for nuclear transport receptors providing an *in vitro* model system for nuclear transport.[49] (***b***) Illustration sketching nuclear transport. While molecules (black) smaller than 30 kDa can pass freely, larger molecules have to be shuttled via the RanGTP (blue) cycle bound to nuclear transport receptors (red) interacting with the FG domains. For a detailed review see ref. 50.

Chapter 2

Structural rearrangements of membrane proteins studied by water-edited solid-state NMR spectroscopy

Christian Ader[1,2]
Robert Schneider[2]
Karsten Seidel[2]
Manuel Etzkorn[2]
Stefan Becker[2]
Marc Baldus[1,2]

[1] Bijvoet Center for Biomolecular Research, Utrecht University, The Netherlands
[2] Max-Planck-Institute for Biophysical Chemistry, Germany

Journal of the American Chemical Society **131**, 170-176 (2009)

Abstract

We show that water-edited solid-state NMR spectroscopy allows for probing global protein conformation and residue-specific solvent accessibility in a lipid bilayer environment. The transfer dynamics can be well described by a general time constant, irrespective of protein topology and lipid environment. This approach was used to follow structural changes in response to protein function in the chimeric potassium channel KcsA-Kv1.3. Data obtained as a function of pH link earlier biochemical data to changes in protein structure in a functional bilayer setting.

Introduction

Membrane proteins control fundamental biological processes including protein synthesis and signal transduction. Their function is often intimately related to structural changes triggered by external stimuli and modulated by the surrounding membrane, making membrane proteins an important target for pharmacological research. Diffraction methods provide increasing insight into membrane protein structure but require the use of protein crystals (see, e.g., refs. 51, 52). While biophysical methods such as FRET and EPR offer structural insight at the nm scale[53,54], solid-state NMR (ssNMR) can be used to study very accurately local structural rearrangements in a membrane environment. Advanced techniques such as ^{19}F or nitroxide spin labeling can extend the NMR-detectable distance range beyond the 3-8 Å range limit if their effect on protein structure is minimized.[31,55,56] ssNMR pulse schemes adapting the Goldman-Shen[33] experiment were, in a complementary manner, used to globally probe membrane protein topology in peptides and proteins reconstituted in a native lipid environment.[9,34,57,58] In these experiments, the resulting one- or two-dimensional ssNMR data sets show signals arising from polarization transfer between water and proteins. In the case of a microcrystalline protein, chemical exchange was identified as a major pathway for magnetization transfer from water to the surface of a solid protein, and it was also confirmed that polarization transfer by NOE takes place. While the presence of intermolecular dipolar polarization transfer could not be directly demonstrated in this study, it can also not be strictly excluded (**Fig. 1**).[35,59] A principal question, therefore, has remained to which extent the data interpretation of these water-edited experiments, in particular the rate of magnetization transfer between water and the protein, depends on the details of the system of interest.

Using membrane proteins of different topology and in different membrane environments, we show in the following that one-dimensional water-edited ssNMR experiments can be well described by a general, effective diffusion coefficient for magnetization transfer from water to protein. Combining experimental results with three-dimensional lattice calculations supports the notion that different membrane protein systems are directly comparable in terms of the ratio between solvent-exposed surface and protein volume. Using the potassium channel KcsA-Kv1.3 as an example, we show that these dependencies provide a useful framework to study the protein-water interface on a residue-specific level. In addition, we demonstrate how these experiments can be used as a straightforward means to follow structural rearrangements related to channel gating in a functional membrane environment.

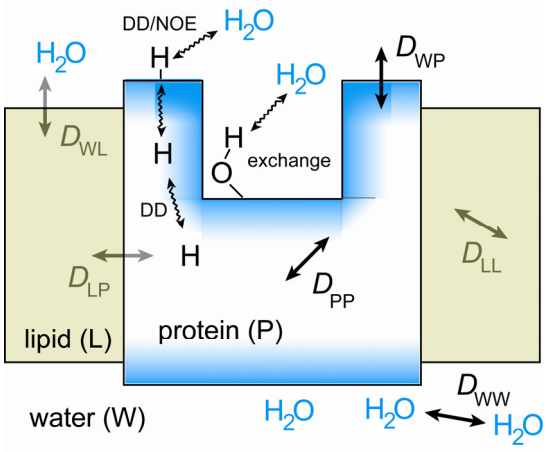

Figure 1. Schematic representation of diffusion pathways and possible mechanisms for magnetization transfer between and among water and protein protons (DD: direct dipolar interaction, NOE: nuclear Overhauser effect, exchange: chemical exchange processes involving fast exchanging protein protons). Relevant diffusion coefficients describing magnetization transfer between and among the different phases are indicated as D_{ij}, where i and j can be W (water), P (protein), and L (lipid).

Analysis of one-dimensional water-protein transfer curves

To study the details of the polarization transfer from water to a membrane-embedded protein, solid-state NMR experiments were recorded for proteoliposomes containing proteins of different size and different lipid compositions. In particular, sensory rhodopsin II from *Natronomonas pharaonis* (NpSRII), a monomeric phospholamban mutant (AFA-PLN) and the chimeric ion channel KcsA-Kv1.3 at pH 7.5 were investigated in a membrane setting. Bilayer preparations varied from synthetic (AFA-PLN) to purple membrane (NpSRII) lipids (**Table 1**).

	lipids	no. res.	mobile res.	no. protons	V_P	S_{WP}	H-H dist.	no. cubes	V_P^{mod}	S_{WP}^{mod}	t_m^s
NpSRII	purple membane	249	~44	~1810	28.6	38.5	2.51	2880	23.0	11.5	135
AFA-PLN	DMPC	54	~28	~260	3.4	6.6	2.34	336	2.7	1.9	90
KcsA-Kv1.3	asolectin	640	~0	~5000	43.1	235.6	2.05	7397	59.2	88.2	40

Table 1. Key data for NpSRII, AFA-PLN, and KcsA-Kv1.3. Lipid composition of the investigated proteoliposomes, total number of amino acid residues (no. res.), approximate number of mobile residues that do not contribute to the cross-polarization spectra (mobile res.)[9,10,40], approximate number of rigid protons (no. protons), protein volume in nm³ according to VADAR[60] (V_P), water accessible surface of the protein in nm² according to VADAR (S_{WP}), average proton-proton distance in Å defined as (V/No. protons)$^{1/3}$ (H-H dist.), number of 2 Å cubes of the low resolution model (no. cubes), volume of the low resolution model in nm³ (V_P^{mod}), water accessible surface of the low resolution model in nm² (S_{WP}^{mod}), initial rate saturation time in ms (t_m^s).

Figure 2a shows exemplarily ^{13}C detected 1D water-edited cross-polarization experiments (see Materials and Methods for details) performed for KcsA-Kv1.3 at pH 7.5 with different longitudinal proton-proton mixing times. No signal is

detected at zero mixing time confirming that residual protein magnetization can be fully suppressed by the combination of a selective initial pulse and a ^{1}H T_2 filter (τ = 1 ms). Notably, this aspect is crucial for a reliable interpretation of the build-up data. In addition, results of (selective) ^{1}H one pulse spectra confirm the high water content of KcsA-Kv1.3 proteoliposome preparations. The T_1-corrected build-up curves obtained by ^{13}C detected water-edited cross-polarization experiments, in which the (^{1}H, ^{1}H) mixing time t_m was varied, are given in **Figure 2b** for the systems considered.

In addition, the build-up curve for KcsA-Kv1.3 at pH 4.0 is plotted in **Figure 2b**. Following previous work on the parent KcsA channel[61], a change to acidic pH should lead to channel opening by rearrangement of the inner helix bundle.

In **Figure 2b**, solid black lines represent simulated build-up curves obtained from three-dimensional lattice calculations (see Materials and Methods). In these computations, three-dimensional spin networks representing structural models of the three investigated proteins were employed. These low-resolution representations were approximated for NpSRII starting from the available crystal structure[62], for AFA-PLN from the published solid-state NMR structure[40] and for KcsA-Kv1.3 from a structural model based on X-ray, EPR and ssNMR data[10,46,63] (**Fig. 2c**). To first approximation, lipid bilayers can be treated as inert diffusion barriers in the simulation due to comparatively small water to lipid and lipid to protein diffusion coefficients (D_{WL} and D_{LP}) and the small T_1 values measured for the lipids in our experiments (see Materials and Methods and **Table 2**). Thus, the lattice calculations depend only on two diffusion coefficients describing the efficiencies for magnetization transfer from water-protein and protein-protein spins. The source magnetization represented by water was considered to be large and the water bulk diffusion is several orders of magnitude faster than the observed transfer processes. Therefore, water magnetization was kept constant throughout the simulations. For all three systems, we found excellent agreement between experimental and simulated build-up curves investigated if a protein-protein diffusion coefficient of 0.3 nm²/ms and a water-protein diffusion coefficient of 0.008 nm²/ms were used. This result reflects the fact, that fast intramolecular spin diffusion is redistributing the polarization from the surface rapidly within the whole protein volume. Notably, the water-protein diffusion coefficient is about 6 times smaller than the value used in previous contributions.[34,57] Considering that these measurements were performed at significantly lower temperatures in the range of 240 K compared to 280 K used in our experiments, this difference can be attributed to the temperature dependence of the molecular dynamics of protein segments involved in the magnetization transfer from water to protein. Furthermore, the relative contribution of the polarization transfer mechanisms might change significantly with temperature. On the other hand, the protein-protein diffusion coefficient is only decreased by about 25% for our simulations, suggesting that the overall protein dynamics are comparable in all studies.

By linear extrapolation of the initial rate to 100% magnetization we obtain the value t_m^s (**Fig. 2b**) which describes the transfer characteristics away from saturation conditions[64]. The correlation coefficients for linear fits to the initial rate of magnetization transfer are 0.995, 0.996, and 0.998 for KcsA-Kv1.3, SRII and AFA-PLN, respectively. At time t_m^s, equation (4) equals 1 and we obtain a linear

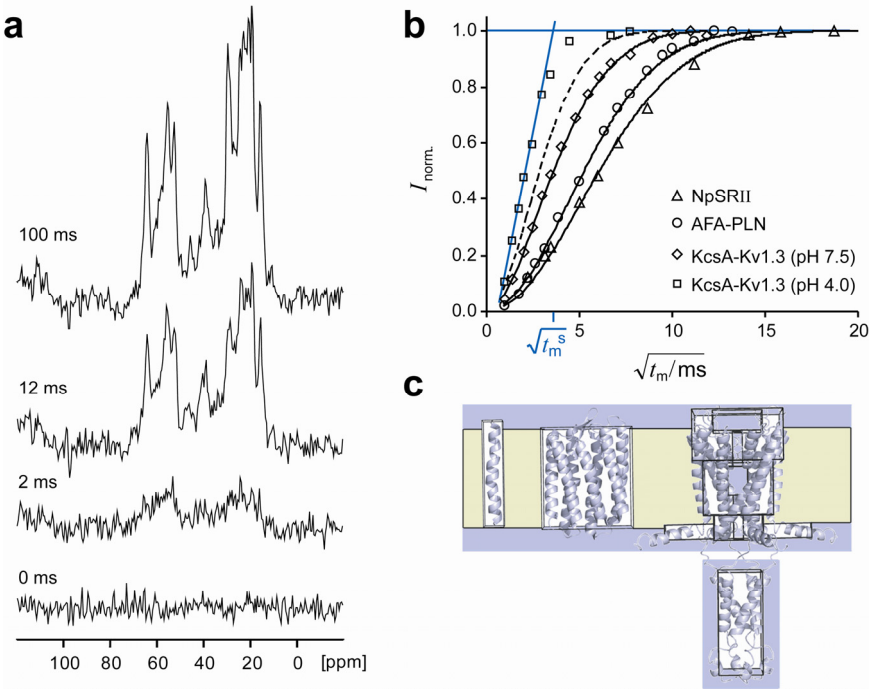

Figure 2. (***a***) ^{13}C detected 1D water-edited cross-polarization experiments performed for KcsA-Kv1.3 at pH 7.5 with different longitudinal ^{1}H-^{1}H mixing times (t_m = 0, 2, 12, and 100 ms). (***b***) Normalized intensities obtained for 1D water-edited cross-polarization experiments plotted against the square root of mixing time t_m. The error of the data points given by the signal/noise of the integrated spectra is in the order of 2 – 4% for all build-up curves. Black lines represent simulated build-up curves based on 3D lattice calculations. The value $\sqrt{t_m^s}$ is obtained by a linear fit to the initial rate of the build-ups as illustrated by blue lines (see text for details). (***c***) Low-resolution models of AFA-PLN (left), NpSRII (middle), and KcsA-Kv1.3 (right) (black lines) are aligned to the underlying structures (grey cartoons). Lipid membrane (yellow) and water (blue) are illustrated as defined for the 3D lattice calculations.

dependence between the square root of t_m^s and the volume to surface ratio given in equation (5). This dependence is in good agreement with the plot of volume to surface ratios determined for the low resolution models compared to experimental values for the square root of t_m^s shown in **Figure 3a**. Hence, an effective diffusion coefficient for the magnetization transfer from water to membrane proteins of about 0.2 nm²/ms can be derived that establishes a general parameter to monitor V_p/S_{WP} by ssNMR.

While the error associated with t_m^s mainly depends on the signal-to-noise ratio of the evaluated spectra, judging the error of the volume to surface ratio is difficult. The volume per amino acid is 0.10 ± 0.01 nm³ for the three low-resolution models investigated. This suggests that the protein volume can be approximated quite accurately on the basis of protein size. However, the definition of the water-accessible surface depends on the lipid bilayer thickness and the surface itself is inaccurate due to the three-dimensional shape of the spin network.

In order to verify the accuracy of the low-resolution models used for the lattice calculations, we employed the VADAR Web Server[60] to obtain volume and water accessible surfaces for the underlying protein structures and structural models. The

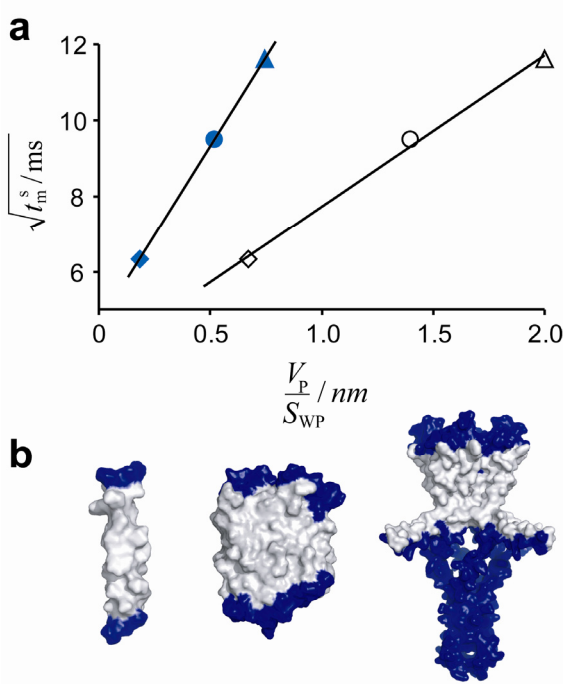

Figure 3. (***a***) Plot of experimentally determined values for $\sqrt{t_m^s}$ versus volume to water-accessible surface ratios calculated based on the low-resolution models of KcsA-Kv1.3 (◊), AFA-PLN (○) and NpSRII (Δ) and based on the underlying structures of KcsA-Kv1.3 (♦), AFA-PLN (●) and NpSRII (▲). Straight lines give linear fits to the data (R^2(low resolution)= 0.997 and R^2(structures) = 0.999). (***b***) Surface representations of AFA-PLN (left), NpSRII (middle), and KcsA-Kv1.3 (right). Residues defined to be water accessible are labeled blue.

total volume of the protein is calculated as the sum of the space enclosed by the van der Waals surfaces of all residues. Residues contributing to the water accessible surface were selected based on existing data[9,10,40] (**Fig. 3b**, **5**) and the surface area was computed by summing up accessible surface areas identified by VADAR for residues that contribute to the defined water-protein interface. **Table 1** summarizes dimensional parameters obtained for the low-resolution models and the underlying structures. The volumes of the low-resolution models deviate by 20-30% from the van der Waals volume analysis confirming that the low-resolution models provide a reasonable approximation for the proteins considered.

Changes in reference to the protein surface should only mildly affect the residual protein-protein diffusion coefficient. According to **Table 1**, the calculated average proton-proton distances give values close to 2 Å, which is line with our numerical analysis. Starting from the protein-protein diffusion coefficient D_{PP} of 0.3 nm²/ms, we can estimate the transfer rate of magnetization, Ω, between two protons a = 2 Å apart to be 7.5 kHz according to $\Omega = D_{PP}/a^2$. This value is in good agreement to earlier studies studying carbon-detected proton-proton mixing under MAS conditions.[65] On the other hand, the surface areas of our low-resolution models and structures differ on average by a factor of 3.2 ± 0.4 reflecting the different levels of surface complexity. Therefore, the protein surfaces are underestimated in the simulations or, correspondingly, the water to protein diffusion coefficient is overestimated in the lattice calculations. Plotting the square root of t_m^s against the volume to surface ratio obtained based on the van der Waals radii yields a linear dependency suggesting an effective diffusion coefficient for water-protein magnetization transfer of 0.04 nm²/ms (**Fig. 3a**). This value is five times smaller than the effective diffusion coefficient obtained based on the low-resolution models in line with the discrepancy in water accessible surface areas. By simulating the magnetization transfer in spin networks of various volume-to-surface ratios, we can show that the larger water accessible surface of the van der Waals representations

correlates linearly with a decrease in the water-protein diffusion coefficient (**Fig. 4**). Thus, the actual water-protein polarization transfer rate at the given temperature of 280 K should be on average 60 Hz, providing an overall estimate of the transfer rate for magnetization transfer from water to protein. Such a value is both compatible with ^{1}H-^{1}H dipolar couplings and chemical exchange processes. Local transfer rates involving individual spin pairs may, however, differ significantly. In this context it might be important to point out that the fraction of amino acid residues having exchangeable protons in addition to the backbone amides ranges from 25 to 55 % in the water-accessible surfaces as defined in **Figure 3b**.

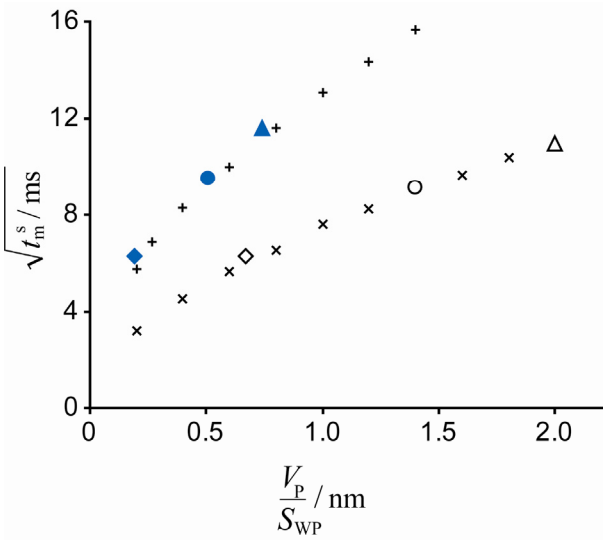

Figure 4. Simulated $\sqrt{t_m^s}$ values obtained for various V_P to S_{WP} ratios using values for D_{WP} of 0.008 nm²/ms (x) and 0.0025 nm²/ms (+). D_{PP} was constantly set to 0.3 nm²/ms. Experimental values for $\sqrt{t_m^s}$ are plotted against V_P to S_{WP} ratios calculated for the structural models of KcsA-Kv1.3 (♦), AFA-PLN (●) and NpSRII (▲). Simulated values for $\sqrt{t_m^s}$ are plotted against V_P to S_{WP} ratios calculated for the low-resolution models of KcsA-Kv1.3 (◊), AFA-PLN (○) and NpSRII (Δ).

Two-dimensional, residue-specific analysis

In line with our recent work on NpSRII,[9] our analysis of 1D transfer dynamics confirms that 2D water-edited (^{13}C, ^{13}C) correlation experiments measured in the initial regime (2.5 ms (^{1}H, ^{1}H) mixing time) can provide residue-specific information about the H_2O-accessible protein surface. In the case of KcsA-Kv1.3 at pH 7.5 (**Fig. 5**), we find that the water-accessible protein surface comprises residues in the extracellular turret and the C-terminal helices of the potassium channel. In addition, we can unambiguously assign resonances that originate from the lower part of the selectivity filter including Thr74 and Thr75. The Cα-Cβ cross-peak intensities of these residues are comparable to values seen for Thr85 which is located in the turret of KcsA-Kv1.3. Residue-specific 3D lattice calculations (**Fig. 6**) show that this finding is compatible with a water accessible selectivity filter and rule out a selectivity filter conformation that is remote from fast exchanging water. It should be mentioned that such an analysis is not possible for larger mixing times t_m as spin-diffusion rapidly distributes magnetization throughout the protein. Under such conditions, the use of deuterated protein samples and transversal mixing periods may be helpful.[66] Comparing experiment and simulation, we conclude that selectivity filter and inner cavity of the channel are accessible to water on the timescale relevant for our experiment. This is especially notable as solvent accessibility of the selectivity filter and the inner cavity has mostly been discussed on the basis of molecular dynamics simulations.[67,68]

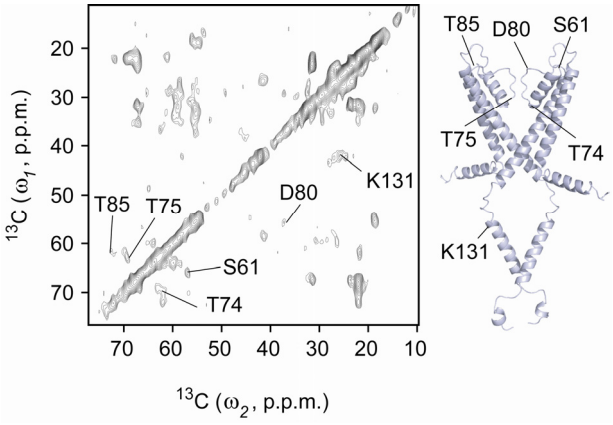

Figure 5. Water-edited initial regime (^{13}C, ^{13}C) correlation spectrum for KcsA-Kv1.3 at pH 7.5. Selected cross peaks representing turret, C-terminus and selectivity filter are labeled and indicated in the structural model (only two subunits are shown). Note that resonances were only considered if unambiguous in terms of the chemical-shift values and if present on both sides of the diagonal.

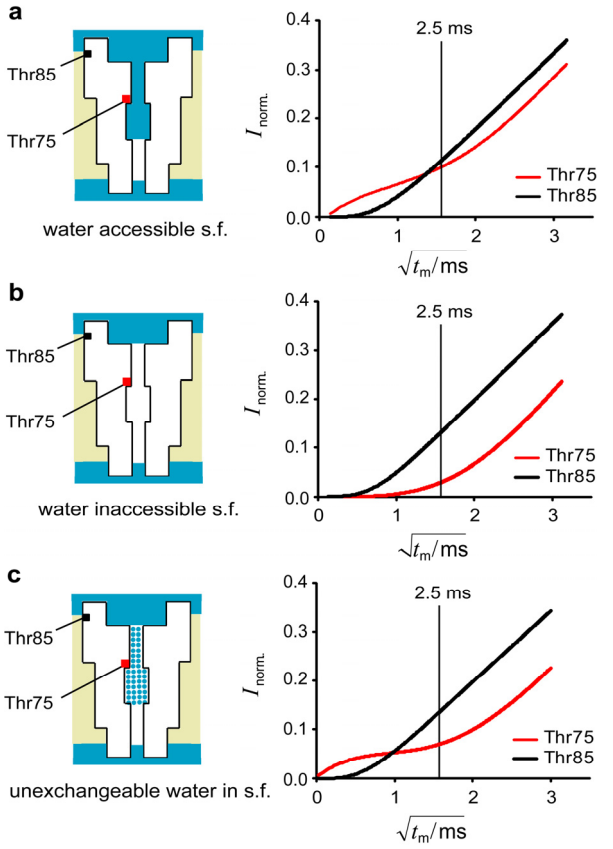

Figure 6. The magnetization transfer to threonine residues 75 and 85 was monitored in lattice calculations in which the selectivity filter (s.f.) and inner cavity were defined as water accessible (***a***) and water inaccessible (***b***). Additionally, lattice calculations were performed for the case of mobile water confined to cavity and filter not exchanging with bulk water (***c***). The amino acid residues were represented by 2 Å cubes located at appropriate positions in the low resolution model of KcsA-Kv1.3. The diffusion coefficients D_{WP} = 0.3 nm^2/ms and D_{PP} = 0.008 nm^2/ms were the same as used for the global simulations given in the main text. The mixing time t_m = 2.5 ms used for the two-dimensional water-edited (^{13}C, ^{13}C) spectrum given in Figure 5 is indicated by a line.

Channel opening as seen by water-edited ssNMR

Sizeable structural changes, for example as expected in response to KcsA-Kv1.3 channel opening by changes in pH, should influence H_2O-edited ssNMR experiments. Indeed, using equation (5), the experimentally determined values for $\sqrt{t_m}^s$, and constant protein volumes we can readily compute an increase in water-accessible surface area of KcsA-Kv1.3 by about 65% if pH is brought from pH 7.5 to pH 4.0. The interpretation of relative changes in water-accessible surface has the advantage that the effective diffusion coefficient D_{eff} can be eliminated, and thus, the results obtained do not depend on the errors introduced by the definition of the low-resolution models and the water-accessible surface areas. **Figure 7a** shows the pH-dependent change of the square root of the initial rate 100% time t_m^s for KcsA-

Kv1.3. The data can be fitted to the Hill equation if we consider the obtained saturation times to be an average for two states of the channel, i.e., one closed and one opened state. We obtain a Hill coefficient of 1.0 ± 0.2 and a pK_a value of 6.0 ± 0.3. These values compare favourably to results obtained on the parent KcsA K^+ channel by measuring the pH dependence of $^{86}Rb^+$ influx under similar conditions.[63] On the basis of crystal structures of open potassium channels such as MthK[69] and Kv1.2[70] as well as a recent ssNMR study of KcsA-Kv1.3,[71] we approximated a low-resolution model for the open pore domain – omitting N- and C-terminus – for KcsA-Kv1.3 at pH 4.0 (**Fig. 7b**). Compared to the low-resolution model for the closed potassium channel at pH 7.5 the water accessible protein surface is increased by about 50%. The simulated build-up curve for this model is given as dashed line in **Figure 2b**. It is obvious that this model does not fully account for the increase in water accessible protein surface observed experimentally. However, the degree of change agrees well with the notion that channel opening is associated with a structural rearrangement leading to a major increase in pore diameter and possibly also affects the water accessibility of C- and N-terminus of the potassium channel.

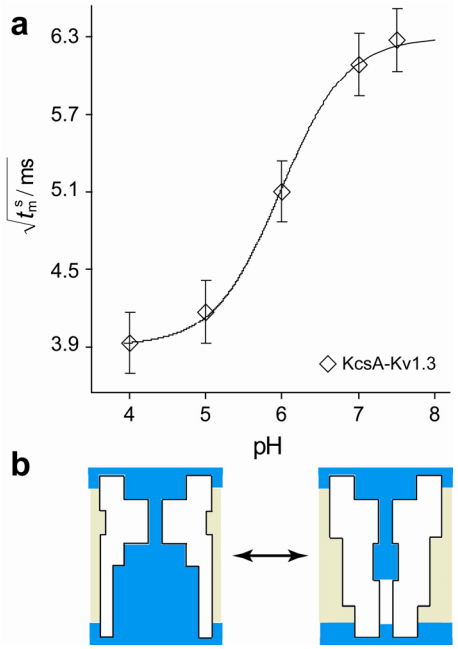

Figure 7. (***a***) Plot of the square root of experimentally determined initial rate 100% values t_m^s for KcsA-Kv1.3 against pH. Error bars represent signal/noise of the evaluated 1D spectra. (***b***) Cross-section of the low-resolution models for the opened and closed pore domain of KcsA-Kv1.3. Lipid membrane (yellow) and water (blue) are illustrated as defined for the 3D lattice calculations.

Discussion

Water-edited solid-state NMR experiments allow for probing the water-protein surface in reference to the protein volume of large membrane proteins in close analogy to domain-size measurements performed previously for heterogeneous polymers.[72,73] Here, we have reported effective diffusion coefficients that allow for computation of H_2O surface-to-volume ratios based on the time constant t_m^s describing magnetization transfer from water to protein. Such an analysis is possible for both low-resolution models suitable for lattice calculations and protein structures if high-resolution information is available. Low-resolution models may

permit to distinguish different membrane protein topologies and help to estimate the magnitude of structural rearrangements as demonstrated for KcsA-Kv1.3. In general, the error associated with the low-resolution model should decrease with protein size making the analysis more favorable for large proteins or protein complexes. If high-resolution structural information is available, water-edited ssNMR spectroscopy might serve as a qualitative means to elucidate 3D molecular structure in membranes under variable experimental conditions such a lipid type or composition.

Isotope-labeling of the protein in combination with 2D spectroscopy offers a sensitive means to examine the H_2O-accessible surface of the protein on the atomic level. Notably, such information can also be obtained in other macromolecular systems[74] and the data can be analyzed in a manner complementary to EPR studies using solvent accessibility data.[75,76] In addition, structural changes in response to function can be followed on the global and local scale. In the case of pH-induced opening of the KcsA-Kv1.3 channel, the calculated increase in water-accessible surface area of the K^+ channel is in line with crystal structures of other opened potassium channels. Furthermore, the pH dependence of channel opening could be followed on a direct structural basis in a titration experiment. The resulting Hill coefficient is in good agreement with biochemical data for the parent potassium channel KcsA underlining the potential of ssNMR to directly relate protein structure to function in a membrane setting.

Materials and Methods

Sample preparation. Sensory rhodopsin II from *Natronomonas pharaonis* (NpSRII), a monomeric phospholamban mutant (AFA-PLN), and the chimeric potassium channel KcsA-Kv1.3 were prepared as described previously.[9,13,40] pH titration for KcsA-Kv1.3 was performed by washing the samples three times with 100 mM citric acid / citrate buffer or 50 mM phosphate buffer adjusted to the desired pH.

Solid-state NMR experiments and analysis. All 1D and build-up experiments (**Fig. 8a**, **b**) were recorded on a 400 MHz instrument (Bruker Biospin). A 3 ms Gaussian pulse and a T_2 filter containing two delays (τ) of 1 ms were used for selective water excitation. The cross-polarization contact time was set to 700 µs. The field strength for SPINAL64[77] proton decoupling was typically between 70 and 83 kHz. All ssNMR experiments were performed at 280 K using a 4 mm triple-resonance MAS (Magic Angle Spinning) probe and an MAS rate of 6.5 kHz. 2D water-edited (^{13}C, ^{13}C) correlation experiments (**Fig. 8c**) were performed at 600 MHz proton frequency using an MAS rate of 9.375 kHz and a temperature of 280 K. Spin-diffusion times t_m and τ_m were set to 2.5 ms and 20 ms, respectively. Other experimental parameters were similar as described above. To analyse the ^{13}C detected water-edited build-up experiments, peak integrals for the spectral region from 80 p.p.m. to 0 p.p.m. were obtained and corrected for water T_1 relaxation by multiplication with $\exp(t_m/T_1)$. ^1H spin-lattice relaxation times of the water and the tail CH_2 lipid signals were measured using standard NMR inversion recovery sequences.

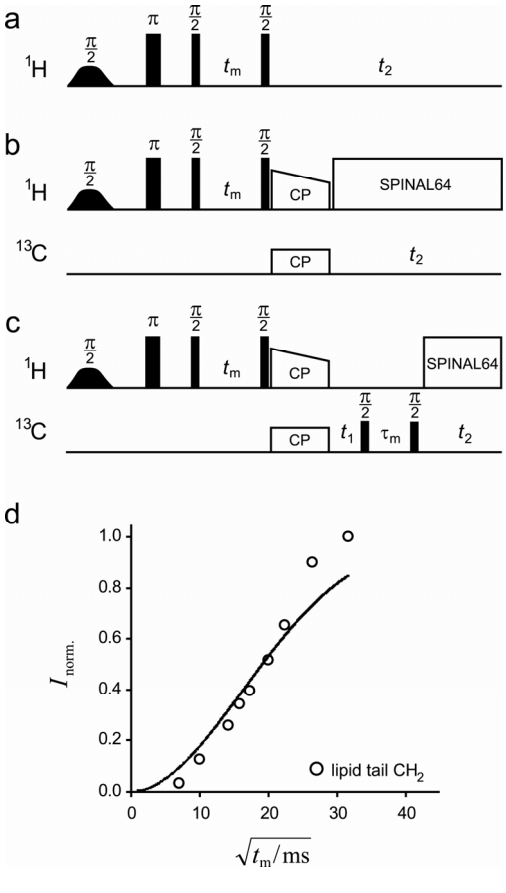

Figure 8. (***a***) Pulse scheme for a ^{1}H-detected 1D water-edited experiment. (***b***) Pulse scheme for a ^{13}C-detected 1D water-edited cross-polarization experiment. After an initial Gaussian 90° pulse on resonance with the ^{1}H water signal, a ^{1}H T_2 filter (τ) leads to the selection of mobile water ^{1}H magnetization. A subsequent longitudinal spin diffusion unit (t_m) establishes polarization transfer to protein protons. Transferred magnetization is read out after a cross-polarization step on ^{13}C nuclei. (***c***) Pulse scheme for 2D water-edited dipolar (^{13}C, ^{13}C) correlation spectroscopy including an additional (^{13}C, ^{13}C) spin-diffusion unit of duration τ_m. (***d***) Normalized intensities for the ^{1}H lipid tail CH_2 resonance at 0.9 p.p.m. of asolectin liposomes, obtained for ^{1}H detected 1D water-edited experiments, plotted against the square root of mixing time. The solid line represents the simulated build-up curve based on lattice calculations using a water-lipid diffusion coefficient for magnetization transfer of 0.001 nm²/ms and a lipid to lipid diffusion coefficient of 0.016 nm²/ms.

Theoretical background. Starting from the diffusion equation for z magnetization $M(\vec{r},t_m)$

$$\frac{\partial M(\vec{r},t_m)}{\partial t_m} = \vec{\nabla}\cdot\left\{D(\vec{r})\vec{\nabla}M(\vec{r},t_m)\right\}, \qquad (1)$$

magnetization transfer from water to protein can be described assuming a semi-infinite two-phase system with a uniform ^{1}H spin density.[64] At time zero, the magnetization is homogeneously distributed in phase A (water in our case) and zero in phase B (protein in our case). Diffusion of magnetization from phase A to B for a system with homogeneous diffusibility can then be described as follows

$$\frac{I_B(t_m)}{I_B(t_m\to\infty)} = \sqrt{\frac{Dt_m}{\pi}}\frac{1}{f_A f_B}\frac{S_{AB}^{tot}}{V^{tot}} - O(\sqrt{t_m}^2) \quad (2)$$

In (2), $I_B(t_m\to\infty)$ represents B (protein) magnetization under equilibrium conditions. Furthermore, D is the diffusion coefficient and f_A , f_B stand for the volume fractions of phases A and B, respectively. In addition, S_{AB}^{tot} is the total

interface area between A and B, and V^{tot} represents the total sample volume. $O(\sqrt{t_m}^2)$ is a term quadratic in $\sqrt{t}_m$ and will be ignored in the following. Assuming that phase A (water) takes a major fraction of the sample volume and the total volume of phase B (protein) is small in contrast, equation (2) reduces to

$$\frac{I_B(t_m)}{I_B(t_m \to \infty)} \approx \sqrt{\frac{Dt_m}{\pi}} \frac{S_{AB}^{tot}}{V_B} \qquad (3)$$

because $f_A \approx 1$.

Notably, proteoliposome samples discussed above do not fulfil the assumption of homogeneous diffusibility as postulated for the derivation of equation (3). Thus, the diffusion coefficient D in equation (3) represents an effective diffusion parameter D_{eff} comprising all diffusion coefficients relevant for the observed magnetization transfer in the system.

Replacing $D \rightarrow D_{\text{eff}}$ and the indices A→W, B→ P, and $I_B(t_m) \rightarrow M_P(t_m)$ in (3), we obtain

$$\frac{M_P(t_m)}{M_P(t_m \to \infty)} \approx \sqrt{\frac{D_{eff}}{\pi}} \frac{S_{WP}}{V_P} \sqrt{t_m} \qquad (4)$$

and for the limit $M_P(t_m^s) = M_P(t_m \to \infty)$

$$\sqrt{t_m^s} = \sqrt{\frac{\pi}{D_{eff}}} \frac{V_P}{S_{WP}} \qquad (5)$$

Hence, the time constant of the magnetization transfer is proportional to the molecular dimensions of the protein in close analogy to domain-size measurements performed previously for heterogeneous polymers.[72,73]

Three-dimensional lattice calculations. We utilized the concept of 'diffusion on a lattice' as described by Schmidt-Rohr and Spiess (Ref. 64, chapter 13.3.3) to numerically simulate the build up for protein magnetization according to equation (1). Correspondingly, a 3D lattice was constructed to reflect a low-resolution model of the protein of interest (see also Results, **Fig. 2c**). The corresponding spin network consists of cubes with an edge length, d, of 2 Å. Only protein segments that contribute to the cross-polarization signal were considered for the low-resolution models. Each cube was defined to be part of the protein, the lipid membrane, or the surrounding water. Magnetization transfer within the three-dimensional spin network was calculated in MATLAB using time steps, Δt_{m}, of 20μs according to

$$M_{x,y,z}(t_m + \Delta t_m) = M_{x,y,z}(t_m) + \sum_i \frac{D_{ij}\Delta t_m}{d^2}(M_i(t_m) - M_{x,y,z}(t_m)). \quad (6)$$

Here, $M_i(t_m)$ monitors the magnetization of the six neighboring cubes (x+1,y,z; x-1,y,z; x,y+1,z; x,y-1,z; x,y,z+1; x,y,z-1), and the D_{ij} stand for the corresponding diffusion coefficients. Magnetization of water was kept constant at 1 assuming a large water pool and water bulk diffusion in the range of 10^6 nm²/ms that is orders of magnitude faster than the observed exchange processes. In addition to magnetization transfer from water spins directly to protein spins and among protein nuclei, indirect pathways of magnetization transfer via lipid molecules may influence the measured build-up rates. To characterize the influence of the surrounding lipid bilayer, we performed water-edited experiments observing the magnetization transfer from water to the lipid tail protons of asolectin liposomes (**Fig. 8d**). The experimental build-up curve for CH_2 lipid side chain magnetization was compared to lattice calculations considering two diffusion coefficients for water-lipid and lipid-lipid magnetization transfer. From the data, we approximate a water-lipid diffusion coefficient of about 0.001 nm²/ms which is almost 1 order of magnitude smaller than the water-protein diffusion coefficient obtained under identical experimental conditions (see Results). In addition, a lipid-lipid diffusion coefficient of 0.016 nm²/ms was found. Our results are in line with earlier work reporting a lipid-lipid diffusion coefficient of 0.012 nm²/ms, a lipid-protein diffusion coefficient of 0.0025 nm²/ms, and a protein-protein diffusion coefficient of 0.3 nm²/ms[58]. Furthermore, we find for lipid chain protons T_1 values of typically 200-500 ms while water T_1 values are between 500 and 1200 ms for all samples used in this study (see also **Table 2**). Therefore, magnetization transferred via lipid protons is further reduced by accelerated relaxation. In summary, we conclude that indirect pathways of magnetization transfer from water to protein via lipid spins can be neglected to first approximation. Consequently, the protein magnetization was initially set to zero, while the lipid magnetization remained zero during the course of the lattice calculations. For all simulations, the relative protein magnetization was read out every 1 ms.

Sample	D_{PP}	D_{WP}	D_{LL}	D_{WL}	$T_1(H_2O)$	T_1(lipid)
Asolectin liposomes	-	-	0.016	0.001	500	450
NpSRII	0.3	0.008	-[a)]	-[a)]	1200	590
AFA-PLN	0.3	0.008	-[a)]	-[a)]	690	350
KcsA-Kv1.3 (pH 7.5)	0.3	0.008	-[a)]	-[a)]	1150	250

Table 1. Diffusion coefficients as obtained by lattice calculations for magnetization transfer from protein to protein (D_{PP}), water to protein (D_{WP}), lipid to lipid (D_{LL}), and water to lipid (D_{WL}) (in nm²/ms) that agree best with the experimental data and experimentally determined T_1 values for water and the CH_2 lipid tail resonance (in ms). a) Secondary pathways for magnetization transfer from water to protein via the lipid protons were ignored in the performed 3D lattice calculations.

Chapter 3

A structural link between inactivation and block of a K^+ channel

Christian Ader[1]
Robert Schneider[1]
Sönke Hornig[2]
Phanindra Velisetty[2]
Erica M. Wilson[3]
Adam Lange[1]
Karin Giller[1]
Iris Ohmert[2]
Marie-France Martin-Eauclaire[4]
Dirk Trauner[3]
Stefan Becker[1]
Olaf Pongs[2]
Marc Baldus[1]

[1] Max-Planck-Institute for Biophysical Chemistry, Germany
[2] University Hospital Hamburg-Eppendorf, Germany
[3] University of California, Berkeley, USA
[4] Centre National de la Researche Scientifique, France

Nature Structural & Molecular Biology **15**, 605-612 (2008)

Abstract

Gating the ion-permeation pathway in K^+ channels requires conformational changes in activation and inactivation gates. Here we have investigated the structural alterations associated with pH-dependent inactivation gating of the KcsA-Kv1.3 K^+ channel using solid-state NMR spectroscopy in direct reference to electrophysiological and pharmacological experiments. Transition of the KcsA-Kv1.3 K^+ channel from a closed state at pH 7.5 to an inactivated state at pH 4.0 revealed distinct structural changes within the pore, correlated with activation-gate opening and inactivation-gate closing. In the inactivated K^+ channel, the selectivity filter adopts a nonconductive structure that was also induced by binding of a pore-blocking tetraphenylporphyrin derivative. The results establish a structural link between inactivation and block of a K^+ channel in a membrane setting.

Introduction

Gating of K^+ and other ion channels is an important mechanism to regulate the selective conduction of ions down their electrochemical gradient across the plasma membrane.[78] In this process, the ion channel opens and closes for a defined duration of time in response to a specific external stimulus such as a change in the membrane electric field and/or in ligand concentration. Channel gating involves conformational changes at an activation gate in the permeation pathway.[69,79] Frequently, prolonged stimulation shuts the permeation pathway and renders the ion channel refractory to further activation. This process is called inactivation. Different inactivation mechanisms have been discovered involving distinct ion channel domains.[79] For example, particular C-terminal domains are associated with C-type inactivation of voltage-gated delayed-rectifier type K^+ (Kv) channels.[79] C-type inactivation seems to be an effective mechanism for controlling Kv channel activity to regulate action-potential firing frequencies in excitable cells.[80] It is suggested that C-type inactivation of Shaker Kv channels is correlated with a nonconducting structure of the pore reflecting a low occupancy of K^+ binding sites in the selectivity filter.[79] This permits C-inactivated channels to conduct Na^+ and Li^+ (Refs. 81-83). Inactivation of the KcsA K^+ channel shares many properties with C-type inactivation. Factors that influence KcsA K^+ channel inactivation have been investigated in great detail, such as intracellular pH and transmembrane voltage. The results supplemented by molecular dynamics simulations have provided detailed models on the regulation of KcsA K^+ channel inactivation.[84-87] Knowledge of the protein structural rearrangements that occur with activation and inactivation gating of the K^+ channel is of central importance for understanding the molecular mechanisms underlying K^+ channel gating. The available data suggest that two separate gates control activation and, respectively, C-type inactivation gating of the KcsA K^+ channel.[88] The activation gate seems to be associated with structures in the intracellular half of the channel, such as the gating hinge and inner helix bundle.[46,69,70,89] The inactivation gate has been localized to the selectivity filter in the extracellular half of the channel. Recent mutational analysis of inactivation gating in the KcsA K^+ channel has shown that stability of the closed inactivation gate is determined by a hydrogen bond network on the back side of the selectivity filter.[86,87] The inactivation mechanism of the KcsA K^+ channel, however, has been

inferred from non-inactivating mutants, because the structure of an inactivated KcsA K^+ channel is still elusive; this highlights the need for direct structural approaches to this important K^+ channel gating process. Solid-state NMR (ssNMR) spectroscopy provides a structural tool for studying functional K^+ channels in a membrane setting in combination with electrophysiological recordings. Previously, we have shown that ssNMR experiments combined with biochemical experiments were suitable to obtain a detailed picture of the structural changes that were associated with binding the scorpion toxin kaliotoxin (KTX) to the external mouth of the chimeric KcsA-Kv1.3 K^+ channel.[13] This channel is assembled from bacterial KcsA subunits in which turret residues 52 to 64 were replaced by the corresponding mammalian Kv1.3 turret residues 368 to 380 to generate a high-affinity scorpion toxin binding site.[14] Here we investigated conformational changes associated with pH-dependent inactivation gating of the KcsA-Kv1.3 K^+ channel. Transition of the KcsA-Kv1.3 K^+ channel from a closed state at pH 7.5 to an inactivated state at pH 4.0 induced distinct structural changes within the pore of the K^+ channel, correlated with an opened activation and a closed inactivation gate. In the inactivated K^+ channel, the selectivity filter adopts a nonconductive structure that was also induced by binding a tetraphenylporphyrin derivative ('porphyrin'), which competes with scorpion toxins for binding to the Kv1.3 channel pore.[90] The data show that ligands that occlude the external pore of K^+ channels, particularly KTX and porphyrin, can induce different conformational changes.

Results

Conformational changes associated with KcsA-Kv1.3 channel gating

Solution-state NMR studies using detergent micelles were previously conducted to probe conformational changes related to toxin binding and gating on the prototypical KcsA K^+ channel.[91-95] Alternatively, we used ssNMR spectroscopy to investigate conformational changes associated with gating and ligand binding of the KcsA-Kv1.3 K^+ channel embedded in liposomes. Using a series of multidimensional ssNMR experiments on different KcsA-Kv1.3 variants led us to assignments for 59% of the residues of the full-length protein, corresponding to 73 residues in the transmembrane and extracellular regions and 21 residues in the N- and C-terminal intracellular regions[10] (**Fig. 1**). Secondary-structure analysis based on secondary chemical shifts revealed α-helical structure between residues 22–53, 62–73 and 86–116 in good agreement with the crystal structure.[46] In addition, an amphipathic N-terminal helix (between residues 4 and 19) and a cytoplasmic C terminal helix (starting from residue 129) were evident, consistent with a previous electron paramagnetic resonance (EPR) study using spin-labeled KcsA channels[63] and solution NMR data.[91] The transmembrane helix 1 (TM1, residues 22–53) was found in our ssNMR study to be about three turns longer than that observed in solution NMR data with KcsA micelle preparations (residues 30–51 (ref. 91) or 31–52 (ref. 93)). This is likely to be functionally important, because His25 within the TM1 helix has been shown to be a key residue for opening the KcsA K^+ channel.[94] These and other secondary-structure differences seen at pH 7.5 between our ssNMR and solution NMR data are in line with the notion that lipid membranes have an important role for structure and function of K^+ channels.[89,96,97]

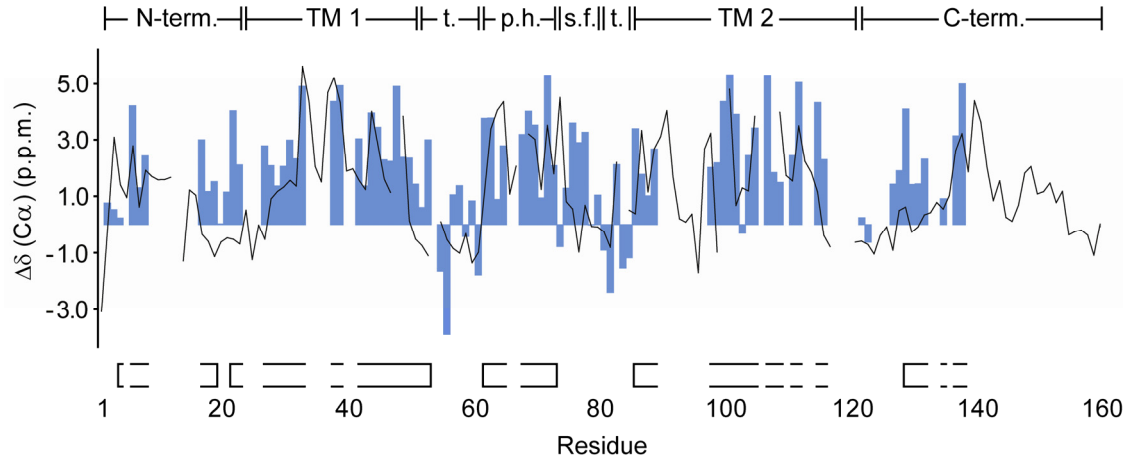

Figure 1. Comparison of solid-phase and solution-state NMR Cα secondary chemical shifts on KcsA variants. Blue bars: KcsA-Kv1.3 in liposomes as seen by solid-state NMR; black line: full-length KcsA studied by solution-state NMR in foscholine micelles.[91] Positive values indicate helical structure. Secondary structure elements of the crystal structure (PDB ID 1K4C)[46] are given as horizontal lines at the top (TM: transmembrane helix; t.: turret loop; p.h.: pore helix; s.f.: selectivity filter), as well as N- and C-terminal regions not covered by the crystal structure. Horizontal bars at the bottom show helical segments as seen by ssNMR.[10]

Inside-out patch-clamp experiments on KcsA-Kv1.3 in proteoliposomes showed that the KcsA-Kv1.3 channel is closed at pH 7.5 and activated by an increase in H^+ concentration on the intracellular side, as occurs in the parent KcsA channel[86,98,99] (**Fig. 2a**). Also, the KcsAKv1.3 K^+ channel rapidly entered into an inactivated state during a prolonged pH stimulus. Current amplitudes of activated KcsA-Kv1.3 K^+ channels decayed to about 8% of the initial amplitude within 1 s (**Fig. 2a**). Note that mutation R64A markedly slowed inactivation of the KcsA K^+ channel[85], whereas mutation R64D in KcsA-Kv1.3 did not. The electrophysiological data provided us with the important information that KcsA-Kv1.3 channels in proteoliposomes had entered an inactivated state when the intracellular pH was 4.0. We further tested this observation by measuring the KcsA-Kv1.3 steady-state activity at pH 4.0 after reconstitution into lipid bilayers. With pH 4.0 on the trans side of the lipid bilayer, we observed KcsA-Kv1.3 K^+ channel activity (**Fig. 2b**) similar to that reported for the KcsA K^+ channel.[98,99] The KcsA-Kv1.3 K^+ channel opened only briefly with a low open probability (~6%; **Fig. 2c**). In agreement with our previous observation that KTX occludes the KcsA-Kv1.3 pore[13], KcsA-Kv1.3 K^+ channel activity was completely inhibited by adding KTX to the cis side of the lipid bilayer (**Fig. 2b**). In symmetrical 150 mM K^+ solutions, chord conductances were 42 pS and 36 pS at +100 mV and –100 mV, respectively, and zero-voltage slope conductance was 52 pS. The lipid bilayer data concurred with our observation that the KcsA-Kv1.3 K^+ channel resides in proteoliposomes at pH 4.0 mostly in an inactivated state.

Next we monitored by ssNMR structural changes in KcsA-Kv1.3 that were associated with a change in pH from 7.5 to 4.0. Detailed ssNMR signal sets are shown in **Figure 3a** (left) documenting distinct spectral changes for residues in the

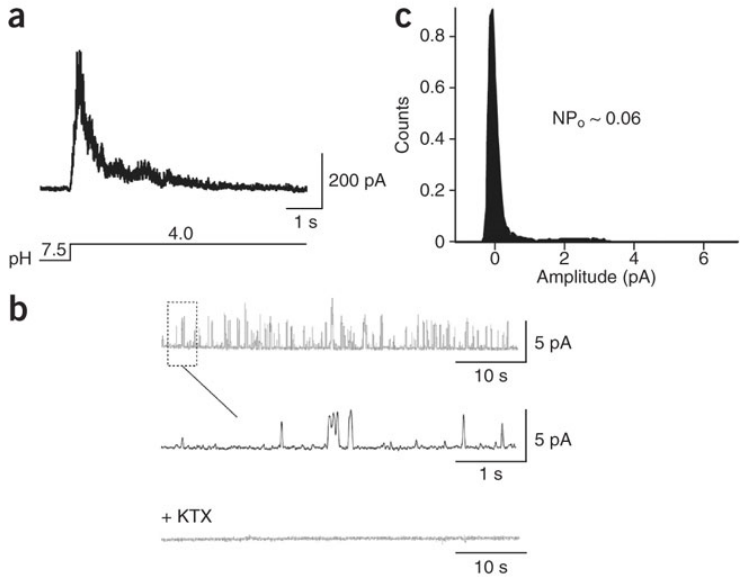

Figure 2. Inactivation and KTX binding properties of the KcsA-Kv1.3 channel. (***a***) KcsA-Kv1.3 current recorded from inside-out patches of proteoliposomes after jumping the pH from 7.5 to 4.0 at +100 mV in asymmetrical K^+ solutions (inside 200 mM KCl, outside 8 mM KCl). (***b***) Representative current traces from lipid bilayers containing KcsA-Kv1.3 channels shown in a slow timescale (above) and as a higher-resolution detail (middle). Traces were obtained at pH 4.0 on the *trans* side of the lipid bilayer and +100 mV in symmetrical 20 mM KCl solutions. Below, after addition of 100 nM KTX to the *cis* side of the lipid bilayer, KcsA-Kv1.3 channel activity was completely inhibited. (***c***) All-points amplitude histogram of single-channel recordings, such as that shown in b. Gaussian fits to the individual peaks were used to determine the nominal open probability (NP_o) of approximately 0.06 at pH 4.0.

selectivity filter, TM2 helix and turret regions. The bar diagram in **Figure 3b** (above) shows the complete set of differences in chemical shift for Cα resonances at pH 4.0 and 7.5. Alterations in side chain resonances are shown in **Figure 4**. We observed substantial chemical shift changes for the backbone of KcsA-Kv1.3 residues within the pore helix (Glu71, Thr72 and Ala73), selectivity filter (Thr74, Thr75, Val76, Gly77, Tyr78, Gly79 and Asp80), inner TM2 helix (Ala98, Gly99, Ile100, Thr101 and Gly116) and cytoplasmic C-terminal helix (Lys131). The magnitude of the backbone shift changes was >0.6 p.p.m., that is, large enough to be correlated with substantial structural alteration (for example, ref. 100). By contrast, differences in the chemical shifts were negligible for residues of the TM1 helix and turret, and for TM2 residues facing the extracellular side of the lipid bilayer. Notably, we observed attenuation of signals from some well-resolved residues in the turret and C-terminus (**Fig. 3b**, arrows). In particular, signals for residues Ala50, Glu51, Asp64, Tyr82, Ala132 and Glu135 could not be detected at pH 4.0. Taken together, in our ssNMR assignments, which covered 71% of the pore domain, only a subset of residues showed sizable chemical shift changes. We derived two major conclusions from our ssNMR analysis. First, pH-dependent gating of the KcsA-Kv1.3 channel is associated with defined local conformational changes. Second, these changes occur within functionally important regions of the K^+ channel, such as the bundle crossing, gating hinge and selectivity filter regions.

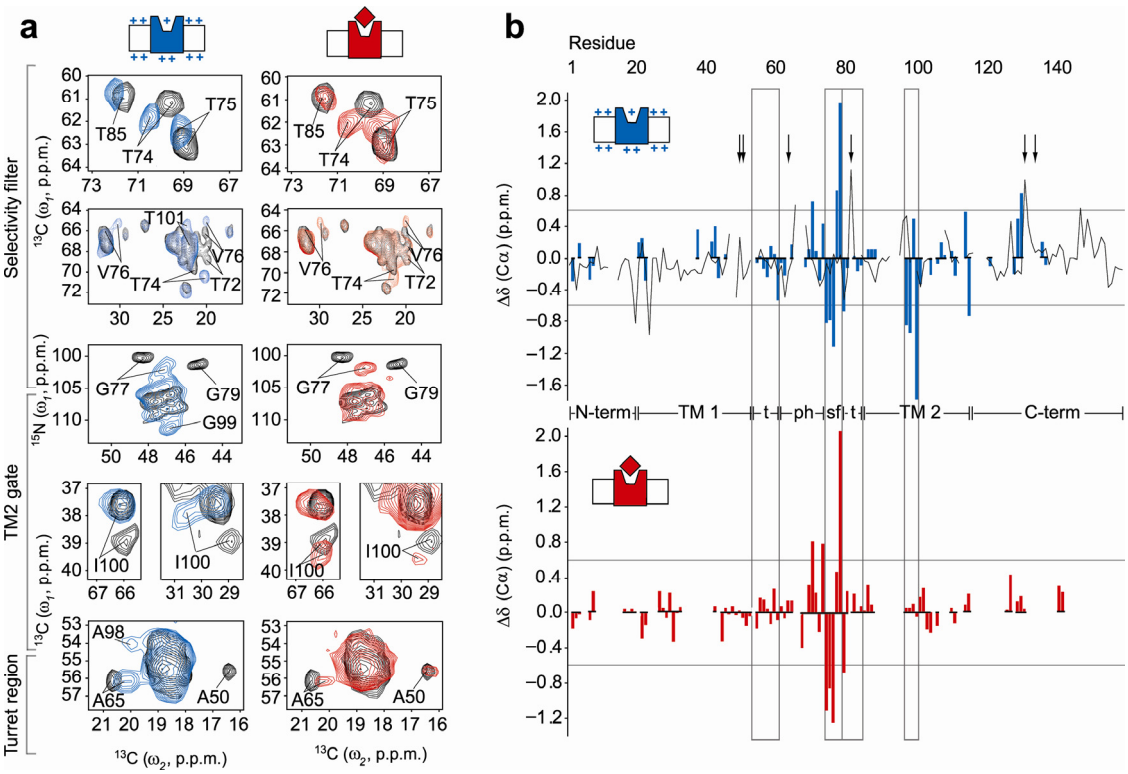

Figure 3. Comparison of ssNMR data for KcsA-Kv1.3 at pH 7.5, pH 4.0, and in the porphyrin-bound state. (***a***) Sections of homonuclear and heteronuclear ssNMR correlation spectra at pH 7.5 (black), pH 4.0 (blue, left) and with bound porphyrin (red, right). Resonances assigned to residues within the selectivity filter, pore helix, TM2 helix and turret regions are labeled. (***b***) Summary of Cα chemical shift changes observed for KcsA-Kv1.3 at pH 4.0 (blue, above) and with bound porphyrin (red, below) compared to pH 7.5. Horizontal lines at ± 0.6 p.p.m. indicate the threshold for substantial chemical shift changes. Lines in the center (N-term, N-terminus; TM1, transmembrane helix 1; t, extracellular turret; ph, pore helix; sf, selectivity filter; TM2, transmembrane helix 2; C-term, C-terminus) schematically show secondary structure along the sequence as seen in ssNMR. Grey frames highlight the selectivity filter, TM2 gating hinge and turret. Arrows point to residues not detectable at pH 4.0. For comparison, chemical shift changes between pH 7.0 and pH 4.0 described for KcsA in foscholine micelles[91] are shown above as a solid black line.

We did not attempt to derive high-resolution structural information from our data. However, the distinct relationship between the protein backbone structure and ssNMR Cα and Cβ chemical shift was used to evaluate structural changes associated with pH-dependent gating. For this purpose, we computed surfaces representing simulated secondary chemical shifts depending on the dihedral angles Φ and Ψ for selectivity filter (**Fig. 5a**) and gating hinge residues (**Fig. 5b**) using SHIFTX[101] (Methods). We then compared simulated to experimentally determined secondary chemical shifts.[100] Experimental values determined for KcsA-Kv1.3 at pH 7.5 (black) and pH 4.0 (blue) are given for selectivity filter and gating hinge residues in **Figure 5c** and **Figure 5d** respectively. In line with our earlier observation[13], secondary chemical shifts measured for KcsA-Kv1.3 at pH 7.5 agree well with their values (**Fig. 5a**,**b**, white circles) predicted on the basis of the crystal

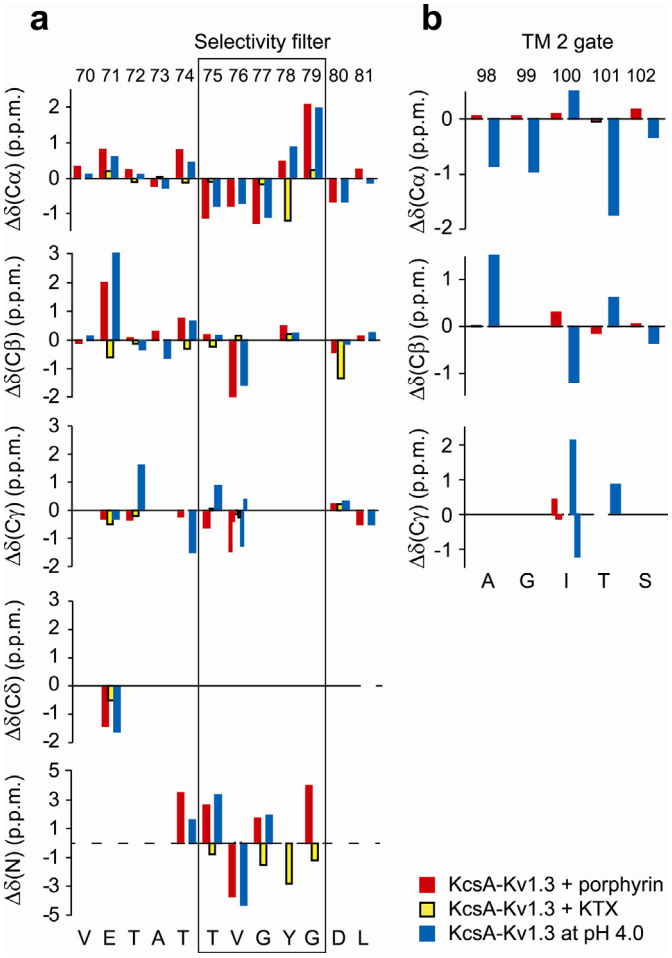

Figure 4. Chemical shift changes observed for residues in the selectivity filter (***a***) and the TM 2 gate (***b***) under different experimental conditions. Shown are data recorded at pH 4.0 (blue), with bound porphyrin (red), and KTX[13] (yellow) relative to free KcsA-Kv1.3 at pH 7.5. The selectivity filter is emphasized by a grey frame. Chemical shift changes for Cα, Cβ, Cγ, and Cδ ^{13}C resonances and peptide ^{15}N resonances (Δδ(Cα), Δδ(Cβ), Δδ(Cγ), Δδ(Cδ), and Δδ(N)) are in p.p.m.

structure of the closed KcsA K^+ channel[46] (PDB 1K4C; **Fig. 6a**,**b**). This idea is also supported by an investigation of proton-proton distances using NHHC and CHHC[30] ssNMR experiments at pH 7.5 (**Fig. 6c–e**), which yielded ten unambiguous distance constraints for the KcsA-Kv1.3 selectivity filter. The data are in excellent agreement with the conductive conformation of the selectivity filter in KcsA crystal structures.[46,69] Experimental secondary chemical shifts of residues Val70 to Leu81 are given in **Figure 5c** for the KcsA-Kv1.3 K^+ channel at pH 7.5 (black) and pH 4.0 (blue). Selectivity filter residues are highlighted and arrows indicate directions of changes in secondary chemical shift between pH 7.5 and pH 4.0. We repeated our approach to obtain from ssNMR data at pH 4.0 dihedral angle pairs for residues Thr75, Val76 and Tyr78 with optimal agreement between experimental (**Fig. 5c**) and simulated secondary chemical shifts (**Fig. 5a**, red squares). Using these dihedral angles as restraints for energy minimization of the selectivity filter in a CNS (Crystallography & NMR system[102]) simulated annealing protocol, we obtained dihedral angle values for Gly77 and Gly79. The respective simulated secondary chemical shifts for Gly77 and Gly79 were in close agreement with our experimental data (**Fig. 5a**, broken squares). The comparison of simulated and experimental secondary chemical shifts showed that backbone torsion angles were altered for selectivity filter residues Thr75, Val76, Gly77, Tyr78 and Gly79 by a few tens of degrees, indicating that the KcsA-Kv1.3 selectivity filter had adopted a

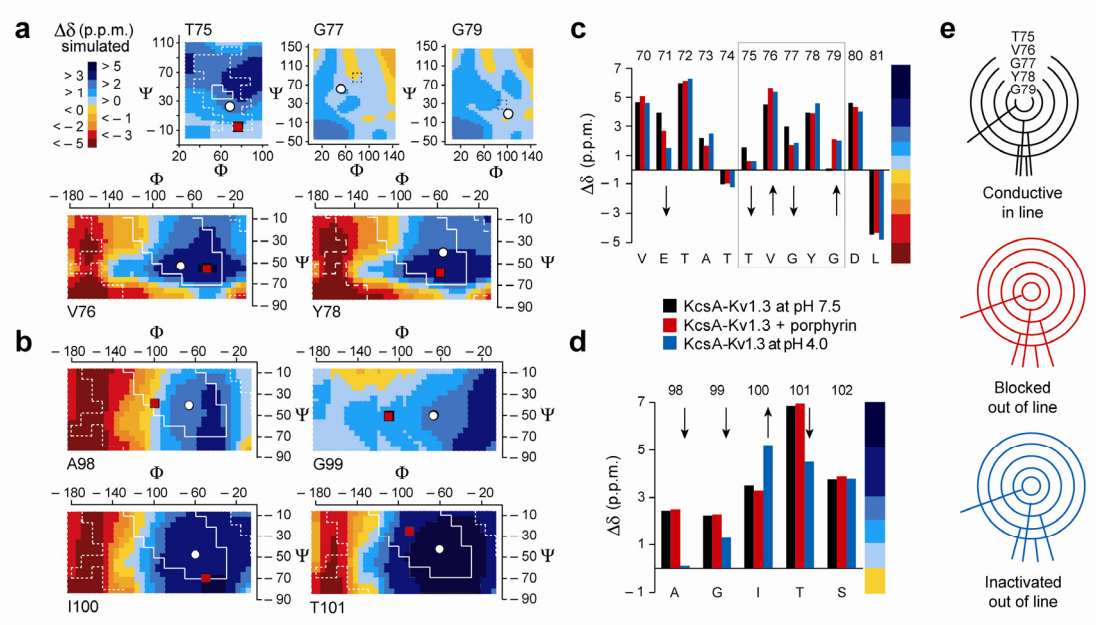

Figure 5. Analysis of changes in KcsA-Kv1.3 backbone conformation associated with pH-dependent gating and porphyrin binding. Surfaces representing simulated secondary chemical shifts depending on the dihedral angles Φ and Ψ for the residues composing the selectivity filter (***a***) and the TM2 gating hinge (***b***) are shown. White circles indicate dihedral angles for the crystal structure of KcsA (PDB 1K4C). Red or broken squares indicate dihedral angle pairs for which we find the best agreement between experimental and simulated secondary chemical shifts (for details, see text). Core (white, solid line) and allowed (white, dashed line) regions of the Ramachandran space are given according to ref. 103. Experimental secondary chemical shifts for KcsA-Kv1.3 at pH 7.5 (black), pH 4.0 (blue) and in the porphyrin-bound state (red) are given for residues Val70 to Leu81 (***c***) and residues Ala98 to Ser102 (***d***). Secondary chemical shifts are given in p.p.m. The grey outline in (c) indicates the selectivity filter. Arrows show directions of changes in secondary chemical shift. The color gradient allows for direct comparison to theoretical secondary chemical shifts plotted in (a) and (b). (***e***) Positional changes in backbone carbonyls of selectivity filter residues are shown, with a Newman-like projection highlighting C'- O bonds.

different conformation at pH 4.0. A hallmark of the conductive conformation of the selectivity filter (PDB 1K4C) is a regular alignment of backbone carbonyls. Observed chemical shift changes for residues lining the selectivity filter of inactivated KcsA-Kv1.3 most likely reflect movement of backbone carbonyls away from their in-line arrangement, as shown in **Figure 5e**. Positional changes in (unprotonated) backbone carbonyls of selectivity filter residues are undetectable in CHHC and NHHC experiments[30], which provided complementary information on the conductive conformation of the selectivity filter at pH 7.5 (ref. 46). NHHC and CHHC spectral data, obtained for the channel at pH 4.0, may be correlated with structural rearrangements involving the lower selectivity filter and gating hinge, but the corresponding cross correlations were ambiguous. Therefore, we did not include the data in our analysis.

KcsA crystal structures in different ionic solutions showed that the selectivity filter can potentially exist in two distinct, well-defined conformations, presumably

corresponding to a conductive and a nonconductive conformation.[46,104] In the nonconductive conformation, the backbone carbonyl group of Val76 has rotated away from the center of the pore, and the Cα of Gly77 faces toward the pore. As a result, the filter collapses shut.[46] This conformational change closely resembles that derived for the KcsA-Kv1.3 selectivity filter at pH 4.0. A principal conclusion from combining electrophysiological and structural data was that inactivation of the KcsA-Kv1.3 K^+ channel can be associated with a change in selectivity filter conformation that resembles the switch to the nonconductive conformation of the KcsA K^+ channel.

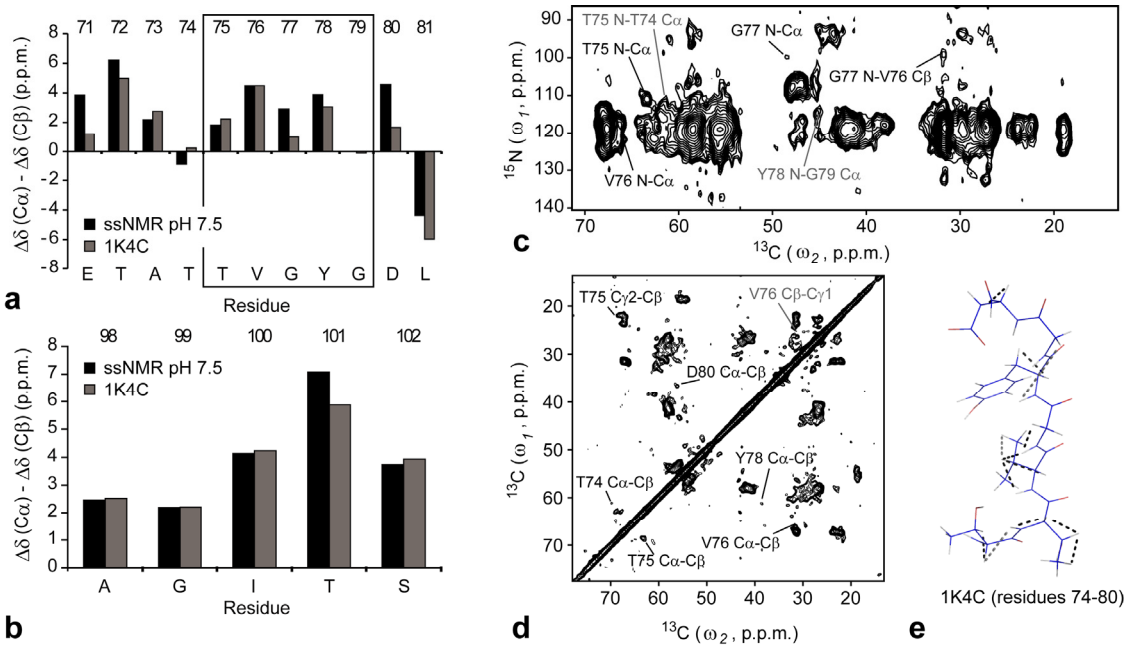

Figure 6. The KcsA-Kv1.3 channel conformation at pH 7.5. Comparison of experimental secondary chemical shifts (Δδ(Cα))-Δδ(Cβ)) between ssNMR assignments for KcsA-Kv1.3 in liposomes at pH 7.5 (black) and SHIFTX[101] predictions for the closed-conductive KcsA crystal structure[46] (grey, PDB ID 1K4C) for the selectivity filter (***a***) and for the TM2 gating hinge (***b***). The selectivity filter is marked by a grey rectangle. (***c***) NHHC (100 µs proton mixing) and (***d***) CHHC (50 µs proton mixing) spectra for the KcsA-Kv1.3 channel at pH 7.5. Signals corresponding to residues Thr74 to Asp80 are indicated (unambiguous: black, ambiguous: grey) and corresponding distances are indicated by lines in the filter structure of conductive KcsA (PDB ID 1K4C) (***e***).

For the gating hinge region in TM2, an analogous analysis indicated changes in dihedral (Φ, Ψ) angles by 20° on average for four consecutive residues (Ala98, Gly99, Ile100 and Thr101) (**Fig. 5b**). Dihedral angles obtained for the backbone of the gating hinge correspond to a bend in the inner TM2 helix in good agreement with structures of K^+ channels crystallized in an open conformation.[69,70,105] It is likely that bending the TM2 helix is coupled to swinging out the lower part of the TM2 helix. In agreement with this picture, we generally did not observe large Cα and Cβ chemical shift changes for the backbone of residues in the lower TM2 helix. Opening of the inner TM2 helix bundle is associated with opening the

activation gate at the cytoplasmic entrance to the pore of the channel.[69] Consistent with this interpretation of the data is the occurrence of substantial chemical shift changes for residues in the C-terminal part of the TM2 helix (Gly116) and in the intracellular C-terminus (Lys131) (**Fig. 3b**).

Localized conformational changes associated with ligand binding

Notably, similar chemical shift changes associated with the nonconductive conformation of the KcsA-Kv1.3 selectivity filter at pH 4.0 were observed upon binding a water-soluble tetraphenylporphyrin derivative[90] (#3, R = HN-$(CH_2)_2$-NH_2, in the following denoted porphyrin) to KcsA-Kv1.3 (**Fig. 3a**, right, and **Fig. 3b**, below) at pH 7.5. The porphyrin ligand binds to the Kv1.3 K^+ channel with nanomolar affinity and inhibits its activity. In competition[90] binding experiments, we showed that porphyrin displaces a high-affinity pore blocker such as ^{125}I-KTX (ref. 13). The competition binding curve for KcsA-Kv1.3 (**Fig. 7a**) was well described assuming a 1:1 stoichiometry and a direct displacement of ^{125}I-KTX by porphyrin with an EC_{50} of 240 nM. The data showed that both KcsA-Kv1.3 and Kv1.3 (ref. 90) K^+ channels had a similar affinity for the porphyrin ligand. ssNMR signal sets were obtained before and after addition of the porphyrin ligand to KcsA-Kv1.3 in proteoliposomes (pH 7.5; **Fig. 3a**, right). We obtained assignments of 53% of all channel residues in the porphyrin-bound case. Changes in chemical shifts were restricted to selectivity filter residues and closely resembled values seen for free KcsA-Kv1.3 K^+ channels at pH 4.0 (**Fig. 3b**, below). Except for Thr75 (Cα, Cβ) resonances, for which we observed a small peak splitting (**Fig. 3a**), peak splittings were generally not detected. To rule out the possibility that spectral variations seen upon addition of porphyrin reflected an indirect effect on the conformation of the selectivity filter, we used ^{15}N-labeled porphyrin to further probe the local ^{1}H environment of the ligand by two-dimensional ssNMR. Frequency-switched Lee-Goldburg[106] ^{1}H-^{15}N correlation experiments were conducted with porphyrin in an asolectin liposome environment in comparison to porphyrin bound to KcsA-Kv1.3 in liposomes (**Fig. 7b**). Results for unbound porphyrin corroborate ^{1}H chemical shift data (data not shown) indicative of a porphyrin coordination in the lipid headgroup region. For KcsA-Kv1.3-bound porphyrin, intramolecular magnetization transfer to the amine protons of porphyrin was more efficient. By contrast, magnetization transfer from water was apparently reduced. Also, we observed proton resonances below 1 p.p.m. for bound porphyrin that corresponded to protein side chain protons. In summary, the results showed spectroscopic changes reflecting an increased rigidity of porphyrin arms bound directly to the KcsA-Kv1.3 K^+ channel.

Subsequently, an *in silico* molecular dynamics-based ligand-protein docking[107] was conducted with residues showing considerable chemical shift changes defined as interaction surface. All 200 water-refined structures showed the same binding mode of porphyrin to the KcsA-Kv1.3 K^+ channel with one of the four arms of the porphyrin penetrating into the selectivity filter, where the protonated amine favorably interacts with K^+ binding site S3 (**Fig. 7c,d**). This binding model has two principal implications. First, K^+ binding site S3 lies deep inside the membrane's electric field; therefore, the affinity of porphyrin to K^+ channels should be voltage sensitive. Second, porphyrin spares a substantial part of the available space around the extracellular entrance of the KcsA-Kv1.3 pore. On the basis of this observation

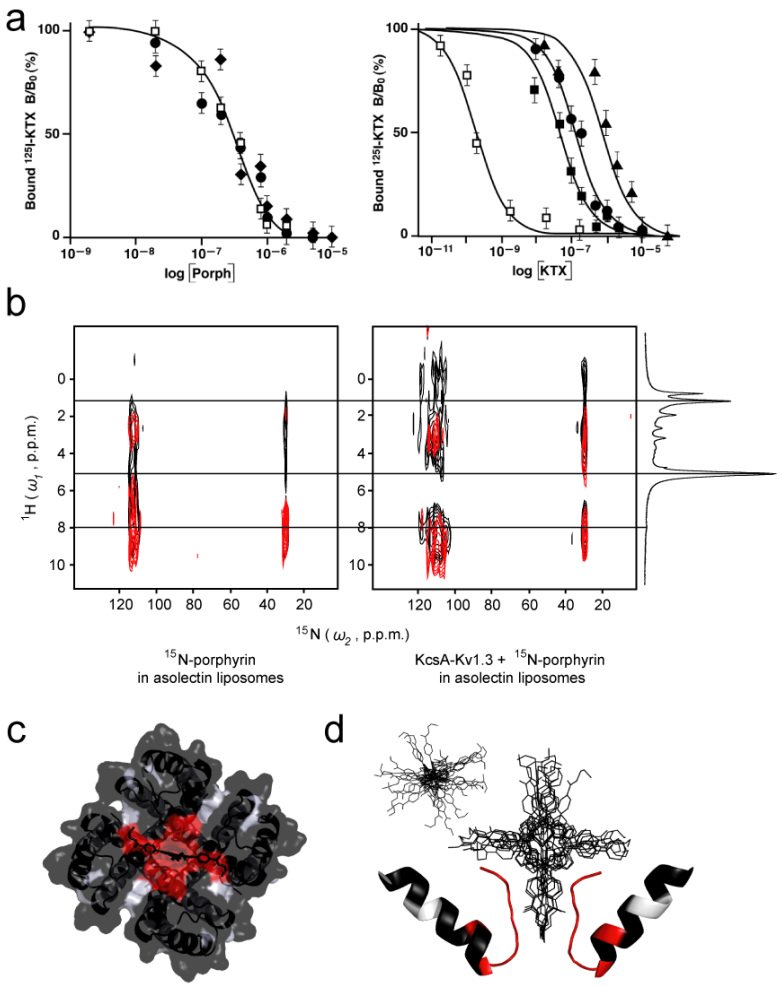

Figure 7. Analysis of porphyrin binding to KcsA-Kv1.3. (***a***) Left, binding of ^{125}I-KTX to purified KcsA-Kv1.3 (□), KcsA-Kv1.3 G58A (●) or KcsA-Kv1.3 G58V (♦) in the absence (B_0) or presence (B) of porphyrin #3 (Porph).[90] Right, binding of ^{125}I-KTX to purified KcsA-Kv1.3 (□), KcsA-Kv1.3 G58A (■), KcsA-Kv1.3 G58V (●) or KcsA-Kv1.3 G58F(▲) in the absence (B_0) or presence (B) of KTX. Error bars indicate s.e.m. (***b***) Frequency-switched Lee-Goldburg[106] (^{1}H, ^{15}N) HETCOR experiments with an additional proton mixing time for selectively ^{15}N-labeled porphyrin free in asolectin liposomes (left) and channel bound (right). Spectra are shown for 100 µs proton mixing (red) and 500 µs proton mixing (black). The one-dimensional ^{1}H spectrum of free porphyrin in asolectin liposomes is given at the far right, and the horizontal lines are included to guide the eye. (***c***, ***d***) Surface representation (top view) of KcsA-Kv1.3 bound to the porphyrin (c) and overlay of the ten lowest-energy structures according to HADDOCK[107] docking (d). Residues for which substantial chemical shift changes have been observed are red; residues for which no chemical shift changes have been observed are black.

and in contrast to earlier views[90], we inferred that porphyrin binding should be relatively insensitive to sterical constraints introduced by mutations at strategical positions in the turret region. To test this hypothesis, we systematically increased the side chain volume of residue Gly58 in the turret region by mutation to alanine, valine or tryptophan. In competition binding experiments with ^{125}IKTX, we

observed that KcsA-Kv1.3 affinity for porphyrin was insensitive to an increase in side chain volume at residue Gly58 (**Fig. 7a**). By contrast, Gly58 mutations decreased KcsA-Kv1.3 affinity for KTX by up to four orders of magnitude (**Fig. 7a**). Next, we investigated voltage sensitivity of porphyrin binding with Kv1.3 channels. We measured the time constants t_{on} for the onset of porphyrin block and t_{off} for porphyrin washout at different test voltages. From the data, we calculated binding constants $K_d(E)$ for the porphyrin block of the Kv1.3 channel. A linear plot of the logarithm of $K_d(E)$ versus voltage yielded, using the Woodhull equation[108], an average value of 0.47 for d, the fraction of membrane potential acting at the porphyrin binding site. The result indicated excellent agreement with our model that part of the porphyrin moiety was approximately halfway down the membrane electric field experienced by the K^+ channel pore.

Besides its high affinity towards the KcsA-Kv1.3 channel, the porphyrin also associates with lipid membranes. In order to characterize this secondary binding event, we determined ^{1}H-^{1}H cross relaxation rates between the porphyrin and 1,2-dimyristoyl-*sn*-glycero-3-phosphocholine (DMPC) liposomes (**Fig. 8a-d**) under MAS. Based on these parameters we deduced the binding mode of the porphyrin to the lipid bilayer. The porphyrin core is located closed to the glycerol part of the lipids while the positively charged arms point into the aqueous environment (**Fig. 8e**).

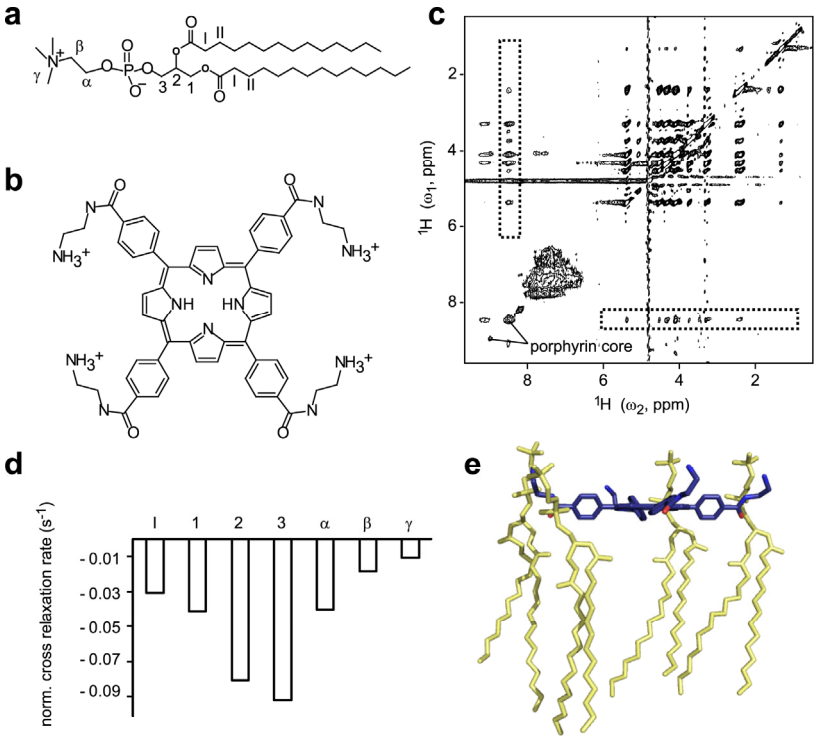

Figure 8. Study of porphyrin-lipid interaction. Structures of DMPC with atom nomenclature (***a***) and porphyrin (***b***). (***c***) NOESY spectrum of DMPC:porphyrin (10:1, mol:mol) obtained for a ^{1}H-^{1}H mixing time of 250 ms under MAS. Intermolecular cross peaks between lipid resonances and resonances due to the porphyrin core are labeled by dashed boxes. (***d***) Normalized per ^{1}H cross relaxation rates computed for the porphyrin core to spins of the DMPC head group. (***e***) Model for the binding mode of the porphyrin to the lipid bilayer as seen from ^{1}H-^{1}H cross relaxation rates.

Discussion

Understanding structural alterations that accompany gating of ion channels is a key issue in ion channel physiology and biophysics. Here we have studied the conformational changes that occur during gating of a functional K^+ channel at the atomic level using ssNMR spectroscopy of KcsA-Kv1.3 channel preparations in liposomes. We have shown that the KcsA-Kv1.3 channel is closed at pH 7.5, and that it is opened by an increase in intracellular H^+ concentration, as seen for the parent KcsA channel. The activated KcsA-Kv1.3 K^+ channel rapidly entered into an inactivated state during a persistent H^+ stimulus. Thus, the KcsA-Kv1.3 K^+ channel predominantly resides under steady-state conditions at pH 7.5 in a closed state and at pH 4.0 in an inactivated state. Our ssNMR experiments conducted on the two channel states showed distinct conformational differences in channel domains that are of prime importance for K^+ channel gating, such as the selectivity filter, gating hinge and inner helix bundle. These differences are likely to reflect conformational changes associated with a transition from a closed to an inactivated state of the KcsA-Kv1.3 K^+ channel.

Previous work established that conformational transitions occurring in the selectivity filter are related to K^+ channel inactivation.[79] The selectivity filter has the potential to adopt two distinct, well-defined structures corresponding to a conductive and a nonconductive conformation, respectively. The two conformations are coupled to K^+-ion occupancy in the filter, particularly at K^+-selective sites 2 and 3. At low K^+ concentration, the selectivity filter attains a nonconductive conformation[46,104,109] which might be related to C-type inactivation.[46,79,104] A similar conformation in the selectivity filter is seen in our KcsA-Kv1.3 preparations at pH 4.0. Additional structural alterations were detected in the pore helix on the backside of the filter involving interactions between Glu71 and Asp80. This is in excellent agreement with mutational and biophysical studies, which indicate a hydrogen bond network behind the selectivity filter that promotes the inactivated state of the KcsA K^+ channel.[85-88] The strength of the interaction between Glu71 and Asp80, which are connected within this network by a water-mediated carboxyl-carboxylate interaction, has a key role in inactivation gating.[87] We observed sizable chemical shift changes for residues Glu71 and Asp80 associated with pH-induced gating of the KcsA-Kv1.3 K^+ channel. In our data, the ^{13}C resonance of the side chain carboxyl group of Glu71 in particular experiences a change to a smaller isotropic chemical shift, indicative of increased protonation as expected for strengthened hydrogen-bonding at pH 4.0. After a pH change from 7 to 4, a recent NMR study using KcsA K^+ channel preparations in foscholine micelles[91] reported only subtle structural changes regarding the hydrogen bond network between Tyr78, Gly79, Glu71 and Asp80. The differences between solution and ssNMR data may not be surprising if we consider that membrane proteins require a special membrane setting to function. Possibly, the conformation of KcsA in micelles is intrinsically unstable at pH 4.0 (as observed for SDS micelles at pH 4.2 (ref. 92)) and fluctuates between a permeating and nonpermeating conformation. By contrast, the KcsA-Kv1.3 K^+ channel attains in liposomes a more stable, nonconducting conformation, in which the inner helix shows an opened activation gate and the selectivity filter has collapsed shut (**Fig. 9a**, **b**). Upon binding of porphyrin to the KcsA-Kv1.3 K^+ channel at pH 7.5, we

observed chemical shift changes indicating a selectivity filter in a nonconductive conformation. We obtained a structural model for the porphyrin–channel complex (**Fig. 9c**), where the porphyrin moiety inserts one of its four positively charged arms deeply into the selectivity filter, displacing K^+ ions from binding sites within the selectivity filter, which are likely to include K^+-selective sites 2 and 3. This observation was fortunate, because it tells us that different conditions, such as a change in pH and ligand binding, can induce a nonconductive conformation in the selectivity filter. The underlying common principle seems to be that both inactivation and channel block generate a low K^+ occupancy in the selectivity filter. Consistent with a large body of functional K^+ channel data[79,85,87], we conclude that inactivation gate closure can be associated with a switch from a conductive to a nonconductive conformation in the selectivity filter. We propose that this event is accompanied by distinct alterations in backbone structure such that the carbonyl oxygen atoms are moved out of line, disrupting K^+ ion binding and conduction. The structural changes inferred from our ssNMR analysis, however, are smaller than those predicted from molecular dynamics simulations[84] or those seen in a crystal structure of a non-inactivating KcsA mutant.[85] Previously, we showed[13] that KTX binding to the extracellular mouth of the pore is characterized by structural alterations near and at the entrance to the selectivity filter. Porphyrin competes with KTX for binding to the extracellular entrance to the pore of both Kv1.3 channels[90] and KcsA-Kv1.3. The structural data presented here showed that, in contrast to KTX, porphyrin penetrates deeply into the selectivity filter, in excellent agreement with our observation that porphyrin binding to Kv1.3 channels is strongly voltage-dependent, whereas KTX binding is not. Apparently, the two blockers elicit markedly different conformational changes because they penetrate the selectivity filter to a different extent. In comparison to the porphyrin-bound state of the KcsA-Kv1.3 K^+ channel, the ssNMR data obtained at pH 4.0 indicate unique pH-induced structural alterations in the KcsA-Kv1.3 pore domain. These include side chain changes for residues in the lower part of the selectivity filter and the pore helix, as well as additional conformational changes in backbone and side chains of residues within the intracellular half of the KcsA-Kv1.3 K^+ channel. Here, the structural data were consistent with those derived from crystal structures for opened K^+ channel conformations[69,70,89] (**Fig. 9a,b**). In particular, secondary chemical shift analysis indicated bending of the inner TM2 helix at the highly conserved gating hinge around residue Gly99. Bending at a gating hinge of the inner TM2 helix has been attributed a key role in opening the activation gate associated with the inner helix bundle.[69] Direction and magnitude of the bend in the KcsA-Kv1.3 TM2 helix are consistent with the idea that the inner helix bundle of the KcsA-Kv1.3 K^+ channel adopts an opened conformation at pH 4.0. The implication then is that the KcsA-Kv1.3 channel shows an opened activation gate and a collapsed selectivity filter in good agreement with a recent proposal for the conformation of the inactivated KcsA K^+ channel characterized by an opened activation and a closed inactivation gate.[87] The observed changes in side chain chemical shifts for residues in the gating hinge, pore helix, and lower selectivity filter regions suggest that steric interaction between the two gates is possible.

In summary, we used ssNMR to follow structural changes associated with K^+ channel gating in a lipid bilayer environment in direct reference to electrophysiological experiments. The conformational changes were confined to

distinct regions of the channel, providing a direct glimpse at structural changes underlying fundamental aspects of the workings of an ion channel in a membrane setting.

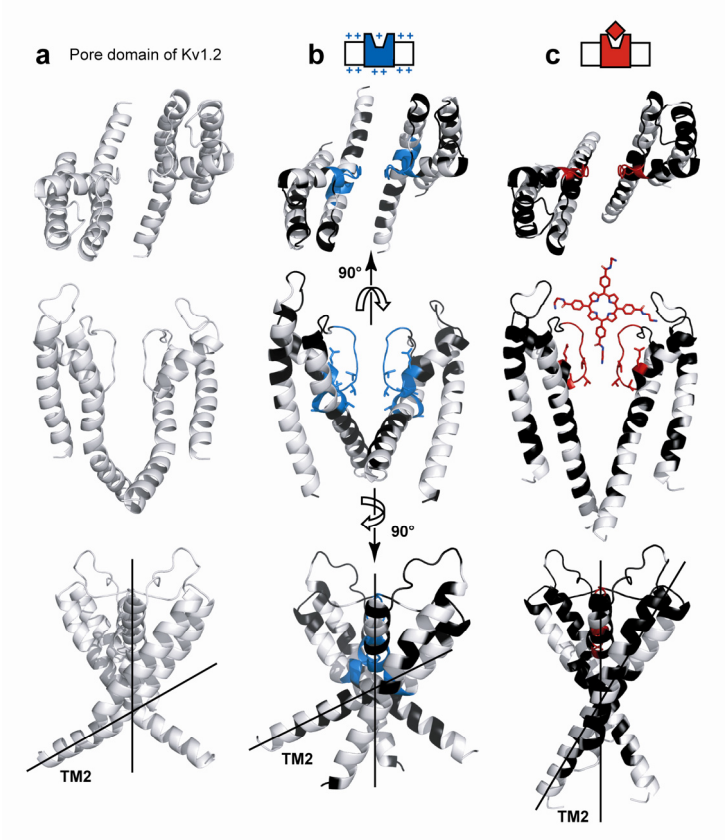

Figure 9. Structural models for the KcsA-Kv1.3 channel at pH 4.0 and with bound porphyrin at pH 7.5. For comparison, the crystal structure of the pore domain of Kv1.2 (ref. 70; PDB ID 2A79) is shown in ***a***. Residues for which Cα chemical shift changes have been observed are blue (***b***, pH 4.0) and red (***c***, porphyrin-bound). Residues for which no Cα chemical shift changes larger than 0.6 p.p.m. have been found are black; unassigned residues are grey. Side chains are indicated for residues with considerable side chain chemical shift changes. Lines in the bottom row represent the four-fold symmetry axis of the channel and the helical TM2 axis, highlighting the structural reorientation of the TM2 helix associated with a bend in the TM2 gating hinge.

Materials and Methods

Sample preparation. We carried out KcsA-Kv1.3 expression, purification and reconstitution into asolectin liposomes as described previously[13]. Samples at pH 4.0 were prepared by washing proteoliposomes with 100 mM citrate buffer, yielding the same ionic strength as the phosphate buffer used for pH 7.5 samples. Porphyrin-bound samples were prepared by adding porphyrin #3 (ref. 90) in two-fold molar excess to KcsA-Kv1.3 reconstituted in asolectin liposomes at pH 7.5. Samples were washed thoroughly with the respective buffer before ultracentrifugation and packing into standard 4 mm rotors for magic angle

spinning. To study porphyrin-lipid interaction partially deuterated 1,2-dimyristoyl-D54-sn-glycero-3-phosphocholine (DMPC) was purchased from Avanti Polar Lipids, Inc. (Alabaster, AL) and samples were prepared with a porphyrin:DMPC ratio of 1:10. This sample contained approximately 60 mass% D_2O.

Solid-state nuclear magnetic resonance. We conducted all NMR experiments using 4 mm triple-resonance (^{1}H, ^{13}C, ^{15}N) probeheads at static magnetic fields of 14.1 T and 18.8 T corresponding to 600 MHz and 800 MHz proton resonance frequencies (Bruker Biospin). Assignments were obtained using two-dimensional and three-dimensional (^{13}C, ^{13}C) and (^{15}N, ^{13}C) correlation experiments, as described in detail in ref. 10. (^{13}C, ^{13}C) correlations were obtained using proton-driven spin diffusion under weak coupling conditions (PDSD-WC)[19], whereas (^{15}N, ^{13}C) spectra were recorded using SPECIFIC-CP[20], with and without subsequent DARR[27] mixing for obtaining side chain ^{13}C resonances. Through-space constraints for the selectivity filter at pH 7.5 were obtained via NHHC and CHHC[30] experiments using 100 μs and 50 μs (^{1}H, ^{1}H) mixing times, respectively. The local environment of porphyrin, which was ^{15}N-labeled in the amide and amine of the four arms, both free in asolectin liposomes and bound to reconstituted KcsA-Kv1.3, was probed via (^{1}H, ^{15}N) heteronuclear correlation experiments using frequency-switched Lee-Goldburg[106] proton decoupling and additional (^{1}H, ^{1}H) mixing times of 100 μs and 500 μs. Two-dimensional MAS NOESY experiments were acquired with 300 t_1 experiments and 24 scans per t_1 increment. In order to obtain cross-relaxation rates, integral intensities of diagonal peaks were determined for mixing times close to zero (5μs) and 250ms using TopSpin (Bruker Biospin). The relaxation rate matrix **R** can be calculated using matrix algebra according to the matrix equation $\mathbf{A}(t_m) = \exp(-\mathbf{R}t_m)\mathbf{A}(0)$, where $\mathbf{A}(0)$ is the diagonal peak intensity matrix at zero mixing time.[110,111] For N magnetically nonequivalent spins **R** is

$$R = \begin{pmatrix} \rho_{11} & \sigma_{12} & \sigma_{13} & \cdots & \sigma_{1N} \\ \sigma_{21} & \rho_{22} & \sigma_{23} & & \\ \sigma_{31} & \sigma_{32} & \rho_{33} & & \vdots \\ \vdots & & & \ddots & \\ \sigma_{N1} & & \cdots & & \rho_{NN} \end{pmatrix}$$

where σ_{ij} is by convention the cross-relaxation rate of magnetization transfer from spin *j* to *i* and ρ_{ii} is the effective relaxation rate of the diagonal peak due to spin *i*. In order to allow for relative comparability per proton transfer rates, Γ_{ij}, were computed by dividing the cross-relaxation rate σ_{ij} by the relative number of *i* spins n_i. MAS speeds used were 9.375 kHz and 12.5 kHz at 14.1 T and 18.8 T static magnetic field strengths, respectively, at effective sample temperatures of approximately +10 °C (liquid crystalline state) or –10 °C (frozen state). NOESY experiments were acquired at 18.8 T employing 11 kHz MAS at about +10°C. The typical proton field strength for 90° pulses and SPINAL64[77] decoupling was 83 kHz.

Structural analysis and protein docking. To analyse changes in the backbone dihedral angles upon pH change to pH 4.0 and porphyrin binding, we simulated secondary chemical shifts for the respective areas of Ramachandran space using the SHIFTX[101] software and compared them to experimentally measured secondary chemical shifts. For every residue in the selectivity filter and the TM2 gate, Φ and Ψ angles were altered independently in steps of 5°. The generated conformations were analyzed by the SHIFTX software, and secondary chemical shifts were calculated as defined previously.[100] For the selectivity filter and the TM2 gate of KcsA-Kv1.3 at pH 4.0, we selected simulated dihedral angle pairs that were closest to experimentally determined values and required the smallest angular change compared to pH 7.5. Owing to the large conformational space available to glycine residues, our shift analysis did not yield an unambiguous result for the dihedral angles of Gly77 and Gly79 at pH 4.0. For this reason, we calculated a set of 500 structures of the selectivity filter using simulated annealing in CNS[102]. Gly77 and Gly79 were allowed to adjust freely, whereas dihedral angles of residues Thr75, Val76 and Tyr78 were restricted to a small region in the Ramachandran plot close to the values found previously in the secondary chemical shift analysis. All other atoms were kept fixed except residues Thr74 and Asp80 to allow for a smooth transition between flexible and rigid protein segments. Resultant structural models were selected on the basis of their overall energy as determined by CNS and a SHIFTX prediction of Gly77 and Gly79 Ca chemical shifts close to experimental values (deviations up to 1.5 p.p.m. accepted). Using PyMOL (http://pymol.sourceforge.net), obtained dihedral angles were introduced manually in the crystal structure of KcsA (PDB 1K4C) containing the 11 mutations of KcsA-Kv1.3 to create the structural model shown in **Figure 9**.
A model of the porphyrin–KcsA-Kv1.3 complex was calculated using the docking program HADDOCK 1.3[107]. The input structure for KcsA-Kv1.3 was generated by introducing 11 mutations to the crystal structure of KcsA (PDB 1K4C) using the PyMOL software. Topology files for the porphyrin were generated using the PRODRG2 server[112] and adjusted manually. The chemical shift changes exceeding 0.6 p.p.m. observed for KcsA-Kv1.3 upon complex formation were used to define active residues. The porphyrin was set up as one residue. Ambiguous interaction restraints (AIRs) were defined between every active residue of KcsA-Kv1.3 and the porphyrin. Residues 50–105 in each subunit of KcsA-Kv1.3 were defined as interface and semiflexible, whereas the porphyrin was set to be fully flexible during all stages of the simulated annealing protocol. We generated 200 structures using rigid-body docking and subsequently performed a semiflexible refinement in torsion angle space. Standard settings were used in the HADDOCK-simulated annealing protocol. As all models obtained from the simulated annealing refinement showed the same binding mode for the porphyrin bound to KcsA-Kv1.3, all 200 structures were chosen for explicit solvent refinement in water. The final structures were ranked on the basis of total energy.

Liposome patch clamp. For electrophysiological measurements on KcsA-Kv1.3 in proteoliposomes, we followed the method of ref. 113 with modifications described in ref. 13. Currents were measured at a 1:100 protein:lipid ratio (mass:mass). Patch-clamp measurements were done at room temperature in asymmetrical conditions with 8 mM KCl, 192 mM NaCl and 10 mM MOPS buffer (pH 7.0) in

the pipette and 200 mM KCl and 10 mM MOPS buffer (pH 7.0) in the bath. Currents were recorded after a jump to pH 4.0 with 200 mM KCl, 10 mM sodium acetate (pH 4.0) with an EPC-9 (HEKA) amplifier. Pipette resistances were 1–2 MΩ. Sampling rates were 1 kHz.

Lipid bilayer studies. Fusion of purified KcsA-Kv1.3 channels with planar lipid bilayers and current measurements were done as described previously.[45] The electrode of the trans compartment was mounted on the headstage (CV-5B-100G) of a current amplifier (GeneClamp 500, Axon Instruments). Current recordings were low-pass filtered at 1–2 kHz and digitized at a sampling rate of 40 kHz. Data were evaluated using IGORPro 6.03 (Wavemetrics) software.

Two-electrode voltage clamp. Kv1.3 cRNA (50 ng μl^{-1}) prepared from Kv1.3 cDNA (Genbank NM_019270) with the mMESSAGE mMACHINE T7 kit (Ambion) was injected into defolliculated stage IV and V *Xenopus laevis* oocytes essentially as described[13]. Unless otherwise stated, Kv1.3-mediated outward currents were measured at –60 mV to + 60 mV test potentials in 10 mV increments from a holding potential of –80 mV at 16 °C. Bath solution was 20 mM RbCl, 80 mM NaCl, 1 mM $MgCl_2$, 0.3 mM $CaCl_2$ and 5 mM HEPES (pH 7.6). Porphyrin dissolved in bath solution containing 1% (w/v) dimethylsulfoxide was added by bath perfusion. Concentrations varied between 0.01 μM and 2 μM. Currents were recorded using an EPC9 amplifier (HEKA). Data were filtered at 2 kHz and digitized at 5 kHz. Binding data were evaluated using HEKA-PULSEFIT in combination with Kaleidagraph (SynergySoftware) and Mathcad (Mathsoft Engineering & Education, Inc.) software.

Binding studies. Channels were mutated, expressed and purified as previously described[14] using a pQE32 vector containing KcsA-Kv1.3 with the RGS-His_6 epitope at the N terminus. In binding experiments, KcsA-Kv1.3 protein (10 ng to 10 μg per assay) was incubated for 1 h at room temperature in binding buffer containing 2 mM n-decyl-β-D-malto-pyranoside with 40 pM to 10 nM ^{125}I-KTX and a series of cold KTX or porphyrin concentrations (0.1 pM to 10 μM) in a total volume of 250 μL. Reactions were stopped and binding was measured essentially as described previously.[13] Data were evaluated using Kaleidagraph and Mathcad software.

Chapter 4

Coupling of activation and inactivation gate in a K^+ channel: potassium and ligand sensitivity

Christian Ader[1,2]
Robert Schneider[2]
Sönke Hornig[3]
Phanindra Velisetty[3]
Vitya Vardanyan[3]
Karin Giller[2]
Iris Ohmert[3]
Stefan Becker[2]
Olaf Pongs[3]
Marc Baldus[1,2]

[1] Bijvoet Center for Biomolecular Research, Utrecht University, The Netherlands
[2] Max-Planck-Institute for Biophysical Chemistry, Germany
[3] University Hospital Hamburg-Eppendorf, Germany

EMBO Journal **in press**

Abstract

K^+ channel gating is choreographed by a complex interplay between external stimuli, K^+ concentration and lipidic environment. We combined solid-state NMR and electrophysiological experiments on a chimeric KcsA-Kv1.3 channel to delineate K^+-, pH- and blocker-effects on channel structure and function in a membrane setting. Our data show that pH-induced activation is correlated with protonation of glutamate residues at or near the activation gate. Moreover, K^+ and channel blockers distinctly affect the open-probability of both the inactivation gate comprising the selectivity filter of the channel, and the activation gate. The results indicate that the two gates are coupled and that effects of the permeant K^+ ion on the inactivation gate modulate activation gate opening. The data suggest a mechanism for controlling coordinated and sequential opening and closing of activation and inactivation gates in the K^+-channel pore.

Introduction

Potassium (K^+) channel activation plays an important role in neural signal transduction as it regulates selective conduction of K^+ across biological membranes.[114] In response to changes in chemical or electrical potential the pore domain of K^+-channels opens and closes, thereby controlling K^+ access to the pore.[79,115] K^+ channels have a common pore design which includes presence of an activation gate at the intracellular entrance of the pore and of a separate inactivation gate situated towards the extracellular entrance at the selectivity filter. Gating of the K^+ channel involves structural rearrangements at the two gates. The activation gate is associated with the inner helix bundle that moves during activation around a gating hinge[47,61,69,71,116-121], while closing of the inactivation gate concurs with rearrangements at the selectivity filter to enter an inactivated state of the K^+ channel.[71,84-88,122-128] In the family of voltage-gated K^+ (Kv) channels, opening and closing of activation and inactivation gate were shown to be coupled.[129-132] It is likely that coupling between the two gates ensures maximum channel open-probability and also sequentially coordinates activation and inactivation gating of the K^+ channel.

The bacterial K^+ channel KcsA[45-47] provides a powerful and robust model system for a detailed investigation of channel gating. Studies of KcsA mutants have identified amino-acid residues involved in KcsA-channel gating.[87,133] In the resting state the activation gate of the channel is closed and the inactivation gate is opened, that is, the selectivity filter has a conductive structure. Acidic pH elicits activation-gate opening and thus an activated state of the KcsA-channel.[61,71,86,88,91,119] The state is short-lived because the inactivation gate rapidly closes the filter of the activated K^+ channel. According to solid-state (ss) NMR, the inactivated filter conformation shares essential features with the collapsed or non-conductive filter structure seen in KcsA crystal structures obtained in low [K^+] (**Chapter 3**).[46,104,109]

The influence of external [K^+] on selectivity filter stability and K^+ channel gating, e.g. C-type inactivation of *Shaker* channels, has been extensively studied on a functional level.[124,128,134-136] However, how sequential gating activity of the two gates in the K^+ channel pore domain is choreographed and affected by the permeant ions is not well understood. A comprehensive understanding of channel gating,

hence, should involve structural studies that delineate the cumulative effect of pH and K^+ concentration in a functional lipidic environment. We have previously shown that under such conditions, high-resolution solid-state (ss) NMR-spectroscopy is a sensitive method for analyzing ligand binding and conformational changes related to pH-induced activation and inactivation gating.[13,71] Here, we used ssNMR chemical-shift mapping in direct reference to electrophysiological recordings on KcsA-Kv1.3 preparations to dissect the pH-, K^+-, and ligand-sensitivity of channel gating. We found that pH-induced gating of KcsA-Kv1.3 is modulated by the concentration of external as well as internal K^+. Correspondingly, distinct potassium binding events affect inactivation and activation gating of the K^+ channel. Using ssNMR, we studied these gating states in lipid bilayers by tracking K^+- and pH-dependent changes in protein conformation and side-chain protonation. Moreover, we probed coordinated actions of opening and closing of the two gates by trapping the K^+ channel in distinct states with external pore blockers.[13,71] We observed that pH, K^+, and the scorpion toxin kaliotoxin (KTX) strongly influence the open probability of the activation gate. While the effect of pH relates to protonation of glutamate residues located in the intracellular "pH sensor" of the channel, the effects of K^+ and KTX are mediated via distinct binding sites within or near the selectivity filter. Thus, we show that the inactivation gate can influence activation gating and that gate coupling based on sidechain interactions between the two gates allows for a choreographed response to K^+. These findings propose a self-regulatory mechanism for controlling sequential gating activity in the K^+ channel, with the permeant ion regulating the onset of ion channel activation as well as inactivation.

Results

Gating is modulated by internal and external potassium

We can depict KcsA-Kv1.3-channel gating with a simplified gating cycle describing equilibria between four composite gating states, namely closed state C, opened state O, and inactivated states I and I* (**Fig. 1a**).[46,79,131] We hypothesized that the equilibria between the four K^+ channel states have different sensitivities to internal ($[K^+]_{in}$) and external ($[K^+]_{out}$) K^+ concentrations. Therefore, we investigated effects of changes in $[K^+]_{in}$ and $[K^+]_{out}$ on pH-induced KcsA-Kv1.3 channel gating.

First, we studied the influence of $[K^+]_{out}$ on KcsA-Kv1.3 channel inactivation by establishing inside-out patches from KcsA-Kv1.3 proteoliposomes prepared in 150 mM NaCl. The pipette solution (corresponding to $[K^+]_{out}$) was varied between 0 and 150 mM KCl. The bath solution was set to 150 mM KCl ($[K^+]_{in}$). As previously described[98,128], a change in pH from 7.5 to 4.0 activates the KcsA-Kv1.3 channel, and in the continued presence of protons the activated channel slowly inactivates, reflecting a conformational transition from a conductive to a non-conductive state, and finally reaches a steady-state current (I_{ss}) level (**Fig. 1b**).[71] Currents were well described by fitting to the data a Hodgkin-Huxley related formalism ($I=I_0 m(t)^4 h(t)$) with one activation (τ_{act}) and one inactivation time constant (τ_{inact}).[137] The time constants τ_{act} and τ_{inact} varied with $[K^+]_{out}$. Moreover, KcsA-Kv1.3 steady-state current levels (I_{ss}/I_{max}), remaining at the end of the test-pulse, were very sensitive to $[K^+]_{out}$ (**Fig. 1b**). A plot of I_{ss}/I_{max} versus $[K^+]_{out}$ revealed that I_{ss}/I_{max} titrates with

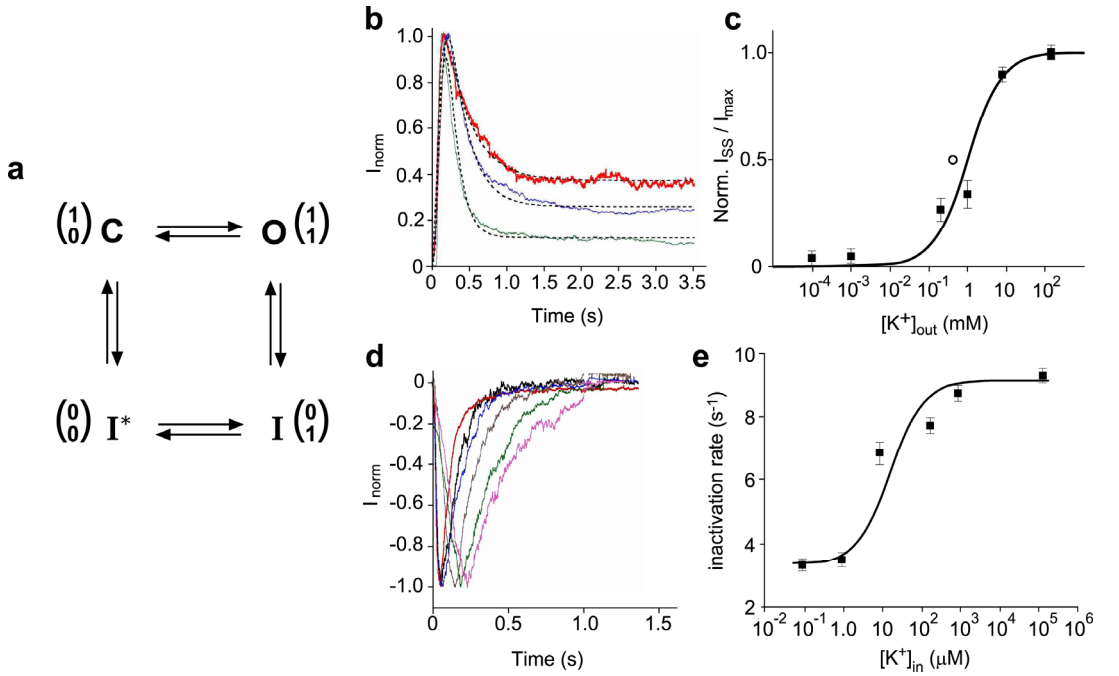

Figure 1. K^+-sensitivity of KcsA-Kv1.3 channel gating. (***a***) A four-state minimal gating model with an upper (inactivation) and a lower (activation) gate in the conduction pathway of the KcsA-Kv1.3 channel. Gate positions (0 for closed and 1 for opened) are diagrammed in one column-matrices with upper gate in upper and lower gate in lower row. C – closed channel in resting state; O – opened channel; I and I* - inactivated states. (***b***) Normalized KcsA-Kv1.3 outward-currents (I_{norm}) recorded at + 100 mV with different external K^+ ($[K^+]_{out}$) concentrations (150 mM ,red; 1 mM ,blue; 1 μM, green). Inside (bath) solution contained always 150 mM KCl. Dashed curves are fits to the data according to Roeper *et al.*[137] (***c***) Normalized steady-state current amplitudes $(I_{ss})_{norm}$ plotted against $[K^+]_{out}$. Solid line represents fitted curve to the dose-response data (■) with K_D for external K^+-binding of 0.9 mM. Error bars are s.e.m. (n = 5 – 14). (○) – K_D for extracellular K^+-binding site on KcsA.[104] (***d***) Normalized KcsA-Kv1.3 inward currents (I_{norm}) recorded at – 100 mV with different internal K^+ ($[K^+]_{in}$) solutions (0 mM, magenta; 1 μM, green; 10 μM, brown; 0.2 mM, black; 1 mM, blue; 150 mM, red). Outside (pipette) solution contained 150 mM KCl. (***e***) $[K^+]_{in}$-sensitivity of inactivation rate (τ_{inact}). Error bars are s.e.m. (n = 5 to 12). K_D-value of 6.5 μM was obtained by fitting a smooth curve to the dose-response data (■) as described by Baukrowitz and Yellen.[130]

$[K^+]_{out}$ (**Fig. 1c**), showing a K_D of 0.9 mM with a maximal I_{ss}/I_{max}-value of 0.44 at 150 mM $[K^+]_{out}$ and a minimum I_{ss}/I_{max}-value of 0.02 at 0 $[K^+]_{out}$. We note that this K_D-value of K^+-sensitive KcsA-Kv1.3 inactivation is similar to the K_D of 0.43 mM determined in calorimetric studies for an external K^+-binding site of the closed KcsA-channel.[104] Importantly, K^+ occupancy of this site affects selectivity filter conformation.[104] The conclusion is that K^+-binding to this site is essential for a stable conductive structure of the selectivity filter, which otherwise is prone to collapse.

Next, we investigated the influence of $[K^+]_{in}$ on KcsA-Kv1.3 gating properties. Inside-out patches were established with 150 mM K^+ in the pipette solution and were perfused with bath solution containing different $[K^+]_{in}$ (0 to 150 mM $[K^+]$).

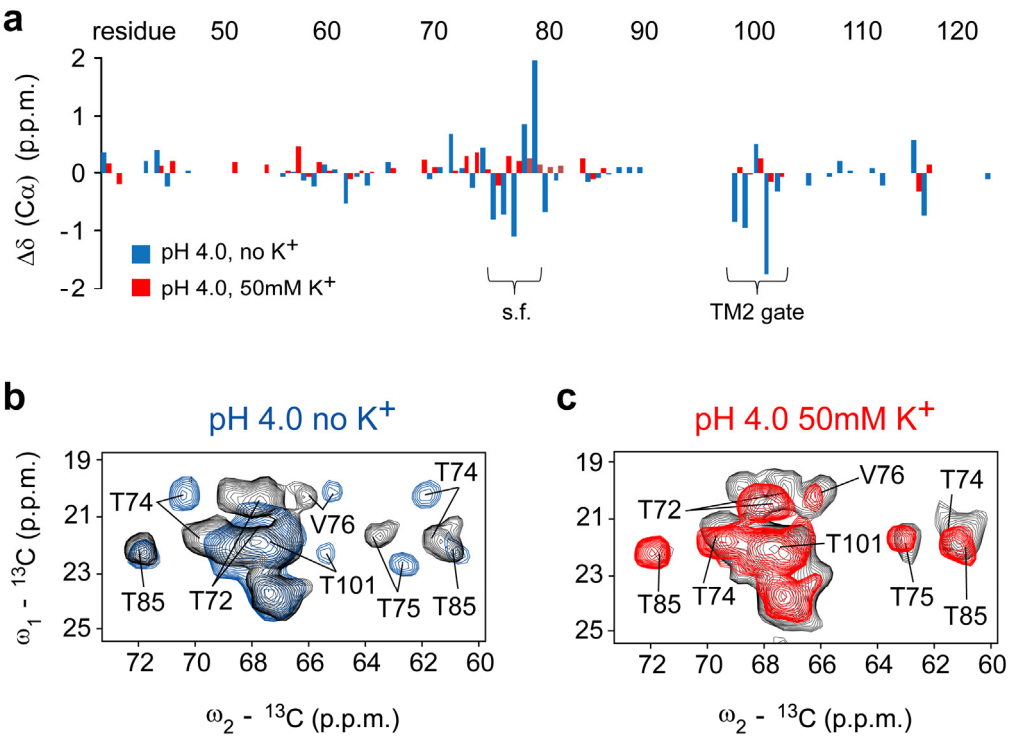

Figure 2. (***a***) Cα chemical shift changes observed for the pore domain of KcsA-Kv1.3 (residues 38-122) at pH 4.0 in the absence (blue bars) and the presence of 50 mM K^+ (red bars) compared to values at pH 7.5 plotted against the residue number. Residues comprising the selectivity filter (s.f.) and the TM2 gate are indicated. (***b***) Regions from ^{13}C, ^{13}C correlation spectra obtained for KcsA-Kv1.3 at pH 7.5 (black) and pH 4.0 (blue) in the absence of K^+. Sizable chemical shift changes for residues in selectivity filer (T74, T75, V76) and TM2 gate (T101) are visible. (***c***) Regions from (^{13}C, ^{13}C) correlation spectra obtained for KcsA-Kv1.3 at pH 7.5 (black) and pH 4.0 (red) in the presence of 50 mM K^+. No sizable chemical shift changes are observed.

Upon a pH jump from 7.5 to 4.0, hyperpolarizing test pulses induced rapid activation of K^+ inward-current (**Fig. 1d**). In agreement with previously reported outward-rectification properties of KcsA-mediated currents, inactivation of KcsA-Kv1.3 inward-current was essentially complete.[99,128] The most important observation which we made in the data was that $[K^+]_{in}$ significantly accelerated KcsA-Kv1.3 inactivation with a minimal time constant τ_{inact} at ≥ 0.2 mM $[K^+]_{in}$ (**Fig. 1d**, **e**). A plot of $1/\tau_{inact}$ versus $[K^+]_{in}$ showed that τ_{inact} titrates with $[K^+]_{in}$ (**Fig. 1e**), revealing an internal K^+-binding site with K_D = 6.5 µM. By contrast, the time course of KcsA-Kv1.3 recovery from inactivation was K^+-insensitive. Time constants for recovery from inactivation (τ_{rec}) were in symmetrical (150 mM), low (1 µM) internal or low (1 µM) external $[K^+]$ essentially identical (τ_{rec} = 3.24 ± 0.14 s, n = 18, s.e.m., data not shown).

We inferred from the data that inactivation of KcsA-Kv1.3 channel is affected by two distinct potassium binding events, while recovery from inactivation seems to be refractory to changes in $[K^+]_{in}$ and $[K^+]_{out}$. The implication is that the equilibria between activated and inactivated channel states, which are influenced by changes in $[K^+]_{in}$ and $[K^+]_{out}$, are correlated with K^+-sensitive conformational rearrangements in the KcsA-Kv1.3 channel. To investigate this K^+ sensitivity of

KcsA-Kv1.3 conformational states on a structural level, we employed ssNMR spectroscopy to obtain information on KcsA-Kv1.3 in the presence of different K^+ concentrations.

Steady-state KcsA-Kv1.3 conformation at pH 4.0 is K^+-sensitive

We recorded ssNMR spectra of KcsA-Kv1.3 proteoliposomes prepared at different K^+-concentrations (0 to 150 mM) and pH values. The overall ionic strength of the buffers was kept constant in all samples by replacing potassium by sodium. In low K^+-concentrations (< 1 mM), we had observed sizable chemical shift changes between pH 7.5 and pH 4.0. Isotropic chemical shifts for pore-domain residues, e.g. Glu71, Thr74, Thr75, Val76, Gly77, Tyr78, Gly79, Asp80, Gly99, Ile100, and Thr101 indicated a pore structure in which the activation gate had opened by a bend in the TM2 helix and the selectivity filter had adopted a collapsed conformation (**Fig. 2a** blue bars, **Fig. 2b** blue spectrum).[71] Strikingly, spectra measured at pH 4.0 and K^+-concentrations ≥ 10 mM K^+ displayed resonances essentially identical to those recorded at pH 7.5, both in phosphate/citrate and MOPS buffers (**Fig. 2a** red bars, **Fig. 2c** red spectrum). Similar observations were made for C-terminally truncated KcsA-Kv1.3 comprising only residues 1-125.

Activation-gate opening of K^+ channels is associated with an outward-movement of the inner (TM2) helices around a gating hinge.[69,71,119,121] This relatively large conformational change[61,121] consequently increases the water accessible surface of the channel, particularly of the inner half of the pore domain, and provided an independent means to study activation-gate opening of the KcsA-Kv1.3 channel at acidic pH (**Chapter 2**). We evaluated the water-accessible channel surface by measuring magnetization transferred from selectively excited water protons to channel-protein spins.[138] Results obtained from this type of NMR experiment are bar graphed in **Figure 3a**. In line with our secondary chemical-shift analysis, the data are compatible with a closed-conductive K^+ channel conformation prevailing at 50 mM [K^+] across the entire pH range of 4.0 to 7.5. By contrast, water-edited ssNMR data in low K^+-concentrations (< 1 mM, **Fig. 3a**) suggest a marked conformational change of the channel after a shift to acidic pH, and lend independent support to our observation that in the absence of K^+ acidic pH induces a conformational change characterized by a stably opened activation-gate.

These ssNMR results had two important implications. First, acidic pH, which opens the KcsA-Kv1.3 channel, renders the selectivity-filter vulnerable to inactivation. Second, the probability of activation-gate opening at acidic pH is K^+-sensitive (**Fig. 3b**). The data demonstrate that the prevailing KcsA-Kv1.3 conformation observed at pH 4.0 shifts from the open-collapsed (I) state to the closed-conductive (C) state of the channel in the presence of millimolar K^+-concentrations. This data complements the functional K^+ dependency of channel activity obtained from channel currents by showing that both the activation and the inactivation gate respond to the potassium concentration on a structural level.

Conformational changes are associated with glutamate protonation

Mutational studies suggested that activation-gate opening at acidic pH is associated with protonation of glutamate side chains, notably Glu118 and Glu120 at the lower

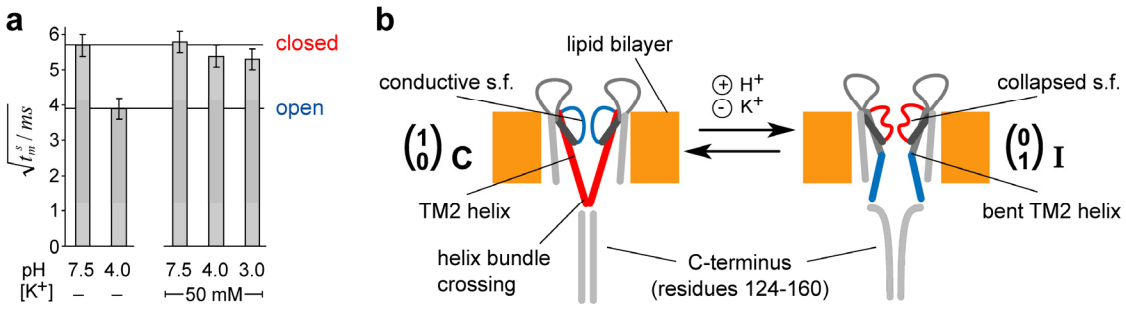

Figure 3. (***a***) Time constant describing magnetization transfer from water to protein spins obtained for pH 7.5, pH 4.0 and pH 3.0 in the absence and the presence of 50 mM [K^+]. Time constants attributed to open and closed activation gates are indicated following Ader *et al.*[138] Accordingly, the water-accessible channel-surface can be probed by measuring magnetization transferred from selectively excited water protons to channel-protein spins. Magnetization build-up is well described by an initial-rate time constant time constant $\sqrt{t_m^s}$ that is sensitive to changes in water-accessible channel surface. We observe in the data that $\sqrt{t_m^s}$ was unaffected by changing the pH from 7.5 to 4.0 in 50 mM [K^+]. ($t_{m,pH7.5}^{s\ 1/2}$ = 5.8 ± 0.4 $ms^{1/2}$; $t_{m,pH4.0}^{s\ 1/2}$ = 5.4 ± 0.4 $ms^{1/2}$), in agreement with our observation that a closed-conductive K^+ channel conformation largely prevails under these conditions. By contrast, in low K^+-concentrations (< 1 mM) a shift to acidic pH markedly decreased $\sqrt{t_m^s}$ ($t_{m,pH4.0}^{s\ 1/2}$ = 3.9 ± 0.4 $ms^{1/2}$). (***b***) Cartoon representation for two subunits of KcsA-Kv1.3 in a lipid bilayer setting. Core elements of gating states are marked. The selectivity filter acts as inactivation gate and resides in conductive/open and collapsed/closed states. The activation gate is located in the TM2 gate of each subunit and gate opening is associated with a bent helix. The C-terminus can be removed by chymotrypsin digestion after reconstitution in lipid bilayers. H^+ induces gating transitions while K^+ stabilizes the closed-conductive resting state of KcsA-Kv1.3.

end of the inner TM2 helix of KcsA.[133] The isotropic chemical shift of glutamate δ carbon atoms is correlated with the sidechain protonation state.[139] Thus, we investigated the influence of pH on NMR resonance frequencies of KcsA-Kv1.3 glutamate residues to monitor activation-gate opening. KcsA-Kv1.3 subunits contain each nine glutamates, four in the pore domain (Glu51, 71, 118 and 120) and five in the cytoplasmic C-terminus (**Fig. 4a**). **Figures 4b-e** depict sections of (^{13}C, ^{13}C) correlation spectra showing glutamate Cγ-Cδ crosspeaks providing information about glutamate protonation states present at different pH- and K^+-conditions. The chemical shifts of Cδ resonances suggested that all glutamates but Glu71 were at pH 7.5 in a deprotonated and at pH 4.0, in the absence of K^+, in a more protonated state (**Fig. 4b**, **c**). Note that magnitudes of chemical shift changes are significantly larger than observed in previous pH-dependent NMR studies of KcsA in solution.[91,94] The Glu71-Cδ resonance at pH 7.5 is consistent with a protonated glutamate side chain in agreement with a water mediated hydrogen bond between Glu71 and Asp80 stabilizing the selectivity filter.[46,87] We observed at pH 4.0 in the presence of >10mM [K^+] two new glutamate Cγ-Cδ crosspeaks in addition to those previously assigned to Glu51 and Glu71[10] (**Fig. 4d**). Comparison of ssNMR spectra of full length and C-terminally truncated KcsA-Kv1.3 (**Fig. 3d**, **e**) showed that removal of the C-terminus selectively eliminated one of these two

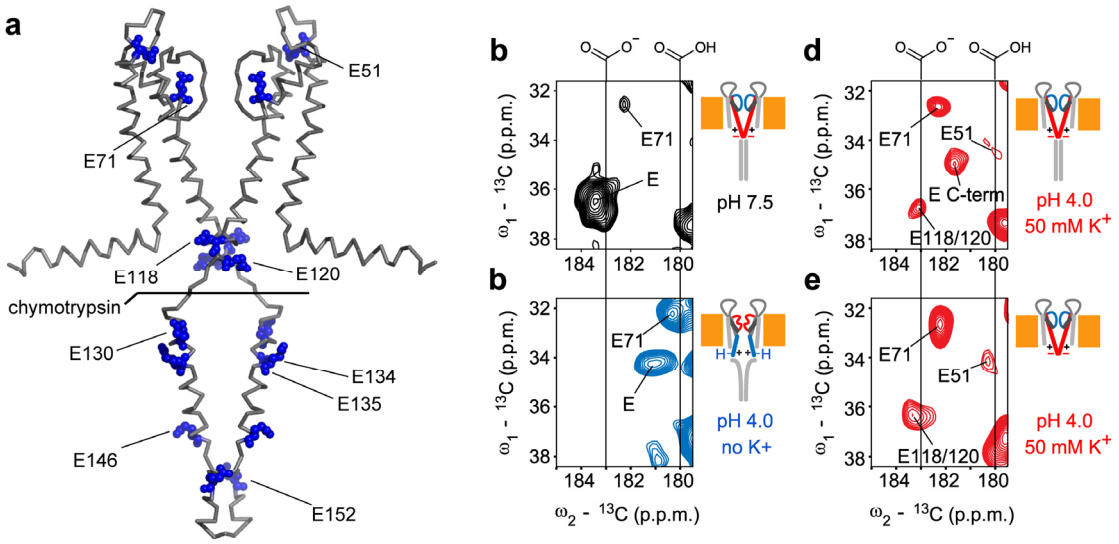

Figure 4. (***a***) Structural model for KcsA-Kv1.3 as published by Schneider *et al.*[10] indicating glutamate residues in blue and the chymotrypsin digestion site. (***b-d***) Regions from (^{13}C,^{13}C) correlation spectra showing glutamate Cγ-Cδ crosspeaks for full-length and C-terminally truncated KcsA-Kv1.3 under different pH and [K^+] conditions. Individual cartoons indicate channel states as defined in Figure 3b. Negative charges and protons illustrate the protonation states of Glu118 and Glu120 at the helix bundle crossing. Positive charges are added to indicate electrostatics at the helix bundle crossing.

glutamate Cγ-Cδ crosspeaks. This peak was, therefore, assigned to the five C-terminal glutamates and the remaining one to Glu118 and Glu120. Following throughout our titration experiments relative intensities of Cγ-Cδ crosspeaks corresponding either to more protonated or deprotonated glutamate side chains, we made the following observations. First, Glu51, having an exposed localization in the extracellular turret region, and the C-terminal glutamates were protonated at pH 4.0 as expected for water-exposed glutamate side chains. We conclude that side chain protonation of these glutamates is K^+-insensitive. By contrast, Cδ resonances of pore-domain glutamates 71, 118, and 120 were markedly K^+-sensitive at acidic pH. Their side chain chemical shifts remained at values seen for neutral pH even at pH 4.0 in the presence of 50 mM [K^+], whereas they shifted to values corresponding to full protonation in the absence of K^+. The data show that protonation is K^+-sensitive for pore-domain glutamates having important roles in activation (Glu118 and Glu120)[133] and inactivation (Glu71) gating of KcsA[86,87] and demonstrate that protonation of pore-domain glutamates is associated both with an opened activation-gate and collapse of the selectivity filter.

Activation and inactivation gate are coupled

Next, we followed conformational changes in the opened-collapsed channel upon back-titration from pH 4.0 to pH 7.5 in the absence of K^+ (**Fig. 5**). We obtained ssNMR-spectra revealing a channel conformation with a collapsed selectivity filter and a closed activation gate. Residues of gating hinge, lower pore helix, and turret region had returned to their conformational states originally observed at neutral pH.

Side-chain resonances of Thr72-Thr75 within the lower selectivity filter and pore helix assumed values close to those seen at pH 7.5 while Cα and Cβ chemical shifts indicate a backbone conformation associated to the collapsed filter (data not shown). Thus, we identified a closed-collapsed conformation in addition to a closed-conductive and an opened-collapsed conformation of the channel. This observation is in agreement with the four state gating circle depicted in **Figure 1a** predicting that the inactivated state comes in two flavors, having either an opened (I) or a closed lower gate (I*). That side-chain resonances of the lower selectivity filter and pore helix (Thr72-Thr75) are only seen to shift together with resonances originating from the gating hinge suggests a residue packing network coupling inactivation and activation gate. Importantly, we could fully restore the closed-conductive (C) state of the resting K^+ channel at pH 7.5 by adding 50 mM [K^+] to the buffer (**Fig. 5**).

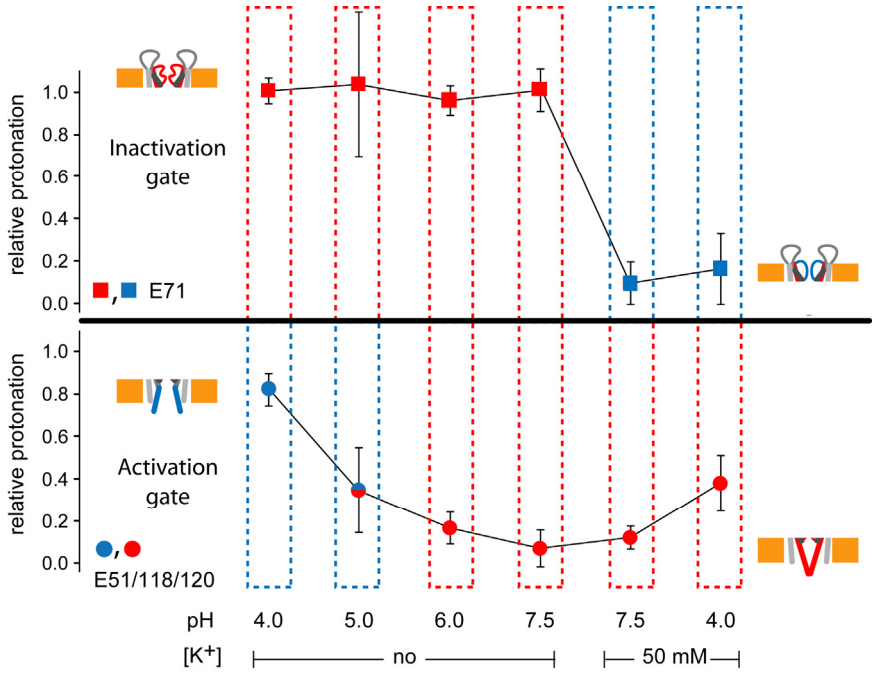

Figure 5. Relative protonation of E71 (square) and E51/118/120 (circle) computed for different pH and [K^+] conditions for truncated KcsA-Kv1.3 (residues 1-125). For each condition, integrals of crosspeaks corresponding to the respective protonated and deprotonated glutamate Cγ-Cδ crosspeaks were normalized to their sum. Relative protonation is, therefore, represented by the fractions of protonated Cγ-Cδ signal. The colours blue and red indicate open and closed conformations of the channel gates, respectively, as seen by chemical shift analysis and water-edited spectroscopy. At pH 5.0 in the absence of potassium the state of the activation gate is ambiguous, because many indicative peaks could not be detected in the spectra under these conditions. Drawings indicate gating states as defined in Figure 3b.

Ligand-binding unmasks gate coupling

The inactivation gate comprising the selectivity filter is a prime candidate for locating the K^+ binding sites entailing the K^+ sensitivity of channel gating inferred from our functional and structural data. In order to test whether gate coupling conveys K^+-sensitivity from the inactivation gate to the activation gate, we

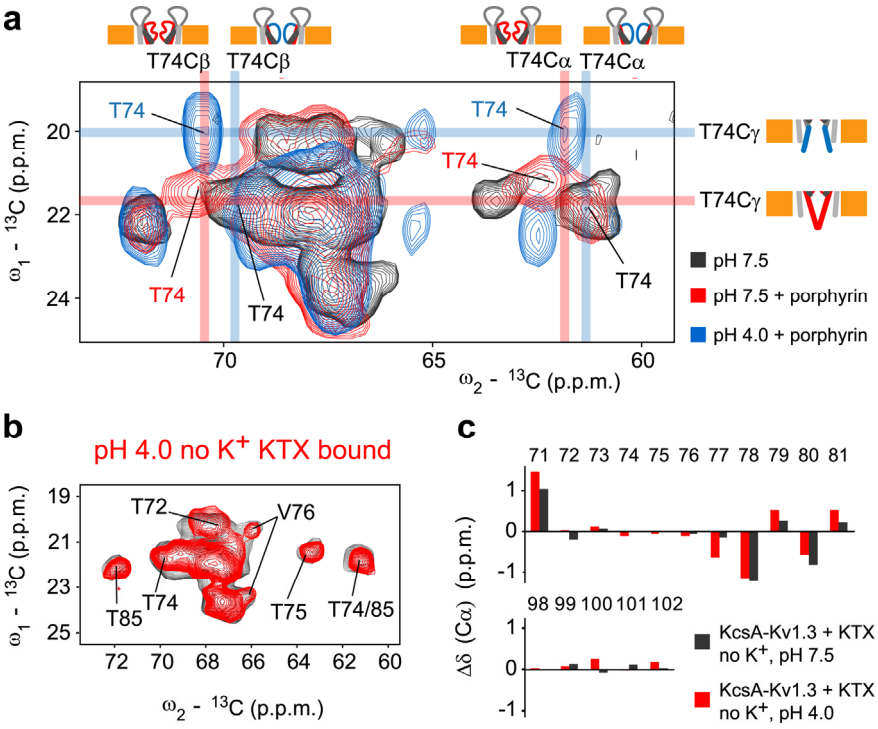

Figure 6. **(a)** Regions from (^{13}C, ^{13}C) correlation spectra obtained for free KcsA-Kv1.3 at pH 7.5 (black) and bound to porphyrin at pH 7.5 (red) and pH 4.0 (blue). Assignments for T74 Cα, Cβ, and Cγ atoms are indicated by colored bars. While sizable Cα and Cβ chemical shift changes are observed for different states of the inactivation gate, namely for conductive and collapsed states of the selectivity filter, the Cγ chemical shift changes largely depend upon activation gate opening indicating a coupling of the two gates via sidechain interactions. Drawings indicate gating states as defined in Figure 3b and blue and red mark open and closed states, respectively. **(b)** Regions from (^{13}C, ^{13}C) correlation spectra obtained for KTX-bound KcsA-Kv1.3 at pH 7.5 (black) and pH 4.0 (red). **(c)** Cα chemical shift changes, in the absence of potassium, observed at two pH values for the inactivation gate (residues 71-81) and the activation gate (residues 98-102) of KTX-bound KcsA-Kv1.3 with respect to free KcsA-Kv1.3 at pH 7.5.

employed two ligands which affect KcsA-Kv1.3 selectivity filter conformation in different ways. The first one, a tetraphenylporphyrin derivative (porphyrin), which binds to KcsA-Kv1.3 with nanomolar affinity, induces a collapsed, non-conductive conformation of the selectivity filter.[71] Binding of the second one, kaliotoxin (KTX), only affects upper selectivity-filter residues[13] and stabilizes a conductive filter-conformation.[140] This particular situation made it possible to study the effect of acidic pH on the lower activation gate in the context of an opened or a closed upper inactivation gate. First, we recorded ssNMR-spectra from the porphyrin-KcsA-Kv1.3 complex at pH 4.0 in the absence of K^+. The spectra were similar to those obtained for the unliganded channel, i.e. they indicated an open-collapsed structure, exhibiting an opened lower activation gate and a closed upper inactivation gate (**Fig. 6a**). Therefore, the porphyrin-bound channel resides in a closed-collapsed conformation at pH 7.5 and an open-collapsed conformation at pH 4.0 resembling the two inactivated states postulated in the cyclic gating model in

Figure 1a. Again, we find that Cα and Cβ chemical shifts of residues Thr72-Thr75 in the lower selectivity filter and pore helix correlate with the open and closed state of the inactivation gate, while side chain chemical shifts on the other hand correlate with the open and closed state of the activation gate (**Fig. 6a**). This suggests that side chain interactions of residues Thr72-Thr75 in and near the inactivation gate and likely the side chain of Ile100 in the gating hinge showing sizable chemical shift changes upon gate opening[71], interact and thus couple the two gates. By contrast, the ssNMR-spectra from the KTX-bound channel revealed that the lower activation gate remained closed at pH 4.0 even in the absence of external K^+ (**Fig. 6b**, **c**). Cδ shifts of Glu118 and Glu120 remained at values corresponding to deprotonated carboxyl groups, while C-terminal glutamates exhibited resonances pointing to protonated carboxyl groups (data not shown). The lower selectivity filter preserved its conductive conformation, and chemical shifts observed for residues 71, 78, 79, and 80 confirmed that KTX remained bound to KcsA-Kv1.3 at pH 4.0 (**Fig. 6c**). The data indicate that KTX binding and high K^+ concentrations have analogous effects on KcsA-Kv1.3 gating states, preserving the channel in a closed-conductive conformation in the steady state even at pH 4.0. **Table 1** provides a summary of gating and protonation states observed for free and ligand-bound KcsA-Kv1.3 under different [K^+] and pH conditions.

		free	KTX	porphyrin
[K^+]	pH	State of the activation gate as seen by ssNMR		
-	7.5	closed	closed	closed
-	4.0	open	closed	open
50 mM	7.5	closed	n.d.	n.d
50 mM	4.0	closed	n.d.	n.d
		State of the inactivation gate as seen by ssNMR		
-	7.5	open	blocked open[a]	closed
-	4.0	closed	blocked open[a]	closed
50 mM	7.5	open	n.d.	n.d
50 mM	4.0	open	n.d.	n.d
		Protonation state of Glu118/Glu129		
-	7.5	deprotonated	deprotonated	deprotonated
-	4.0	protonated	deprotonated	protonated
50 mM	7.5	deprotonated	n.d.	n.d
50 mM	4.0	deprotonated	n.d.	n.d
		Side-chain chemical shift changes observed for Thr74		
-	7.5	no	no	no
-	4.0	yes	no	yes
50 mM	7.5	no	n.d.	n.d
50 mM	4.0	no	n.d.	n.d

Table 1. Summary of channel states observed under different [K^+] and pH conditions for free and ligand-bound KcsA-Kv1.3 reconstituted in asolectin liposomes. n.d.: not determined, a: chemical shift changes indicate adaptation of the selectivity filter conformation due to toxin binding.

Discussion

KcsA-Kv1.3 K^+ channel activation and inactivation is well described by a reductionist gating model.[46,79,131] It defines main channel states by different combinations of opened and closed activation and inactivation gates. Here, we have obtained spectroscopic information for three of the four states: closed-conductive (C), open-collapsed (I), and closed-collapsed (I^*) in a functional membrane setting, with particular attention to residues located in the activation and inactivation gate. We combined ssNMR titration experiments and electrophysiology to probe the K^+- and ligand-sensitivity of these gating states and directly followed protonation events accounting for pH-induced channel gating.
The open probabilities of both activation gate and inactivation gate were found to be distinctly K^+-sensitive. ssNMR results showed that the closed-conductive conformation of the KcsA-Kv1.3 channel is quantitatively converted to an open-collapsed conformation at pH 4.0 if the buffer solution contains no or low K^+-concentrations. Conversely, in high (mM) K^+-concentrations, we observed as most stable conformation in asolectin liposomes a closed-conductive state of the KcsA-Kv1.3 channel at pH 7.5 as well as pH 4.0. The K^+-sensitivity of this gating transition is correlated with a K^+-sensitive protonation of glutamate residues 71, 118, and 120. These residues have an important influence on selectivity filter conformation (Glu71)[86,87] and on pH-induced activation gate opening (Glu118 and 120)[133], respectively. Using ssNMR spectroscopy, we could directly show that protonation of Glu71 correlates with inactivation gate closure and protonation of Glu118 and 120 with activation gate opening.

Our data reveal a higher KcsA-Kv1.3 steady-state current at high external K^+-concentration, a finding which agrees well with previous studies and is consistent with the idea that C-type inactivation is correlated with the collapse of a conductive selectivity filter structure.[71,124,129,136] An earlier study found a K_D of 0.43 mM for K^+ binding to the selectivity filter of KcsA.[104] The K_D value of 0.9 mM we find for the sensitivity of KcsA-Kv1.3 inactivation to external [K^+] as measured by steady-state current is conspicuously similar.

Additionally, our electrophysiological experiments indicate that an internal high-affinity K^+ binding site with a K_D of 6.5 μM modulates KcsA-Kv1.3 activation gating. ssNMR experiments show concordantly that the open KcsA-Kv1.3 activation gate is more stable in low than in high K^+-concentrations. These results are favourably complemented functional studies postulating recovery of K^+ channels from inactivation via closure of the TM2 gate[128,131,134,136] and previous electrophysiological studies on K^+-sensitive gating of the KcsA-channel.[141,142] Note, however, that, in contrast to earlier studies, overall ionic strength was kept constant in our experiments, such that the effects observed here can be traced to potassium itself. Previous reports have related low channel open probability at acidic pH to an open-inactivated state as seen in ssNMR experiments in low (< 1 mM) K^+ concentrations.[61,86,88,119] In light of the results presented here, the exact potassium concentrations and probably also lipid environments seem to be of crucial relevance in order to discuss the individual structural findings in a common context.

The combination of structural and functional data has been very successful for understanding fundamental aspects of K^+ channel activity which regulates the flow of K^+ ions across biological membranes (e.g. ref. 51). Note, however, an important limitation in combining results of structural and functional studies. In structural studies, it is difficult to establish an electrochemical gradient, which drives the flow of K^+-ions along the conduction pathway of the K^+ channel. This situation may be improved by using K^+ channel preparations in proteoliposomes as attempted here. Functional studies, on the other hand, require an electrochemical gradient in order to measure K^+ channel activity, for example activation and inactivation kinetics, voltage-dependence, open probability, and single-channel conductance. Thus, conditions under which no current flows through the channel, for example in low symmetrical [K^+], are inaccessible for functional investigations. Therefore, we investigated the impact of low [K^+] on the KcsA-Kv1.3 channel by separating $[K^+]_{in}$ from $[K^+]_{out}$ in our functional studies. This made it possible to establish a link between functionally important potassium binding events modulating channel inactivation and the influence of K^+ on the conformation of activation and inactivation gates within the K^+ channel pore as seen by ssNMR.

We observed synchronized pH-dependent chemical-shift changes for amino-acid side chains in pore-helix, lower selectivity filter, and TM2 gating hinge suggesting that they are part of an interaction surface responsible for gate coupling. These observations are in line with the crystal structure of closed KcsA (PDB ID 1K4C) where side chains of both regions are in close spatial proximity. As we have shown previously, ssNMR chemical-shift and through-space distances concomitantly suggest that such a conformation may also be adopted by KcsA-Kv1.3 in the closed state.[71] A mechanical coupling might then, for example, involve Ile100 Cδ1 and Thr75 Cγ2 that are less than 5Å apart in the X-ray structure[46] of the closed KcsA channel and exhibit strong chemical-shift changes in our ssNMR data. Opening of the activation gate accomplished by a bend in transmembrane helix 2 could establish side-chain contacts to the inactivation gate, initializing inactivation by lowering the stability of the conductive selectivity filter conformation. While our data at this stage cannot provide a high-resolution structural view of the coupling mechanism, we were able to identify residues that are core players for gate coupling based on chemical-shift changes, suggesting that the two gates interact sterically on the side chain level.

Titration experiments performed with toxin bound channels (**Fig. 7**) reveal that the gating states of the inactivation gate can control activation gating. Low [K^+] supports an opened activation gate in the absence of KTX, but not in the presence of KTX, which traps the filter in a conductive conformation favoring a closed activation gate. Considering which regions are affected by ligand binding (**Fig. 7**), K^+ binding sites 2-4 of the selectivity filter are prime candidates for the internal high binding site that influences activation gating as seen by electrophysiological and ssNMR experiments. This notion is further supported by previous reports showing that presence of K^+ in the selectivity filter of Kv-channels accelerates activation gate closure.[131,143]

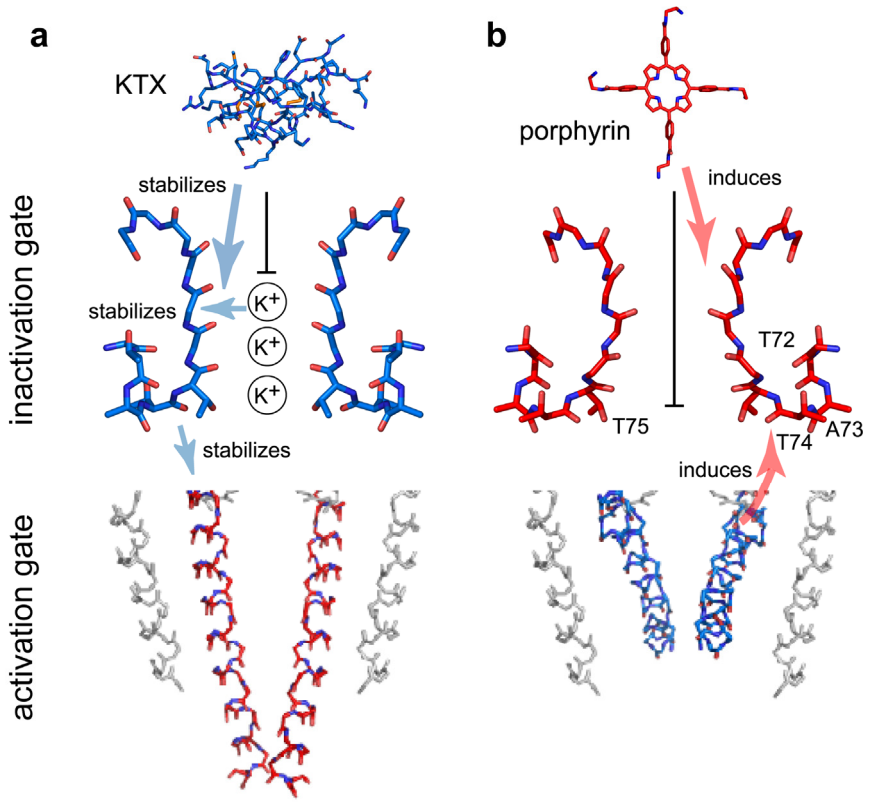

Figure 7. Overview of K^+ and ligand effects influencing the conformation of both channel gates. **(A)** Conductive selectivity filter (blue) and closed activation gate (red) (PDB ID 1K4C)[46] as well as KTX (PDB ID 1XSW)[29] **(B)** Collapsed selectivity filter (red) (PDB ID 1K4D)[46] and a model for the open activation gate (blue) as well as porphyrin ligand.[71] KTX and porphyrin stabilize the conductive and collapsed backbone conformation, respectively, and affect a different set of K^+ binding sites (black vertical bars). Arrows mark the effects of K^+ and ligands on the selectivity filter conformation and the linked impact on activation gating via gate coupling as discussed in the text.

Thus, it is likely that gate coupling as proposed conveys ligand- and K^+-sensitivity from the inactivation gate to the activation gate. An intriguing implication of the data is that K^+-sensitivity and gate coupling propose a powerful mechanism to adjust the gating cycle based on the relative stability of all four possible gating states, suggesting a scenario for consecutive gating transitions involving opening, closing, inactivation, and recovery.

Materials and methods

Sample preparation. KcsA-Kv1.3 expression, purification and reconstitution into asolectin liposomes was done as described previously.[13] Reconstitution was performed at a 100/1 asolectin/KcsA-Kv1.3 molar ratio in either 50 mM Na-phosphate, pH 7.5, 50 mM NaCl or 10 mM MOPS, pH 7.0, 150 mM KCl. C-terminally truncated KcsA-Kv1.3 (residues 1-125) was obtained by chymotrypsin digestion. KTX and porphyrin were added in twofold molar excess as described previously.[13,71] pH and K^+ titrations were performed by washing the

proteoliposomal pellet three times with 1 ml of the desired buffer followed by 30 min ultracentrifugation at 45000 rpm and +4°C. For each titration step the loss of sample was below 5% as judged from 1D ^{13}C spectra. Thus, titrations with up to 10 steps could be performed using a single proteoliposomal sample.

Solid-state NMR. All NMR experiments were conducted using 4 mm triple-resonance (^{1}H,^{13}C,^{15}N) probeheads at static magnetic fields of 9.4, 14.1, and 18.8 T corresponding to 400, 600, and 800 MHz proton resonance frequencies (Bruker Biospin, Karlsruhe/Germany). Assignments were obtained previously[10] and were extended and verified using 2D (^{13}C, ^{13}C) correlation experiments using proton-driven spin diffusion under weak coupling conditions (PDSD-WC).[19] Water-edited ssNMR experiments were performed at 9.4 T and analyzed as described elsewhere[138] using a 3 ms Gaussian $\pi/2$ pulse, a T_2 filter containing two delays (τ) of 1 ms, and a cross-polarization contact time of 700 μs. MAS speeds used were 6.5, 9.375, and 12.5 kHz at 9.4, 14.1, and 18.8 T static magnetic field strengths, respectively, at an effective sample temperature of approximately +7°C. Integration of spectral cross peaks was performed using the software Topspin 2.1 (Bruker Biospin, Karlsruhe/Germany). Error estimates for spectral integrals were obtained from integrals in noise regions with sizes equal to those of the signal integration regions.

Electrophysiology. Electrophysiological measurements on KcsA-Kv1.3 in proteoliposomes were as previously described[71] except that we varied internal and external K^+-concentrations in patch-clamp recordings as follows. External (pipette) and internal (bath) solutions contained 10 mM MOPS buffer and 150 mM monovalent cation (Na^+ or K^+). As indicated in the legends, K^+-concentration in external (pipette) or internal (bath) solution was varied from 0 to 150 mM keeping total monovalent cation concentration constant.

Chapter 5

The conformational stability of K^+ channel gating states depends on the lipid bilayer

Christian Ader[1]
Marc Baldus[1]
Stefan Becker[2]
J. Antoinette Killian[1]
Erica C. E. Kremer[1]
Olaf Pongs[3]
et al.

[1] Bijvoet Center for Biomolecular Research, Utrecht University, The Netherlands
[2] Max-Planck-Institute for Biophysical Chemistry, Germany
[3] University Hospital Hamburg-Eppendorf, Germany

Manuscript in preparation

Abstract

The lipid bilayer regulates localization, structure, and function of membrane proteins. The underlying molecular mechanisms that range from specific lipid-protein binding events to general physical bilayer properties are currently poorly characterized. We have investigated lipid effects on structural integrity and functional gating states of the tetrameric potassium channel KcsA-Kv1.3. Combining high-resolution solid-state NMR spectroscopy with biochemical techniques revealed that potassium and phosphatidic acid increased tetramer stability. Furthermore, specific lipids quantitatively changed the steady-state equilibrium of the channel's gating states. The data suggest that both lipid binding to the non-annular lipid binding site of the channel and physical bilayers properties play an important regulative role for channel structure and function.

Introduction

Biological membranes are highly diversified, functionalized permeability barriers. Lipid bilayers not only provide the basis for compartmentalization but also serve as solvent and association surface for numerous membrane associated proteins. Therefore, membranes are commonly described as fluid mosaic.[144,145] Emerging knowledge about membrane protein function and the underlying molecular structures reveal that the lipid environment plays a crucial role in membrane protein folding and stability as well as for functional integrity and regulation. Lipids can interact as single molecules located in specific protein binding sites or act as entity affecting proteins by general physical bilayer parameters such as intrinsic lipid curvature and hydrophobic mismatch between integral membrane proteins and the hydrophobic core of the bilayer.[146-148]
Detailed analysis of these interactions is often hampered by the diversity and complexity of membranes, even if biochemically produced simplified model systems such as supported bilayers or proteoliposomes are considered. Therefore, approaches that provide insight into the molecular details of such systems are of high importance for our functional understanding of membrane proteins in their biological context.

Solid-state NMR (ssNMR) spectroscopy has proven to be a powerful method to study structure and dynamics of lipid bilayers and associated peptides. In our laboratory, the chimeric potassium channel KcsA-Kv1.3 has been subject to ssNMR spectroscopic investigations of channel activation, inactivation, and ligand binding in a bilayers setting.[10,13,71,138] For the parent KcsA channel, specific (non-annular) and non-specific (annular) lipid-protein interactions have been identified[153-158] and the presence of negatively charged lipids was shown to be essential for ion gating.[97,149-155] Furthermore, lipids play a crucial role for assembly of KcsA subunits forming the potassium channel and concomitantly affect the stability of the functional tetrameric structure.[156-158] Analysis of available crystal structures (compare e.g. refs. 46, 70, 117, 120) reveals that the monomer-monomer interfaces of KcsA and other homotetrameric potassium channels are prominently constituted by the channel's pore region. On the other hand, mutations such as found in the chimeric KcsA-Kv1.3 where eleven residues located in the pore region

are substituted by corresponding residues of the voltage dependent K^+ channel Kv1.3[14,159] (**Fig. 1a**) do not perturb channel structure or function.[71] The question then is to which extend tetramer stability is affected by changes in the pore region.
Furthermore, the pore region of KcsA entails highly selective potassium binding sites located in the selectivity filter of the potassium channel as well as four symmetric non-annular lipid binding sites. Both types of binding sites depend on the structural integrity of the tetrameric channel, because they are located at subunit interfaces. Therefore, it seems likely that also K^+ concentration and the lipid composition of the bilayer modulate tetramer stability. Indeed, this is in agreement with data showing that mutations affecting K^+ binding sites within the selectivity filter of KcsA alter tetramer stability[160] and the fact that phosphatidic acid (PA) was identified to play a special role in KcsA tetramer stability compared to other anionic lipids such as phosphatidylglycerol (PG).[161]
In this study we used KcsA-Kv1.3 reconstituted in lipid bilayers as a model system to study lipid effects on structural stability and functional gating states of this archetypical α-helical potassium channel. First, we studied the stability of the homotetrameric pore domain of KcsA-Kv1.3 in comparison to wild-type KcsA in a membrane setting and probed stabilizing influences of potassium and lipids. Second, we characterized the steady-state stability of gating states linked to pH-induced gating of KcsA-Kv1.3 in reference to the lipid environment. The data suggests that the interplay between protein and surrounding bilayer affects the conformational state of KcsA-Kv1.3 and identified the lipid environment as a potential regulator of the potassium channel gating cycle.

Results

Sequence, lipid, and K^+ dependency of tetramer unfolding

In the following we investigate the cumulative effect of protein sequence, surrounding lipids, and potassium concentration on tetramer stability. Firstly, we monitored tetramer dissociation for KcsA and KcsA-Kv1.3 induced by increasing concentrations of trifluoroethanol (TFE)[97,157,162-164] using gel mobility shift assays (**Fig. 1b**). Secondly, we varied lipid composition and K^+ concentration in these experiments to probe for associated changes in tetramer stability.

Our data revealed that the chimeric KcsA-Kv1.3 channel is intrinsically less stable than wild-type KcsA at 5 mM [K^+]. For example, KcsA tetramers reconstituted in a 7:3 mixture of 1,2-dioleoyl-sn-glycero-3-phosphocholine (DOPC) and 1,2-dioleoyl-sn-glycero-3-phosphate (DOPA) remained intact at 30% TFE. In contrast, only about 10% of the chimeric tetramers were preserved under identical conditions (**Fig. 1b**).
Additionally, we found that both K^+ channels are more stable in DOPC/DOPA compared to a lipid bilayer where DOPA was substituted by 1,2-dioleoyl-sn-glycero-3-phosphoglycerol (DOPG) (**Fig. 1b**). This confirms that PA is an exceptional stabilizer of the KcsA tetramer. Interestingly, the increased stability of KcsA in bilayers containing PA is markedly pH sensitive and could not be observed if the pH was lowered close to the pK_a (3.2) of PA (**Fig. 1b**). For a lipid composition of DOPC/DOPG (7:3), in contrast, tetramer stability was found to be

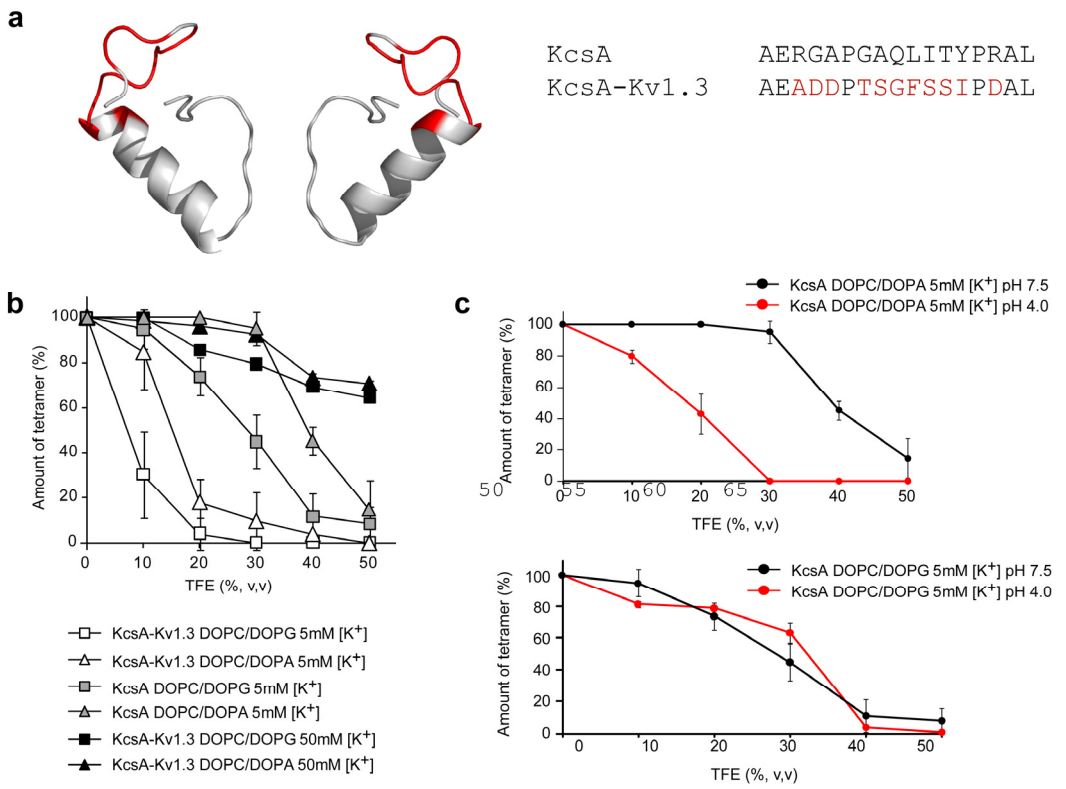

Figure 1. Gel mobility shift assays report on trifluoroethanol (TFE) induced tetramer dissociation. (***a***) Mutations introduced in KcsA-Kv1.3 are indicated and corresponding residues are colored red in the structure (PDB ID 3EFF) of $KcsA^{165}$ (residues 50-85 are shown for two subunits). (***b***) Tetramer stability observed at neutral pH for KcsA and KcsA-Kv1.3 reconstituted in DOPC/DOPG (7:3) and DOPC/DOPA (7:3) at different potassium concentrations. (***c***) Tetramer stability observed for KcsA reconstituted in DOPC/DOPG (7:3) and DOPC/DOPA (7:3) in the presence of 5 mM [K^+] at pH 7.5 (black) and pH 4.0 (red). TFE treated samples were analyzed by SDS-PAGE and quantified by densitometry following the tetramer band. Data points correspond to the average of two or three experiments. Standard deviations are given as error bars.

pH insensitive as seen by TFE-induced unfolding (**Fig. 1b**). This makes it unlikely that the observed destabilization at acidic pH in the presence of PA is caused by pH-induced opening of KcsA and suggests that the charge and hydrogen-bond potential of PA form the molecular basis of PA induced tetramer stabilization.

Next, we investigated the potassium sensitivity of tetramer stability by increasing the potassium concentration used for TFE titration experiments from 5 mM to 50 mM. The overall ionic strength in these experiments was kept constant by replacing sodium by potassium. Hence, changes observed can be attributed to potassium itself excluding non-specific electrostatic effects. We found potassium to strongly stabilize tetrameric KcsA-Kv1.3 independent of the lipid induced stabilization (**Fig. 1b**). At 50 mM K^+ chimeric tetramers were found almost quantitatively preserved at 30% TFE while only about 10% of KcsA-Kv1.3 was in the tetrameric state in the presence of 5 mM [K^+].

In summary, our data based on gel mobility shift assays revealed that the pore region of KcsA potassium channels is of high importance for the structural integrity of the tetrameric channel state. Furthermore, binding of both potassium and lipids seems to play a substantial role for tetramer stability.

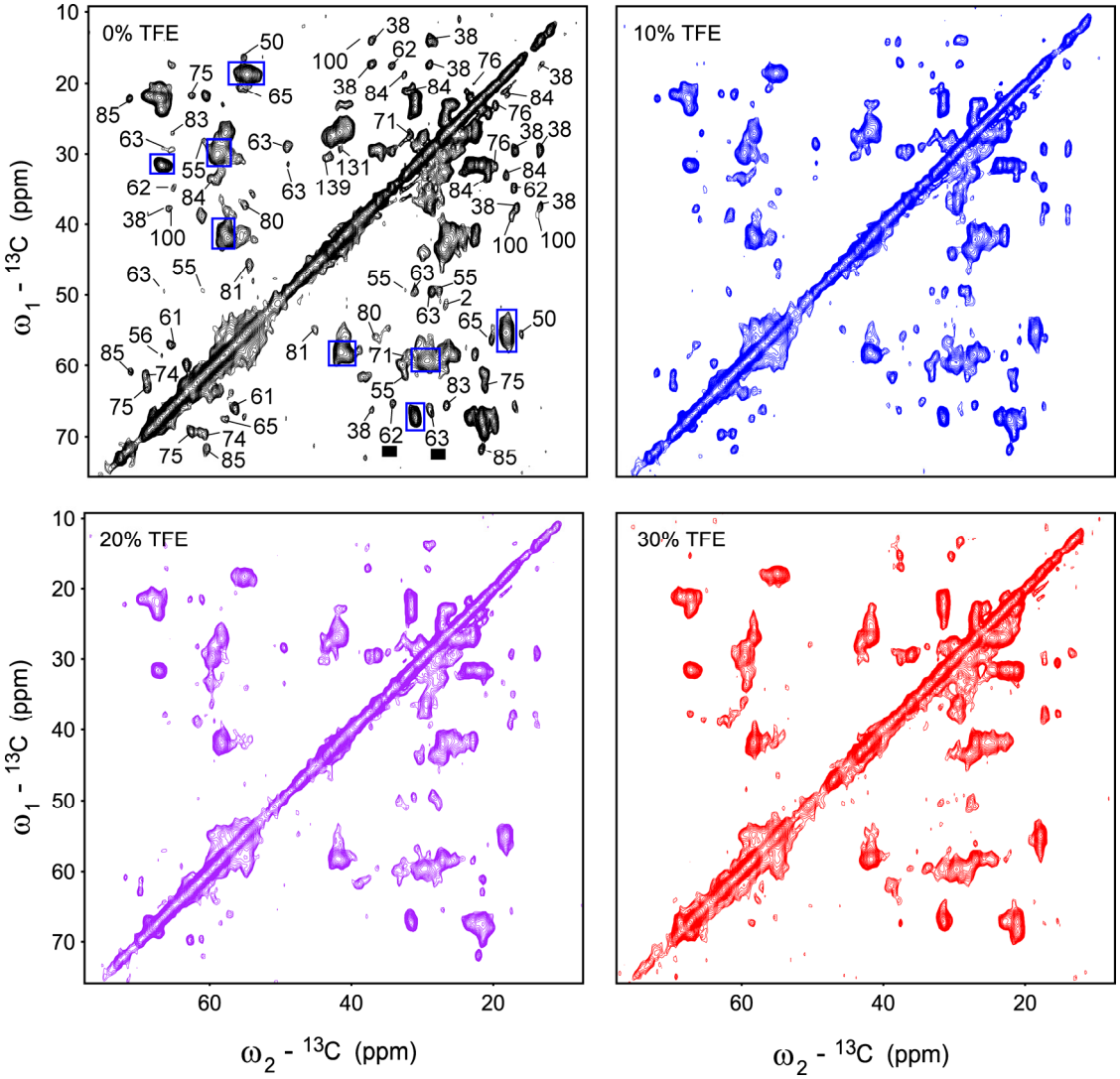

Figure 2. (^{13}C, ^{13}C) correlation spectra obtained for KcsA-Kv1.3 reconstituted in DOPC/DOPG (7:3), pH 7.5, and 5 mM [K^+] at different concentrations of TFE. Peaks used for the residues specific analysis of tetramer dissociation are indicated. Blue boxes mark regions of high spectral overlap representing Ala, Arg, Glu, Leu, and Val residues located in transmembrane and terminal helices.

In order to obtain a more detailed view on channel stability and dissociation in a membrane setting, we employed solid-state NMR spectroscopy to follow site-resolved structural changes within the channel's pore region upon TFE titration. Based on the results discussed above, we chose conditions under which KcsA-Kv1.3 was most sensitive to TFE, namely prepared in DOPC/DOPG (7:3) bilayers and 5 mM [K^+]. We successively acquired ssNMR spectra under MAS (Magic Angle Spinning) to obtain residue-specific information at 0, 10, 20, and 30% (v/v) TFE (**Fig. 2**). We could trace 70 resolved cross-peaks in (^{13}C-^{13}C) correlation

spectra assigned to 21 residues of KcsA-Kv1.3[10] throughout the TFE titration (**Fig. 2**). Integration of the respective peak areas and normalizing them to the initial peak volumes at 0% TFE, allowed us to follow alterations in protein structure by ssNMR cross-peak position and signal intensity. Additionally, we could follow an ensemble of about 70 α-helical residues that are represented by defined regions of high signal density in (^{13}C-^{13}C) correlation spectra accounting for the high occurrence of Ala, Arg, Glu, Leu, and Val residues in transmembrane and terminal helices (**Fig. 2**). Signal intensities for these regions provided us with a global measure for helix stability. **Figure 3** summarizes spectral changes detected in the course of the ssNMR titration experiments.

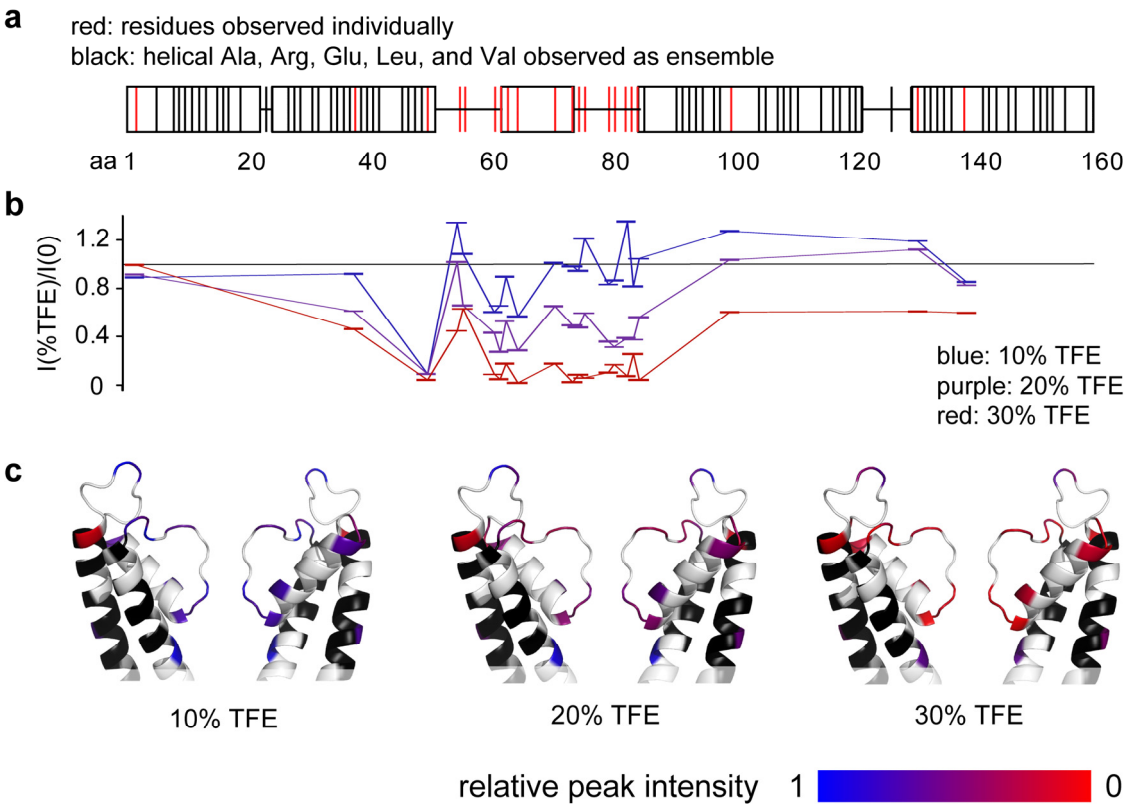

Figure 3. (***a***) TFE dependency for relative intensities of resolved cross-peaks due to 21 residues (marked red) plotted against the KcsA-Kv1.3 sequence. Secondary structure of KcsA-Kv1.3 is indicated (box: helix, line: loop). Residues contributing to spectral regions of high signal overlap due to helical Ala, Arg, Glu, Leu, and Val are marked black. (***b***) The intensity changes plotted in (a) are mapped onto the crystal structure of KcsA (PDB ID 1K4C)[46]. Residues observed individually are colored according to a blue-red gradient were pure blue corresponds to 100% peak intensity and pure red to peak absence. α-helical residues observed as an ensemble are colored black, residues not considered white.

Residues affected first, i.e., already at 10% TFE, are located at the extracellular end of transmembrane helix 1 (TM 1) (Ala50) and the beginning of the pore helix (Ser61, Ile62, Pro63, and Ala65). At higher TFE concentrations also peaks due to residues located in the rest of pore helix and the subsequent selectivity filter gradually disappeared indicating emergence of dynamical and/or structural

disorder. This region of the channel comprises many of the inter-subunit contacts stabilizing the tetrameric state. At 30% TFE no signal originating from pore helix, selectivity filter and extracellular loops could be detected consistent with the loss of tetrameric organization and well-defined protein structure. This observation is in agreement with gel mobility shift assays confirming the absence of tetrameric channel structures under similar conditions. In contrast, intensities detected for regions representing amino-acid types that occur frequently in transmembrane and C-terminal helices were found to be invariant throughout the titration (data not shown). This suggests that α-helical regions are largely preserved and exhibit limited structural mobility, in agreement with previous characterizations of monomeric KcsA.[92,163,166] In conclusion, we found that TFE induces structural and/or dynamical disorder in the pore region of the KcsA-Kv1.3 potassium channel. Residues affected firstly by TFE are located at the extracellular end of TM 1 and in the loop connecting TM 1 and the pore helix. While we did not find evidence for a well defined structure in the pore region of KcsA-Kv1.3 comprising extracellular loops, pore helix and selectivity filter at 30% TFE, the secondary structure of transmembrane and terminal helices seems to be largely preserved.

Lipid dependence of the gating states of KcsA-Kv1.3

Based on the K^+ and lipid dependence of quarternary structure discussed above, it is likely that also membranes and characteristics of their respective lipid components contribute to the functional integrity of the potassium channel KcsA-Kv1.3 in general, and conformational states of the gating cycle in particular. Previously, it was for example shown that KcsA channel activation depends on negatively charged lipids[97] and that channel structure adapts to bilayer thickness.[154] Here, we used ssNMR spectroscopy to analyze the impact of the lipid environment on the steady-state conformation of KcsA-Kv1.3. The potassium channel was reconstituted in liposomes of defined lipid composition maintaining the 1,2-dioleoyl-sn-glycerol (DO) moiety but varying the phospholipid headgroup. Lipids investigated were PC, PA, PG, PE (phosphoethanolamine), and in addition bovine Cardiolipin. We thereto reconstituted KcsA-Kv1.3 in pure DOPC and in lipid mixtures containing 70% DOPC (mol/mol) and 30% of one of the other above-mentioned lipids.

We then used two-dimensional ssNMR spectroscopy under MAS to analyze the influence of the lipidic environment on the conformation of KcsA-Kv1.3 gating states which depend on pH and K^+ concentration. Therefore, we obtained spectra at pH 7.5 and pH 4.0 for KcsA-Kv1.3 in each lipid setting to follow the transition of the potassium channel from its resting state to an inactivated channel state.[71] Furthermore, we acquired spectra at 50 mM [K^+] and in the absence of explicit potassium in the buffer to account for a K^+ induced stabilization of the channel's resting state observed previously for KcsA-Kv1.3 reconstituted in asolectin liposomes (**Chapter 4**).

First of all, we observed that ^{13}C and ^{15}N line widths and chemical shifts were generally similar for all samples investigated (**Fig. 4**). This shows that ssNMR-based analysis of such proteoliposomes provides great freedom for defining suitable and biologically relevant lipidic environments. In agreement with our previous observations, we find that in the absence of explicit K^+ in the sample buffer, KcsA-Kv1.3 converts from a closed to an open conformation if pH is

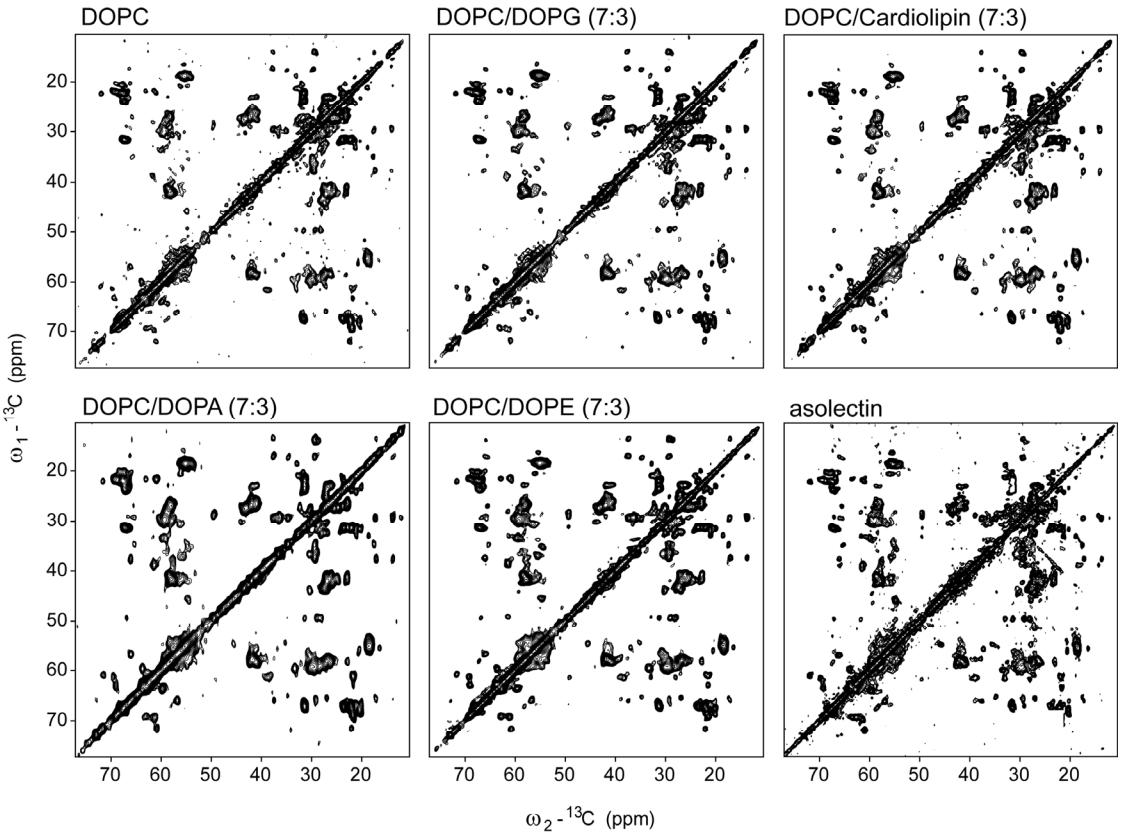

Figure 4. (^{13}C, ^{13}C) correlation spectra obtained for KcsA-Kv1.3 reconstituted in bilayers of different lipid composition at pH 7.5 and 50 mM [K^+].

changed from pH 7.5 to pH 4.0 independent from the lipidic environment (data not shown). This rearrangement corresponds to a bent in the second transmembrane helices of the channel subunits that block the ion permeation pathway along the C4 symmetry axis of the channel in the closed conformation at the, so called, helix bundle crossing. Characterizing an inactivated channel, the selectivity filter was found in a collapsed, non-conductive conformation at pH 4.0 in the absence of potassium for all samples investigated in agreement with our previous results.[71]

In the following, we detected conformational changes associated with pH-induced gating in the presence of 50 mM [K^+] (**Fig. 5**), because we had previously observed that KcsA-Kv1.3 reconstituted in asolectin liposomes assumed an open-inactivated state at pH 4.0 in low [K^+] but remained in its resting state even at pH 4.0 in high [K^+] (**Chapter 4**).
For proteoliposomes containing PC, PC/PG, and PC/Cardiolipin we found at pH 4.0 and 50 mM [K^+] an inactivated KcsA-Kv1.3 channel characterized by an open activation gate and a collapsed selectivity filter closing the channel's inactivation gate similar to the experiments performed in the absence of explicit potassium (**Fig. 5b, c**). Notably, this confirms that a collapsed filter conformation can be stably induced also at high millimolar [K^+] if the activation gate is open and further underpins the idea that a collapsed filter conformation is a biologically relevant state of the channel essential for inactivation gating.

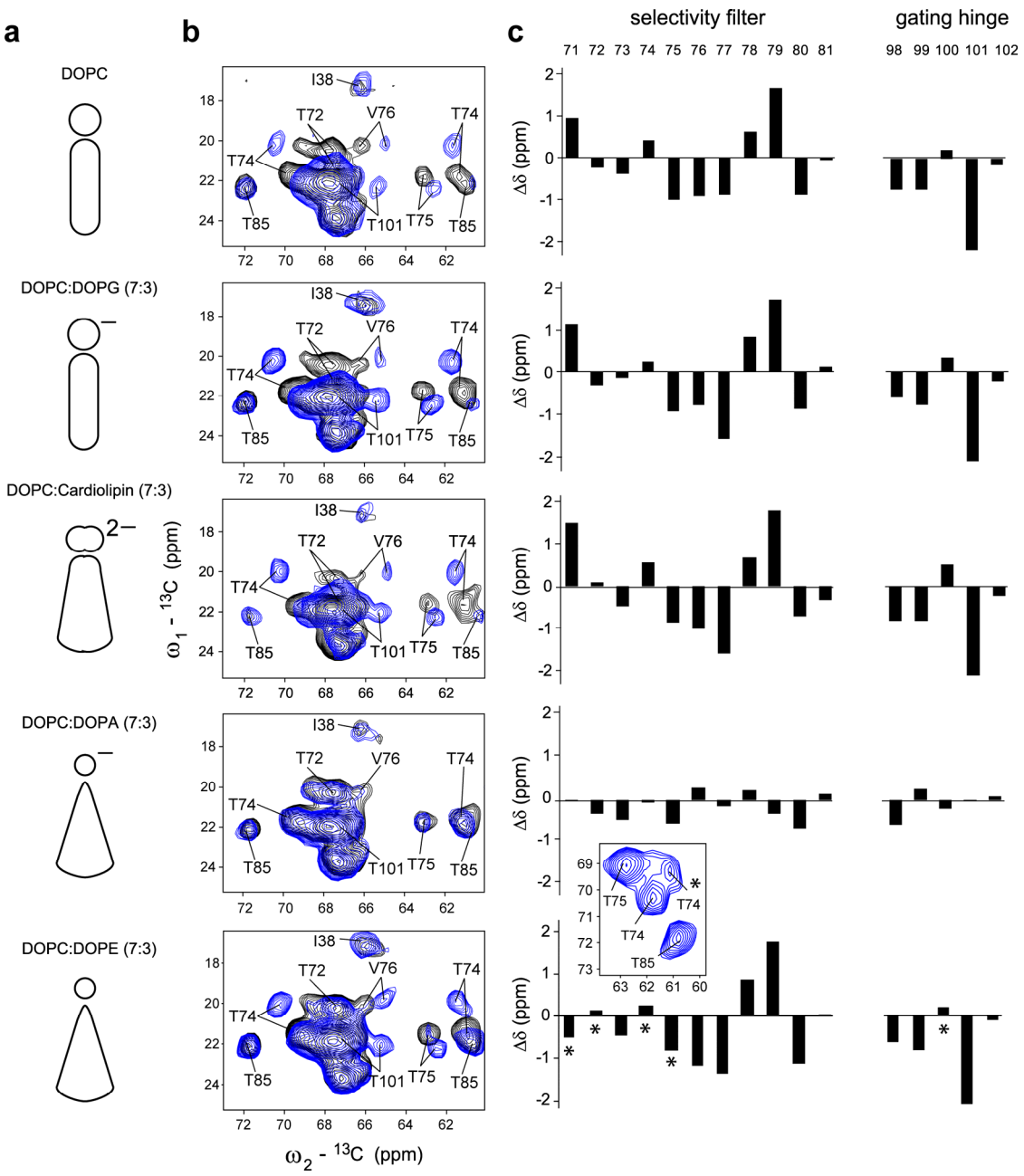

Figure 5. (***a***) Cartoon representation of lipids investigated indicating net charge and overall molecular shape. (***b***) (^{13}C, ^{13}C) correlation spectra obtained for KcsA-Kv1.3 reconstituted in bilayers of indicated composition in 50 mM [K^+] at pH 7.4 (black) and pH 4.0 (blue). Peak assignments are indicated. (***c***) Cα chemical shift changes for residues located in and close to the selectivity filter and the TM2 gating hinge observed after changing from pH 7.4 to pH 4.0. For the DOPC/DOPE sample we observed two peak sets. Chemical shift changes are bar graphed for the more intense peaks. Residues for which also peak sets for the other channel conformation are apparent are marked by asterisks. The inlayed spectrum shows the two observed Cβ-Cα peaks found for T74.

KcsA-Kv1.3 reconstituted in PC/PA and PC/PE, however, was found to reside predominantly or at least partially in the closed-conductive state under high potassium conditions at pH 4.0 (**Fig 5b, c**).
As asolectin contains PA as well as large quantities of PE, these observations link our earlier results to the presence of these lipids in combination with high [K^+]. Moreover, the fact that acyl-chains are invariant among the lipids investigated suggests that the molecular basis of the effect observed depends on the lipid headgroups including characteristics like their hydrogen bond potential. Another feature of PA and PE is the cone-like shape of these particular lipids compared to the more cylindrical shape of the other lipids investigated (**Fig. 5a**). Therefore, also physical bilayer properties associated with structural frustration of lipids might play a role for the channel's conformational stability. The basic conclusion from the present data is that the lipid bilayer has the potential to quantitatively change the steady-state equilibrium of KcsA-Kv1.3 gating states in a potassium-dependent manner.

Discussion

Multimerization of membrane proteins is a delicate process that is well supported and regulated in living cells (see e.g. refs. 167-169 for review). For the bacterial potassium channel KcsA, it was shown that membrane localization and efficient tetramer formation in *Escherichia coli* depend on signal particle recognition and the protonmotif force.[170,171] Detergent solubilized tetrameric KcsA on the other hand readily integrates into pure lipid bilayers where its stability is increased by the presence of negatively charged phospholipids.[45,172] Here, we found that phosphatidic acid and [K^+] distinctly increase tetramer stability. pH dependence of the effect observed for PA suggests that charge and hydrogen-bond potential of the PA headgroup is essential for the increased potassium channel stability. Comparing wild-type KcsA to the chimeric KcsA-Kv1.3 potassium channel revealed a marked decrease in stability of the channel containing 11 mutations in its pore region. Notably, KcsA-Kv1.3 comprises a mutation in residue 64 substituting Arg by Asp. This Arg residue together with the essential Arg89 contributed by the neighboring subunit was proposed to constitute the non-annular lipid binding sites of KcsA.[97,150] Therefore, the occupancy and respective state of these lipid binding sites is suggested to influence tetramer stability.
In order to probe the structural stability of membrane associated KcsA-Kv1.3 in a site resolved manner, we followed TFE induced unfolding of the K^+ channel by solid-state NMR spectroscopy. We found that residues affected first by TFE are located in the extracellular end of the TM1 helix and the turret loop surrounding the mutated residue Asp64. While Arg89 seems to be essential for functional KcsA[97,150], mutation of Arg64 may alter channel inactivation[86] but seems to be less crucial for channel folding as well as tetramer stabilization induced for example by PA. This could mean that the mutations including Arg64Asp introduced in the pore region have little influence on tetramer stability. On the other hand, KcsA-Kv1.3 is less resistant towards TFE induced unfolding than the parent KcsA channel and our site-resolved analysis of this process indicates that residues close to the non-annular lipid binding site of KcsA show an early response upon increasing amounts of TFE. This spotlights the regions close to the lipid binding sites as critical for

channel unfolding and might well reflect the importance of lipid binding to the channel's pore region for tetramer stability.

Furthermore, we observed that increased potassium concentrations also oppose TFE induced tetramer dissociation. This is in good agreement with results obtained for selectivity filter mutations of KcsA showing that these mutations not only change ion binding but also affect tetramer stability.[160] Notably, molecular dynamics simulations performed for KcsA in a lipid setting disclosed potential hydrogen-bond interactions between Arg89 and Asp80.[173] By removing this interaction *in silico* the tetramer was destabilized and started to dissociate. These data together with our results imply the presence of a hydrogen bond network connecting selectivity filter, non-annular binding sites and bound lipids (**Fig 6a**) and suggest that both potassium as well as lipids with a high hydrogen-bond capacity stabilize a conductive channel state.

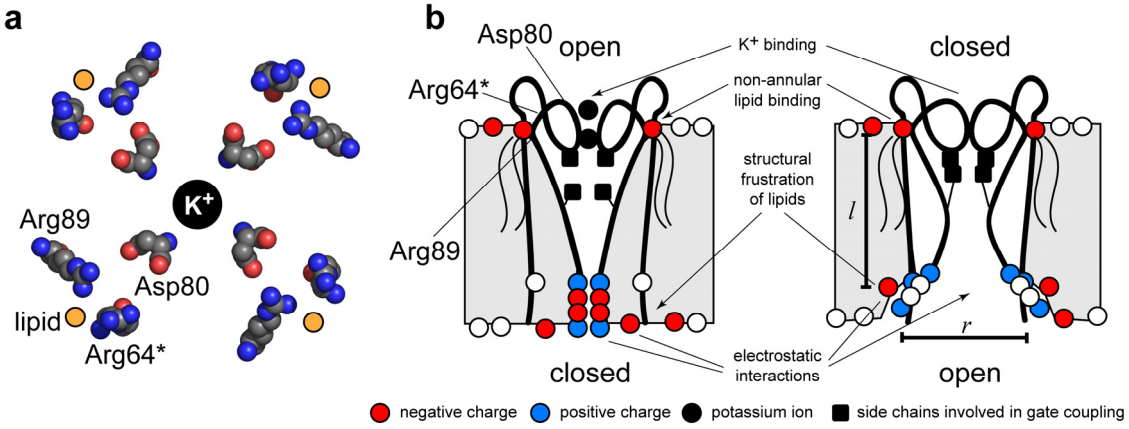

Figure 6. (***a***) Extracellular view on KcsA residues Arg64 (*mutated to Asp in KcsA-Kv1.3), Asp80, and Arg89. The potassium permeation pathway along the axis of fourfold symmetry and the non-annular lipid binding sites are indicated. (***b***) Cartoon illustrating molecular determinants affecting the steady-state equilibrium between the resting state of KcsA-Kv1.3 (left) and its open-inactivated state (right). Charges of protein residues and lipid headgroups are color coded (blue: +, red: -). Potassium ions are indicated as black circles and sidechains establishing gate coupling as black squares. The effective protein radius (*r*) and the protein hydrophobic length (*l*) are prone to change upon channel opening potentially altering structural frustration of phospholipids.

Potassium channel activation and inactivation gating was previously reported to depend on potassium and the lipidic environment (e.g. refs. 124, 128, 134-136 and 97). However, the molecular basis, especially of the lipid dependencies, has been elusive. We now characterized stabilities of the KcsA-Kv1.3 potassium channel gating states in a broad range of lipid, pH, and K^+ settings by ssNMR spectroscopy. Importantly, we observed similar spectral resolution and sensitivity for all samples investigated. Thus, ssNMR techniques are well suited to study such versatile proteoliposomal samples and the method provides great freedom to adjust sample conditions according to biological relevance.

Furthermore, no sizable ^{13}C chemical shift differences were observed among different preparations at neutral conditions (**Fig. 4**, pH 7.5, 50 mM [K^+]) confirming that KcsA-Kv1.3 resides in a well defined and reproducible structure in all bilayers investigated. Upon changing from neutral pH to pH 4.0 we were able to trace the influence of the lipid environment on pH-induced K^+ channel gating. Previously, we reported that potassium can stabilize KcsA-Kv1.3 reconstituted in asolectin liposomes in its closed-conductive resting state even at pH 4.0, while the channel underwent structural rearrangements leading to an inactivated state in the absence of explicit potassium (**Chapter 4**). The present data reveals that this conformational state is not only controlled by potassium but also strongly lipid dependent. For the majority of lipid mixtures studied, we found the K^+ channel inactivated at pH 4.0 in low and high millimolar concentrations of potassium (**Fig. 5**). This led us to conclude that the selectivity filter can reside in a collapsed and therefore inactivated conformation in the presence of high potassium concentrations underpinning its role as central component of the channel's inactivation gate. Moreover, we identified PA and PE to be stabilizers of the closed-conductive resting state of KcsA-Kv1.3. Combination of high potassium concentrations and these lipids shifted the steady-state equilibrium between resting and inactivated gating states of the KcsA-Kv1.3 channel. As a result, the resting state is the prevailing state at pH 4.0 in DOPC/DOPA (7:3).

Mutational as well as spectroscopic data showed that activation of the channel is driven by electrostatic repulsion of residues located on the intracellular side of the TM2 helices (**Chapter 4**).[133] At neutral pH particularly Arg and Glu residues form a network of polar contacts stabilizing the TM2 helices in a conformation which precludes ion permeation. Protonation of Glu and His residues leads to electrostatic repulsion of the remaining positively charged residues establishing the open channel conformation (**Fig. 6b**). Our present data implies that potassium and lipid effects contribute to the energetic differences between the different gating states of the channel. We showed that potassium most likely acts via distinct binding sites in or close to the selectivity filter inducing the open conformation of the inactivation gate (**Chapter 4**). This binding effect seems to be transferred to the activation gate by distinct sidechain interactions coupling the two channel gates (**Fig. 6b**). Lipids located in the non-annular lipid binding sites of the K^+ channel might stabilize the resting state in analogy to their contribution to the overall tetramer stability discussed above. In favor of this, we observed strong signal reduction for residues located close to the non-annular binding site (e.g. Ala50, Asp64) if the channel entered the inactivated state.[71] Furthermore, channel opening is associated with a widening of the channel's pore altering the characteristic inverted tepee-like structure of the resting state (**Fig. 6b**). Apart from the effective radius of the channel protein this rearrangement could in principal also affect the hydrophobic length of the channel. Such a change could be for example induced by interactions of uncompensated positively charged residues located in the opened activation gate with negatively charged phospholipids (**Fig. 6b**). Hence, also physical lipid bilayer properties (see e.g. ref. 146 for review) related to the intrinsic lipid curvature or even hydrophobic mismatch might contribute to the lipid dependent stabilization of the resting state at pH 4.0. This hypothesis is supported by the observation that the stabilizing lipids PA and PE are characterized by a cone-like shape resulting in a

high intrinsic lipid curvature while their net charge is different. Moreover, the stabilizing effect of PA on tetramer stability seemed to be strongly reduced at pH 4.0, while PA stabilized the KcsA-Kv1.3 resting state at acidic pH. This might mean that charge or the superior hydrogen-bonding potential of PA are not the exclusive molecular basis for stabilization of the channel's resting state but that also structural frustration of lipids has to be considered.

In summary, our results establish that external parameters like the substrate K^+ and lipids can contribute strongly to the delicate control of the KcsA channel's gating cycle and have the potential to quantitatively change the steady state equilibrium of K^+ channel gating states.

Materials and methods

Materials. 1,2-dioleoyl-sn-glycero-3-phosphocholine (DOPC), 1,2-dioleoyl-sn-glycero-3-phosphate (DOPA), 1,2-dioleoyl-sn-glycero-3-phosphoglycerol (DOPG), 1,2-dioleoyl-sn-glycero-3-phosphoethanolamine (DOPE) and Cardiolipin (Heart, Bovine) were purchased from Avanti Polar Lipids, Inc (Alabaster, AL).

Sample preparation. KcsA-Kv1.3 expression, purification and reconstitution into liposomes was done as described previously.[13] Reconstitution was performed at a 100/1 lipid/KcsA-Kv1.3 molar ratio. pH and K^+ titrations were performed by thoroughly washing the proteoliposomal pellet with the desired phosphate or citrate buffers followed by 30 min ultracentrifugation at 45000 rpm and +4°C (compare ref. 138). KcsA expression, purification and reconstitution was done as described previously.[163]

Gel mobility shift assays. Constant aliquots of suspensions of KcsA and KcsA-Kv1.3 proteoliposomes in the indicated buffer were incubated with variable amounts of pure TFE (%, v/v) for 1 h at room temperature. Next, these samples were mixed with electrophoresis sample buffer (50 mM Tris-HCl, pH 6.8, 50% glycerol, 0.01% bromophenol, blue and 10% SDS) and run on 15% acrylamide gel (0.1% SDS) at room temperature. Tetramer bands were quantified by densitometry and plotted with respect to the band obtained for 0% TFE against TFE concentration.

Solid-state NMR spectroscopy. All NMR experiments were conducted using a 3.2 mm triple-resonance (^1H,^{13}C,^{15}N) probehead at a static magnetic field of 16.5 T corresponding to a proton resonance frequency of 700 MHz (Bruker Biospin). Magic angle spinning was employed at a frequency of 10.92 kHz. The effective sample temperature was set to approximately +7°C. Integration of spectral cross peaks was performed using the software Topspin 2.1 (Bruker Biospin).

Chapter 6

Protein dynamics detected in a membrane-embedded K^+ channel using two-dimensional solid-state NMR spectroscopy

Christian Ader[1,2]
Olaf Pongs[3]
Stefan Becker[2]
Marc Baldus[1,2]

[1] Bijvoet Center for Biomolecular Research, Utrecht University, The Netherlands
[2] Max-Planck-Institute for Biophysical Chemistry, Germany
[3] University Hospital Hamburg-Eppendorf, Germany

Biochimica et Biophysica Acta, Biomembranes **in press**

Abstract

We demonstrate that solid-state NMR can be used to probe residue-specific backbone dynamics in a membrane-embedded protein. Longitudinal ^{15}N relaxation rates were obtained from two-dimensional (^{15}N, ^{13}C) chemical-shift correlation experiments for the potassium channel KcsA-Kv1.3 reconstituted in multilamellar vesicles. We detected enhanced backbone mobility for two glycine residues within the selectivity filter that are highly conserved in potassium channels and that are of core relevance to the filter structure and ion selectivity.

Introduction

Protein dynamics play an essential role for molecular function[174] and nuclear magnetic resonance (NMR) has become a premier method to probe molecular dynamics at atomic resolution in solution.[175,176] For more than two decades (see, e.g., refs. 177, 178), solid-state NMR (ssNMR) has provided spectroscopic means to study molecular structure and dynamics in a membrane environment where molecular size increases and protein structure is modulated by the presence of a surrounding bilayer matrix.[179] With recent advancements in the field of Magic-Angle-Spinning (MAS[180]) based ssNMR on membrane proteins (see, e.g., refs. 56, 181, 182), the structural analysis of larger membrane-embedded proteins becomes feasible. For example, we have shown that for the chimeric KcsA-Kv1.3 potassium channel, ligand binding and channel inactivation can be studied at atomic level.[10,13,71,138] KcsA-Kv1.3 shares essential structural and functional features with the KcsA channel first identified in the gram-positive bacterium *Streptomyces lividans*.[45] KcsA has been characterized by a variety of structural and biophysical techniques and high resolution structural information is available.[46,117,165] The selectivity filter which entails the channel's high K^+ selectivity and specificity[51] constitutes an essential part of the K^+ channel and is highly conserved among potassium channels. During pH-induced activation, KcsA and KcsA-Kv1.3 channels rapidly inactivate. The inactivation is correlated with a conformational change of the filter from a conductive to a 'collapsed' conformation which renders potassium binding sites inaccessible and thereby blocks the passage of potassium ions. Crystal structures initiated a series of *in silico* molecular-dynamics (MD) studies[67,173,183-186] that addressed the importance of conformational flexibility in the selectivity filter for selective conduction of potassium ions. The dynamical dependence between filter and permeant ion was referred to as breathing motion and linked to the fundamental mechanism of ion gating.[186] MD simulations evaluating the energetics related to different ion occupancies within the selectivity filter suggested a two state conduction pathway for the permeant ion.[184,187] This is supported by electron density profiles obtained for K^+ and larger analogues like Rb^+ located in the selectivity filter of KcsA.[188] Experiment and simulation showed that filter stability depends crucially on the presence of potassium.[46,104,173,189,190] Mutations in the selectivity filter and within its close proximity strongly affect stability and gating properties of the potassium channel[83,86,87,160,191,192], confirming that conformational dynamics of the selectivity filter and its molecular environment play an in important role for channel gating.[84,86-88,122-128,193]

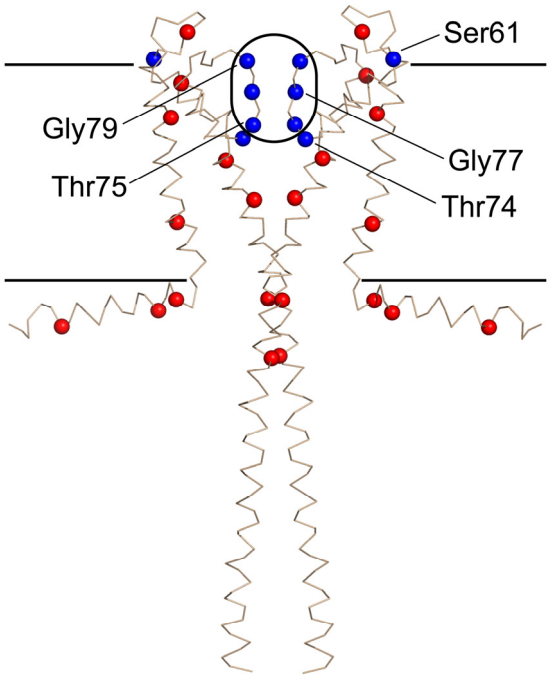

Figure 1. Structural model for KcsA-Kv1.3 comprising residues 1-160 (only 2 subunits of the channel are shown) based on the crystal structure of full-length KcsA (PDB ID 3EFF)[165] and a full-length model based on EPR data for residues 1-24 (PDB ID 1F6G).[63] Residues stated in the text and the following figures are labeled. Nitrogen atoms for which site specific longitudinal relaxation rates (R1) could be obtained are illustrated as blue spheres. Gly residues other than Gly77 and Gly79 are marked by red spheres. The selectivity filter of the potassium channel is marked by a black frame. The lipid bilayer is indicated by black lines.

In principle, ssNMR provides an experimental means to directly examine ion channel dynamics in a bilayer environment and in different functional states. Compared to solution-state NMR, ssNMR provides a more direct measure for internal mobility, as no overall tumbling of the molecule has to be considered. Moreover, spectral resolution is not determined by the micellar surrounding, instead the type and nature of the lipid bilayer can be readily varied providing insight into membrane effects on protein structure and dynamics (see, e.g., ref. 194, **Chapter 5**). For KcsA-Kv1.3, previous dipolar ssNMR correlation spectra speak in favor of a well defined structure in a membrane setting.[10] Here, we probed ^{15}N nuclear spin relaxation times to obtain a more detailed view of KcsA-Kv1.3 backbone dynamics with particular attention to selectivity filter residues. Following pioneering work by Torchia *et al.*[195,196] and more recent studies on solid-phase globular proteins[37,197], we show that two-dimensional ssNMR in combination with ^{15}N-edited relaxation filtered spectroscopy provides a promising means to probe channel backbone dynamics in lipid bilayers.

Results

As previously shown, KcsA-Kv1.3 residues Thr74, Gly77, and Gly79 are essential for binding K^+ ions in the selectivity filter. These residues can readily be resolved in N-Cα correlation spectra. Our spectral analysis also included Thr74, close to the inner entrance of the filter, and Ser61, located in the turret region at the extracellular side of the KcsA-Kv1.3 channel (**Fig. 1**). Together with a set of α-helical Gly residues, several residue-specific probes were hence available for spectroscopic analysis. Obviously, the number of residues to be investigated could be increased by conducting NCACB[198] experiments, possibly even in three spectral dimensions. For reasons of spectroscopic sensitivity, such experiments were not attempted here.

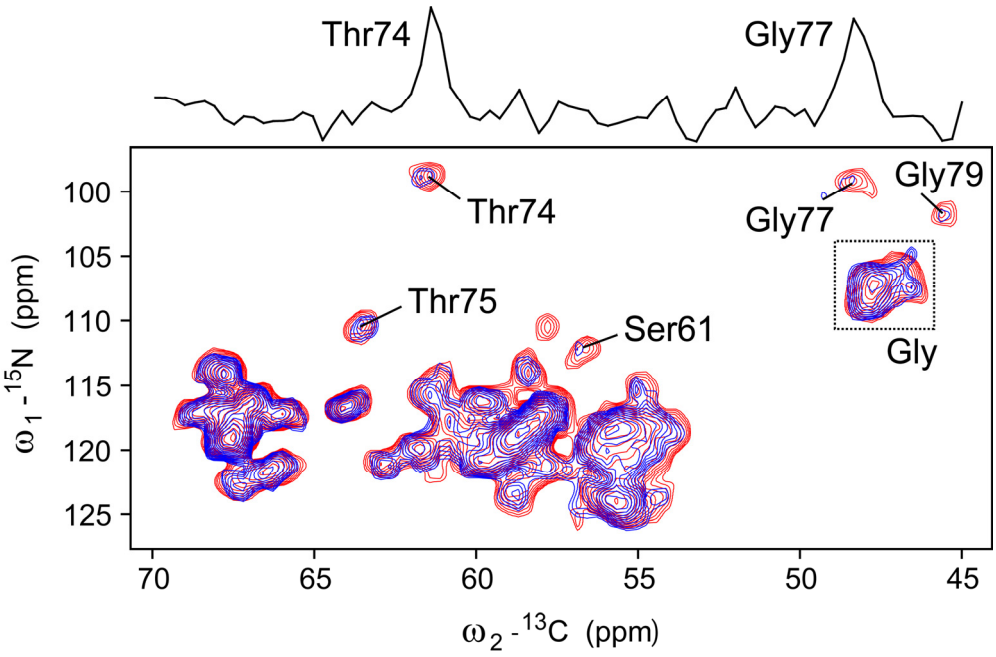

Figure 2. Superposition of ^{15}N-^{13}C correlation spectra obtained for membrane embedded KcsA-Kv1.3 using ^{15}N spin-lattice relaxation delays of τ = 5 s (red) and τ = 20 s (blue). Resonances due to residues discussed in the text are labeled. The Gly N-Cα region is marked by a dashed box. The one-dimensional slice was extracted from the 2D spectrum employing τ = 5 s at a ^{15}N chemical shift of 99 ppm.

In **Figure 2**, we present relaxation-edited N-Cα correlation spectra obtained for longitudinal ^{15}N delays of 5 and 20 s. Visual inspection of the spectra readily revealed a qualitative difference between residues Gly77 and Gly79, which occur at the upper, and Thr74 and Thr75, which occur at the lower part of the selectivity filter. Our data show that spin-lattice relaxation proceeds faster for Gly77 and Gly79 than for Thr74 and Thr75. In order to distinguish whether this observation originates from increased local mobility in the upper part of the selectivity filter or from larger motional freedom intrinsic for Gly residues, we included the Gly N-Cα region (dashed box in **Fig. 2**) in our analysis. KcsA-Kv1.3 contains thirteen glycines per subunit, mainly located in helical segments of the KcsA-Kv1.3 channel. Subsequently, we determined peak volumes for the five resolved signals and the Gly region and subtracted noise levels by integrating and subtracting corresponding noise regions of the individual spectra to avoid systematic overestimation of small peak volumes obtained at long relaxation delays. In order to correct for different experiment times we normalized peak volumes by the number of acquired scans. The resulting corrected peak integrals were standardized to the respective data point obtained for the relaxation delay of 5 s and data were fitted to an exponential decay in order to determine R_1's (**Fig. 3a**). No correction for effects of magic angle spinning on R_1 and ^{15}N spin diffusion[37,197] was applied. Based on the signal to noise of our spectra, we estimate that our site specific R_1's are associated with an error of approximately 0.01 s^{-1}. For residues Gly77 and Gly79 we measured ^{15}N backbone R_1's of 0.049 s^{-1} and 0.050 s^{-1}, respectively (**Fig. 3b**). These values are significantly larger than the average value of 0.024 s^{-1} obtained for KcsA-Kv1.3. Notably, signals contributing to the Gly N-Cα region are

characterized by a comparatively slow relaxation rate of 0.011 s^{-1}; more than four times smaller than the relaxation rates obtained for the two Gly residues in the selectivity filter. On the other hand, we found ^{15}N backbone R_1's for residues Thr74 and Thr75 of 0.030 s^{-1} and 0.019 s^{-1}, respectively. The data suggest that increased mobility as observed for Gly77 and Gly79 is locally confined to the upper part of the selectivity filter. By contrast, Thr74 and Thr75 at the lower part of the selectivity filter have a local mobility similar to the average channel backbone. In this context, it is interesting to note that mutation of Thr75 was not only found to change ion affinity but also substantially affected the thermal stability of the channel tetramer.[160]

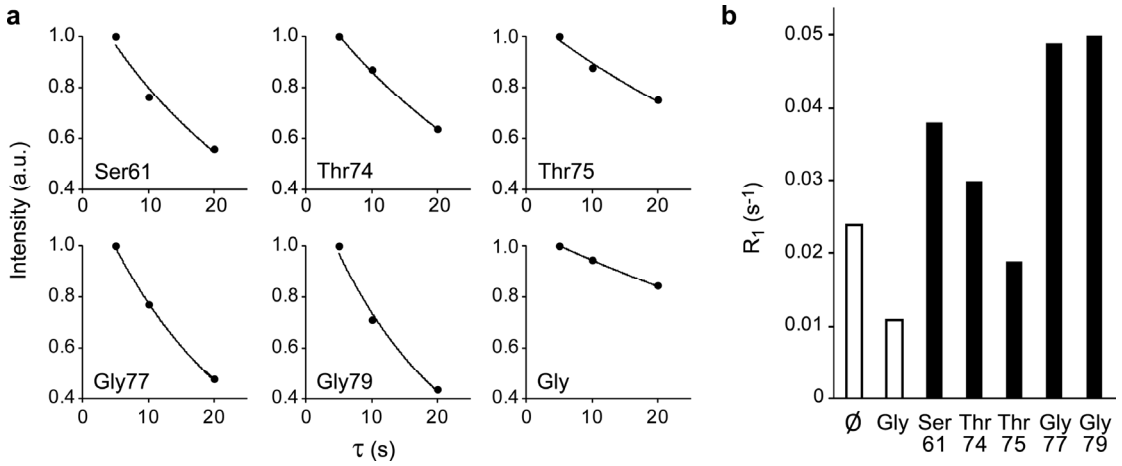

Figure 3. (***a***) Decay curves measured for Ser61, Thr74, Thr75, Gly77, Gly79, and the Gly N-Cα region. Corrected intensity values obtained for three relaxation delays (τ = 5, 10, and 20 s) were renormalized so that the data point for τ = 5 s has an intensity value of 1. Solid curves give exponential fits to the data. (***b***) Bar graph summarizing the determined average (Ø) and site-specific ^{15}N spin-lattice relaxation rates.

This affect on global channel stability agrees with our finding that the lower part of the selectivity filter exhibits less backbone dynamics than the remaining filter segments. Finally, we determined a ^{15}N backbone R_1 of 0.038 s^{-1} for Ser61. This residue is located in the extra-cellular loop of KcsA-Kv1.3 and displays mobility above the protein's average. Nevertheless, the Ser61 value does not exceed T_1 rates observed for the Gly residues in the upper selectivity filter. The data is consistent with the idea that residues in the turret region are well structured in the resting state of the channel at pH 7.5[10] but likely exhibit higher molecular dynamics in the context of pH-induced gating.[71] On the basis of ^{15}N backbone R1's we have color coded in **Figure 4a** the relative differences in local mobility observed for KcsA-Kv1.3 filter residues. For reference, selectivity filter residues affected by ligands which induce a distorted conductive (KTX, refs. 13, 140) or collapsed (porphyrin, ref. 71) backbone structure are included. Interestingly, filter residues identified as mobile are involved in both ligand binding modes. Next, we compared our results to crystallographic B-factors obtained for KcsA crystallized in the absence and presence of an FAB antibody (**Fig. 4b, c**). Neither of the two data sets shows qualitative agreement to our spectroscopic analysis. This disagreement may originate from the different conditions in which the KcsA channel structures were

studied including parameters like pH, temperature, ionic strength, and lipid environment. For example, the crystal structures were obtained using detergent solubilized KcsA, whereas ssNMR data base upon proteoliposome preparations. In fact, comparison of both X-ray data sets suggests that B-factors seem to depend mainly on the environment of the channel, i.e, residing in a free crystalline state or when bound to an FAB antibody.
Previously, solution-state NMR studies of KcsA variants were conducted at pH 7.5 in SDS micelles that revealed a molecular conformation comparable to the available crystal structures and allowed to examine ^{15}N relaxation rates as a quantitative measure of structural mobility.[92,93] These data suggested increased backbone mobility for the N- and C-terminal segments of closed KcsA and excluded backbone dynamics on the ps-ns time scale for selectivity filter residues at neutral pH. However, under such conditions, pH-induced gating could not be followed. Instead, solution-state NMR of KcsA in DDM and foscoline micelles were used to gain insight in pH sensing and dynamics related to activation gating.[91,94] For example, Riek *et al.* followed structural dynamics of residue Y78 in the selectivity filter as a function of pH based on $^3J(^1HN,^1H\alpha)$ scalar couplings.[91] This data revealed millisecond timescale motions in the filter that were attributed to exchange between low and high K^+ affinity states. On the other hand, we previously observed significantly larger structural changes after inactivation in lipid bilayers[71] compared to solution-state NMR studies. It suggests that protein dynamics are significantly different in a micellar versus a lipid bilayer. This is consistent with the idea that composition and mechanical status of the lipid bilayer have a profound influence on K^+ channel gating and stability underlining the utility of ssNMR-based dynamic studies in a native or native-like membrane setting. Here, we showed the ^{15}N R1's are accessible for KcsA-Kv1.3 in a membrane setting revealing increased backbone dynamics in the upper selectivity filter of the closed channel at neutral pH. This approach may be used in the future to follow filter dynamics as a function of parameters such as pH or ion concentration controlling potassium channel function.

Discussion

We have determined ^{15}N longitudinal relaxation rates for individual residues of KcsA-Kv1.3 in lipid bilayers. The experiments allow for a qualitative description of local backbone dynamics in the selectivity filter in reference to other segments of a membrane embedded potassium channel. Site specific R_1's ranged from 0.019 s^{-1} to 0.050 s^{-1} at 18.8 T, and the average protein backbone relaxation can be described by an overall rate of 0.024 s^{-1}. In absolute numbers, the values compare favorably to data obtained on a crystalline protein at different magnetic fields. Our experiments confirm earlier conclusions based on dipolar ssNMR correlation spectroscopy[10] that KcsA-Kv1.3 resides in a well defined structure in a membrane setting. We observe a locally increased mobility for Gly77 and Gly79 in the upper part of the KcsA-Kv1.3 selectivity filter, while the Thr74 and Thr75 residues in the lower part display local dynamics similar to the average protein backbone.

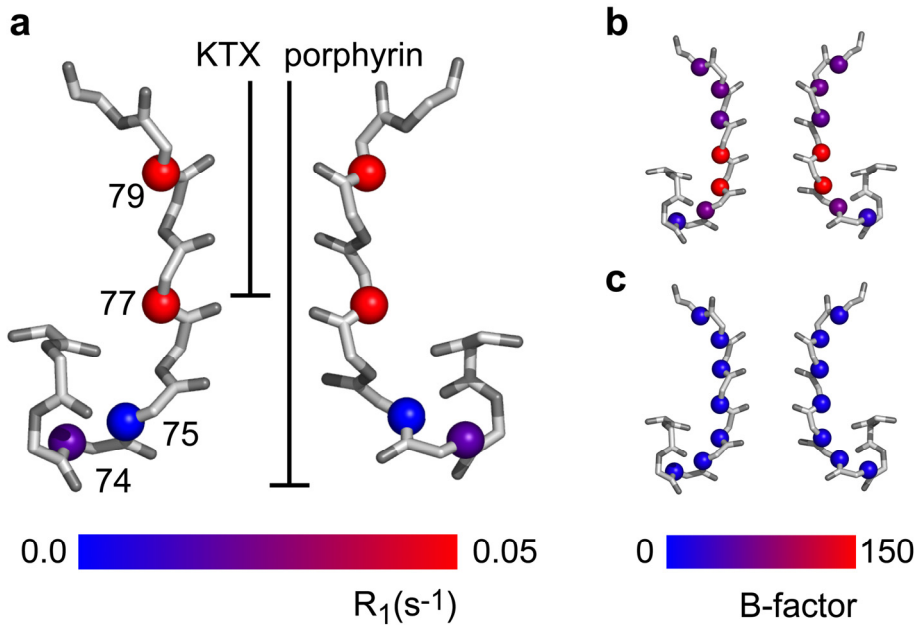

Figure 4. (***a***) Selectivity filter of KcsA (PDB ID 1K4C).[46] Backbone nitrogens for which R1's were determined are depicted as spheres. R1's are indicated by a color gradient from blue (R1=0 s^{-1}) to red (R1=0.05 s^{-1}). Bars indicate the residues affected by KTX and porphyrin binding, respectively. B-factors reported for backbone nitrogens of the selectivity filter and the two neighboring residues for KcsA crystal structures obtained in the absence (***b***, PDB ID 1BL8)[117] and presence (***c***, PDB ID 1K4C)[46] of FAB antibodies. B-factors are indicated by a color gradient from blue (B=0) to red (B=150).

The two glycine residues are highly conserved in the pore of K^+ channels and their conformational dynamics are of crucial importance to the filter structure and ion selectivity (see, e.g., refs. 83, 191). Here, we found for the channel's resting state that these residues are also characterized by distinctly high backbone mobility. We propose that this mobility is an essential property of the filter to dynamically respond to the binding and unbinding of ions while they pass along the K^+ binding sites in the filter during ion permeation. Furthermore, backbone plasticity of the selectivity filter may be critical for the gating transition of the K^+ channel involving conductive and 'collapsed' filter conformation or the binding of ligands to the channel pore. The results underline that T_1 relaxation rates provide a powerful means to follow site-specific dynamics in larger membrane-embedded proteins by solid-state NMR. To further dissect dynamical details associated with K^+ channel function site-resolved measurement of ^{15}N backbone dynamics may in the future be assisted by measurements of transversal protein relaxation rates[199] or by a more detailed analysis of ssNMR chemical shifts and cross-peak amplitudes as recently demonstrated for other membrane proteins.[11,200]

Material & Methods

Sample preparation. Protein expression, isotope-labeling and reconstitution in asolection liposomes were done as previously described.[71] The sample used for this

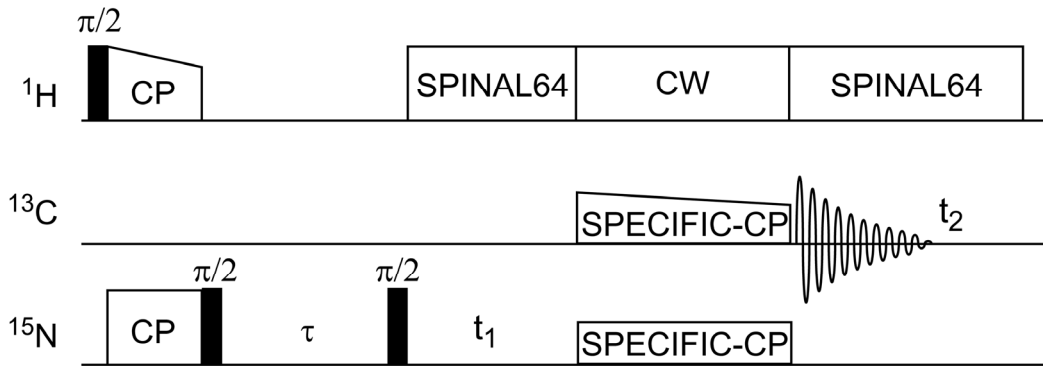

Figure 5. Pulse sequence used to encode ^{15}N spin-lattice relaxation rates in ^{15}N-^{13}C correlation spectra. All spectra were obtained at about 283 K and 12.5 kHz MAS.

study contained approximately 150 nmol (10 mg) uniformly (^{13}C, ^{15}N) labeled KcsA-Kv1.3. The protein to lipid ratio was 1:100 (mol/mol) and the water content of the sample was about 50% (w/w).

Solid-state NMR spectroscopy. Site-specific ^{15}N nuclear longitudinal relaxation rates (R_1) were measured using two-dimensional R_1-edited (^{15}N,^{13}C) correlation experiments. The corresponding pulse sequence is shown in **Figure 5** and was adapted from previous R_1 investigations[37,197] on a microcrystalline protein by incorporation of a SPECIFIC-CP[20,201] transfer step. As a result, the ^{15}N,^{13}C heteronuclear correlation spectrum is dominated by N-Cα correlations. All spectra were obtained at about 283 K and 12.5 kHz MAS using a 800 MHz instrument (Bruker Biospin Karlsruhe). The ^1H-^{15}N cross polarization (CP) step employed a linear ramp (100 to 80% field strength) on the ^1H channel. The CP period was 0.75 ms and the ^{15}N field strength was set to 35 kHz. The 2.5 ms ^{15}N-^{13}C CP step used a linear ramp on the ^{13}C channel and a ^{15}N field strength of about 34 kHz establishing SPECIFIC[20,201] transfer. ^1H decoupling was obtained by SPINAL64[77] and continuous wave (CW) with a decoupling field of 83.3 kHz. Spectra were obtained for three spin-lattice relaxation times (5, 10, and 20 s). We acquired 176-560 scans for each of the 40 increments in t_1. Maximum acquisition times in t_1 and t_2 were 4 ms and 10 ms, respectively. The total experimental time for the spectra analyzed was about 140 hours. In order to minimize effects due to changes in CP-efficiencies over the course of the experiment, spectra were acquired in interleaved steps and added after the whole dataset was completed. Furthermore, we monitored CP-efficiencies in between individual two-dimensional (2D) experiments by acquiring 1D control spectra. During the course of data collection, we did not observe any sizable intensity changes in the ssNMR spectra. The average ^{15}N nuclear longitudinal relaxation rate of KcsA-Kv1.3 was measured by fitting the integrals of a series of 1D ^1H-^{15}N cross polarization (CP) spectra with an additional spin-lattice relaxation time before detection. For the external magnetic field of 18.8 T we obtained an average relaxation rate of 0.024 s^{-1} measured at an effective temperature of 283 K. This value compares favorably to values found for a microcrystalline protein.[37,197]

Chapter 7

Amyloid-like interactions within nucleoporin FG-hydrogels

Christian Ader[1,2]
Steffen Frey[2]
Werner Maas[3]
Dirk Görlich[2]
Marc Baldus[1,2]

[1] Bijvoet Center for Biomolecular Research, Utrecht University, The Netherlands
[2] Max-Planck-Institute for Biophysical Chemistry, Germany
[3] Bruker Biospin Inc., USA

Manuscript under Review

Abstract

The 62 kDa FG/FxFG-repeat domain of the yeast nuclear pore complex protein Nsp1p forms a hydrogel-based permeability barrier that excludes inert macromolecules, but allows rapid entry of nuclear transport receptors (NTRs). Gelation involves a hydrophobic collapse of Phe-rich clusters within the domain. Using solid-state NMR spectroscopy, we now identified two additional types of intra-gel interactions, namely transient hydrophobic interactions between Phe and methyl side chains as well as intermolecular β-sheets between Asn-rich spacer regions. The latter also characterize neuronal inclusions or prions formed by Asn/Gln-rich amyloid proteins. This reveals a fully unexpected physiological function of such inter-chain β-structures. Our data suggest a plausible explanation for how contacts between FG-repeats gain the kinetic stability to suppress passive fluxes through nuclear pores and yet allow rapid NTR passage.

Introduction

The permeability barrier of nuclear pore complexes (NPCs) controls all nucleo-cytoplasmic exchange.[202,203] It allows free passage of small molecules, but suppresses the flux of macromolecules larger than 30 kDa and thereby prevents an uncontrolled intermixing of nuclear and cytoplasmic contents. However, the permeability barrier also permits a rapid passage of even large cargoes, provided these are bound to appropriate nuclear transport receptors (NTRs). NTRs thereby supply nuclei with proteins and the cytoplasm with nuclear products such as ribosomes or tRNAs.

FG-repeat domains are essential building blocks of NPCs.[204] They are considered to be natively unfolded and they contain up to 50 repeat units, in which a characteristic hydrophobic patch, typically with the sequence FG, FxFG or GLFG, is surrounded by more hydrophilic spacer sequences.[205-207] These hydrophobic patches transiently bind NTRs during facilitated NPC-passage.[49,208-212]

Recent evidence suggests that the permeability barrier is a hydrogel derived from FG-repeat domains (FG-hydrogel).[49,211,213,214] Indeed, FG-hydrogels could be reconstituted from the FG/FxFG domain of the yeast nucleoporin Nsp1p or the GLFG-domains from Nup49p and Nup57p, all showing permeability properties very similar to those of NPCs themselves: they allowed an up to 20 000-fold faster entry of large NTR-cargo complexes than of the respective cargo alone.[49,213,215]

Within the 600 residues FG-repeat domain of Nsp1p ($FG/FxFG^{Nsp1p}_{2-601}$), phenylalanines are critical not only for NTR-binding, but also for gel-formation[49], suggesting that inter-repeat contacts involve some form of hydrophobic interaction.

According to the selective phase model[211,213,216], FG-hydrogels are reversibly-crosslinked 3-dimensional protein meshworks, whose mesh size determines their size-exclusion limit for inert objects. NPCs already significantly restrict the flux of GFP-sized objects (diameter ≈ 5 nm).[216] Cargo-NTR complexes, however, are typically much larger than GFP and thus exceed the expected mesh size. Yet they cross NPCs in a facilitated manner. This implies that inter-repeat contacts dissociate rapidly in the vicinity of an NTR, but are kinetically stable elsewhere in the gel.[213] To understand this phenomenon, we foremost need structural information on FG-repeat interactions. As gels are intrinsically disordered and

insoluble, such information is difficult to obtain by X-ray crystallography or solution NMR. Solid-state NMR (ssNMR), however, proves to be the ideal technique to study both formation and structural organization of an FG-hydrogel.

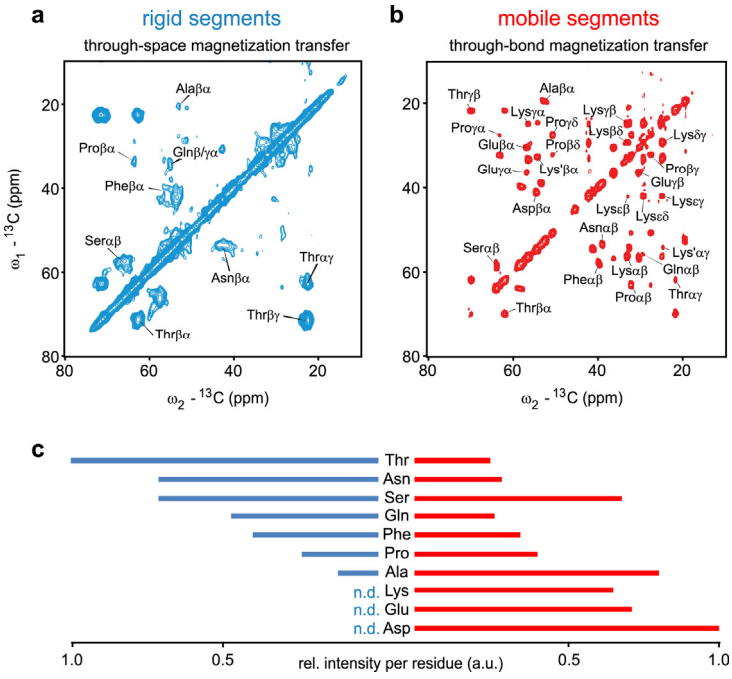

Figure 1. Investigation of rigid and mobile segments of the Nsp1-hydrogel using 2D (^{13}C-^{13}C) ssNMR employing through-space (***a***) and through-bond (***b***) mixing. Amino-acid specific assignments are indicated. (***c***) Relative (rel.) Cα-Cβ peak intensities per residue obtained from both spectra allow to estimate the amino-acid distribution within the rigid **(**left, blue**)** and mobile **(**right, red**)** segments of the hydrogel (n.d.: no Cα-Cβ peak detected).

Results

The FG-hydrogel contains rigid and highly dynamic segments

To probe mobile as well as rigid segments of a fully carbon (^{13}C), nitrogen (^{15}N) isotope-labeled FG/FxFG$^{Nsp1p}_{2–601}$-hydrogel in a complementary manner, we acquired two-dimensional (^{13}C-^{13}C) correlation spectra employing through-space and through-bond mixing units[40,217] (**Fig. 1a**, **b**). Even without sequential resonance assignments for this 62 kDa protein domain, NMR line widths, peak positions and the overall correlation patterns clearly distinguish dynamically different protein segments. The established standard amino-acid specific peak positions[218] can be used to approximate the relative distribution of amino acids within the rigid and the mobile segments (**Fig. 1c**). The mobile, unstructured segments contain large fractions of the charged amino acids Asp, Glu and Lys, while Thr, Asn, and Gln residues characterize the rigid segments, possibly acting as anchoring points of the gel network. This is striking because so far only hydrophobic interactions, especially such involving Phe, have been considered to stabilize the FG-hydrogel.[49,211,216] Phe residues, however, appear to reside balanced between both motional regimes. This might reflect the paradox that inter-repeat contacts must be kinetically stable enough to pose a firm barrier while, at the same time, phenylalanines must rapidly bind approaching NTRs and transmit the signal for opening a mesh.

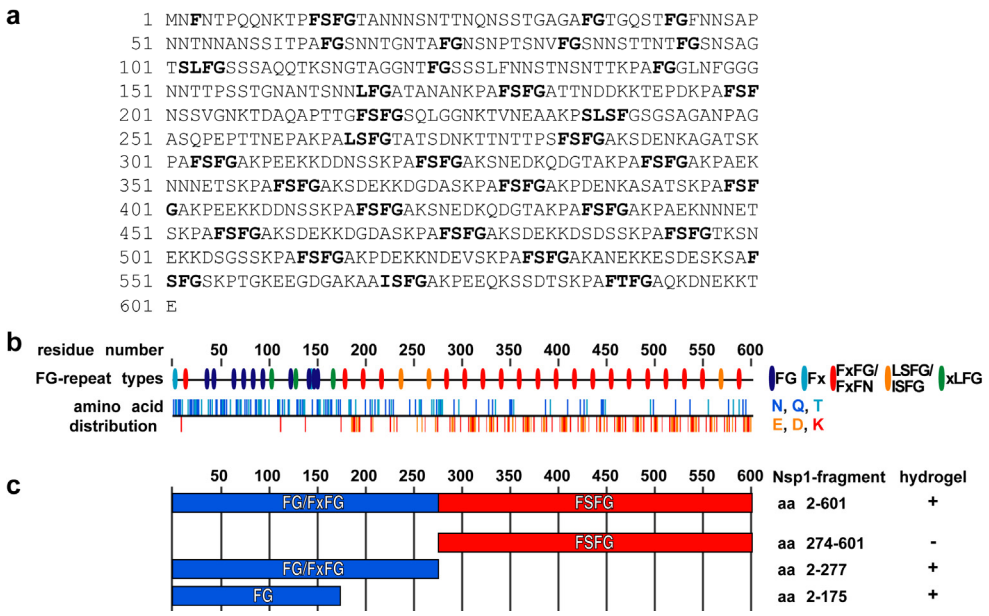

Figure 2. Gelation propensity correlates with the content of Asn, Gln and Thr within the inter-FG-spacers. (***a***) Sequence of $FG/FxFG^{Nsp1p}_{2-601}$. FG-repeats are printed bold. (***b***) Linear representations illustrating the non-uniform distribution of the various FG-repeat types (top) and relevant amino acids (bottom) within the $FG/FxFG^{Nsp1p}_{2-601}$-domain. (***c***) Bar models of Nsp1p fragments with high and low gel-forming propensity.

The N- and C-terminal halves of the $FG/FxFG^{Nsp1p}_{2-601}$ domain differ quite significantly in their amino acid composition (**Fig. 2a, b**). The more heterogeneous N-terminal half ($FG/FxFG^{Nsp1p}_{2-277}$) consists (in addition to the abundant FG motifs) mainly of Asn-, Gln-, Thr-, and Ser-rich (NQTS-rich) spacers, while the C-terminal half ($FSFG^{Nsp1p}_{274-601}$) comprises highly repetitive FSFG-repeats with highly charged spacers. If the rigid segments seen by ssNMR spectroscopy were crucial for hydrogel stability, then the isolated N-terminal half should show a greater gelation propensity than the C-terminal half. Indeed, the N-terminus formed a functional hydrogel, while the C-terminus remained liquid under identical conditions (**Fig. 2c, Table 1**). The gelation potential of an even shorter N-terminal fragment (FG^{Nsp1p}_{2-175}), lacking nearly all charged residues, was at least as strong as that of the complete repeat domain (**Fig. 2c, Table 1**).

The hydrogel is stabilized by hydrophobic and hydrophilic interactions

Line widths and peak positions[218] in the NMR spectrum employing scalar-based polarization transfer indicate that mobile segments are largely unstructured (**Fig. 1b**). This is supported by the occurrence of only very few inter-residue crosspeaks in proton-proton (^1H-^1H) NOESY[42] spectra (**Fig. 3a**), even at long contact times. Because of limited spectral dispersion and the large size of the repeat domain, Phe-Phe interactions proposed previously to stabilize the hydrogel as well as other interactions between identical side chains could not be probed by two-dimensional NMR. Strikingly however, the NOESY spectra of both full length and N-terminal Nsp1-hydrogels revealed spatial vicinity between aliphatic side chain protons and

Repeat domain	Hydrogel formed?	Gel formed after	Appearance	Heating to 80°C
$Nsp1^{2\text{-}601}$	yes	< 4 h	strong gel	no effect
$Nsp1^{274\text{-}601}$	no			
$Nsp1^{2\text{-}277}$	yes	< 3 h	strong gel	no effect
$Nsp1^{2\text{-}277}$(T→S)	yes	24 h	weak, inhomogeneous gel	no effect
$Nsp1^{2\text{-}277}$(N→S)	waxy mass	< 2 min	inelastic, waxy mass	melts < 3min
$Nsp1^{2\text{-}277}$(FILV→S)	no			
$Nsp1^{2\text{-}175}$	yes	< 1 h	strong gel	no effect

Table 1. Gelation characteristics of various Nsp1p fragments and mutants. Included residues and introduced mutations are indicated in superscript or brackets, respectively. "T→S" indicates that all 39 Thr were mutated to Ser. Likewise, "N→S" indicates mutation of all 49 Asn to Ser, and "FILV→S" indicates mutation of all Phe, Ile, Leu and Val residues (a total of 35 residues) to Ser.

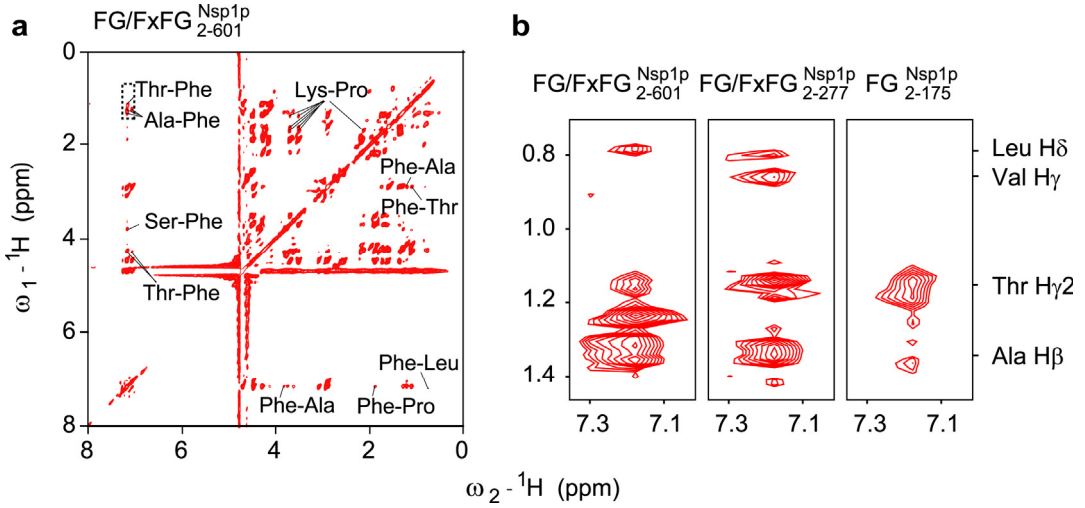

Figure 3. Comparison of NOESY spectra obtained for full length and N-terminal Nsp1-hydrogels. (***a***) Inter-residue crosspeaks observed for $FG/FxFG^{Nsp1p}_{2-601}$ are indicated. The other crosspeaks can be explained by intra-residue correlations. (***b***) Details of NOESY spectra (dashed box in ***a***) obtained for indicated Nsp1p fragments showing inter-residue crosspeaks between indicated side chain methyls and Phe side chains. In all cases, a (^{1}H-^{1}H) mixing time of 250 ms was used.

the aromatic ring protons of Phe, confirming hydrophobic interactions on a dynamic and likely transient level (**Fig. 3b**).

C', Cα, Cβ, and Hα chemical shifts are very sensitive to secondary structure elements[218] and concordantly point towards a β-strand backbone conformation within rigid NQTS-rich spacers (**Fig 4a, b**). In such conformations, sequential NH-Hα proton-proton distances should be short (2-3 Å), which is in line with the observed rapid magnetization transfer (maximum intensities at 100 µs ^{1}H-^{1}H mixing) from amid nitrogen atoms to the alpha carbons via directly bonded ^{1}H spins[65] (**Fig. 5a**). Furthermore, similar nitrogen-carbon correlation experiments

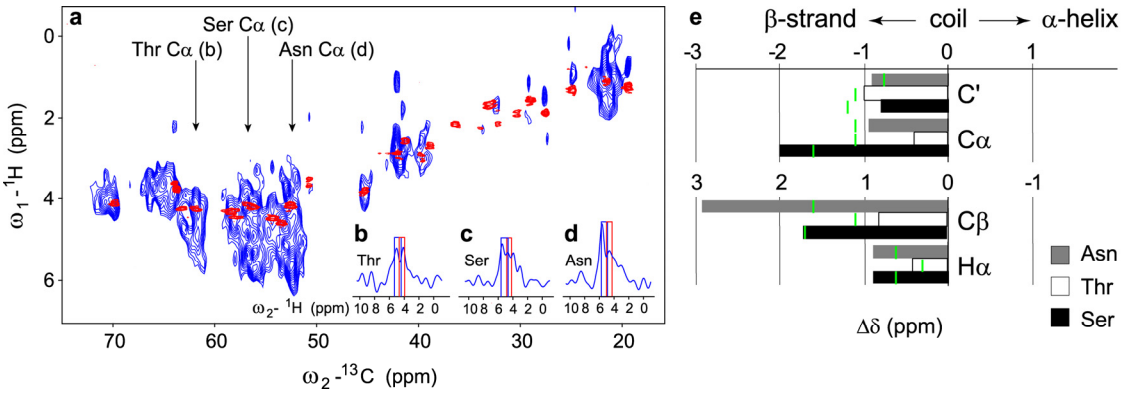

Figure 4. (***a***) INEPT-HETCOR (red) and frequency-switched Lee-Goldburg (blue) (^{1}H-^{13}C) correlation spectra probing ^{1}H chemical shifts for the mobile and rigid segments of the FG/FxFG$^{Nsp1p}_{2-601}$-hydrogel, respectively. Cα resonances of Thr, Ser, and Asn within the rigid segments are indicated by arrows and ^{1}H cross-sections for these resonances are displayed in ***b-d***. Boxes indicate statistical Hα chemical shift values for β-strand (blue) and random coil (red) conformations. The widths of the boxes are two times the standard deviations given by Wang and Jardetzky[218]. (***e***) Bar graph of C', Cα, Cβ, and Hα chemical-shift differences for resonances of rigid Asn, Thr, and Ser of FG/FxFG$^{Nsp1p}_{2-601}$ as compared to statistical average values for β-strands (green lines).

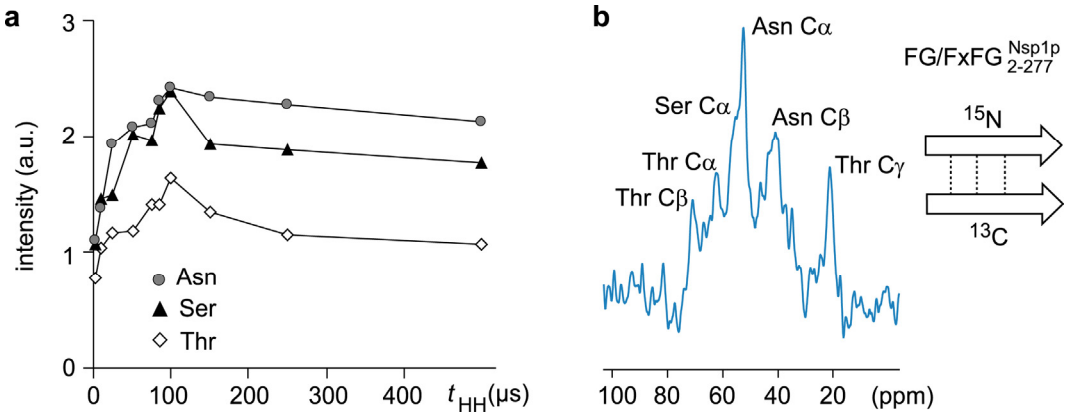

Figure 5. (***a***) Dependence of Cα peak intensities for Asn, Thr, and Ser on the ^{1}H-^{1}H mixing time (t_{HH}) in NHHC[65] experiments suggests NH-Hα ^{1}H-^{1}H distances compatible with β-strands. (***b***) NHHC spectrum obtained for a hydrogel containing ^{13}C-labeled FG/FxFG$^{Nsp1p}_{2-277}$ and ^{15}N-labeled FG/FxFG$^{Nsp1p}_{2-277}$ at a 1:1 ratio. The signal arises due to short ^{1}H-^{1}H distances between complementarily labeled β-strands forming an intermolecular sheet (see sketch).

performed on a 1:1 mixture of ^{15}N- and ^{13}C-labeled FG/FxFG$^{Nsp1p}_{2-277}$ demonstrated that these β-strands form intermolecular β-sheets (**Fig. 5b**).

We then analyzed the impact of threonines, asparagines and hydrophobic residues on hydrogel-formation (**Table 1**). While wild type FG/FxFG$^{Nsp1p}_{2-277}$ rapidly formed a rigid gel, exchange of all 35 hydrophobic residues (F, I, L and V) to serines abolished hydrogel formation, confirming our previous conclusion that

hydrophobic interactions drive gel formation.[49] Along the same line, mutating all 39 threonines to serines (T→S mutant) significantly delayed gelation and resulted in a weaker hydrogel compared to the wild type domain. Once formed, the wild type gel was stable and neither dissolved in excess of buffer nor melted at 80°C. The N→S mutant, however, formed an inhomogenous waxy mass that dissolved in excess of buffer and melted at 80°C, possibly because it lost rigid components of its inter-repeat contacts, i.e., stable H-bonds within backbone or side chain networks. Thus, threonine and asparagine not only reside within rigid segments of the FG-hydrogel, but they also stabilize the gel.

NQTS-rich spacers characterize various nucleoporins

Nucleoporins make up a functionally related group of proteins containing Q/N-rich regions in *Saccharomyces cerevisiae*.[204,219] The interactions observed for the $FG/FxFG^{Nsp1p}_{2-601}$ hydrogel could, therefore, be relevant for other proteins contained in this functional cluster. Dipeptide occurrences allow for comparison of different FG-repeat nucleoporins on the sequence level. Dipeptide statistics were obtained for a database of 12 FG-repeat domains of 11 nuclear pore proteins from yeast (**Table 2**). FG^{Nsp1p}_{2-175} shows the greatest gel-forming propensity within the entire Nsp1 FG-repeat domain. It is N/Q-rich and largely devoid of charged residues. This compositional feature is typical also for the FG-repeats from Nup116p, Nup100p, Nup57p, Nup49p and Nup42p. These domains define a distinct cluster within the FG-repeat nucleoporins considering pairwise correlation coefficients based on dipeptide statistics (**Table 3**). We analyzed Nup49p and Nup57p and found that their FG-repeat domains can also form a highly selective FG-hydrogel.[215]

Another cluster is represented by $FSFG^{Nsp1p}_{278-601}$ and the FG-repeats of Nup1p, Nup2p and Nup159p. It is characterized by a lower N/Q-content and high charge of the inter FG-spacers (**Tables 2** and **3**). In the case of $FSFG^{Nsp1p}_{278-601}$, this correlates with a low autonomous gel-forming propensity. However, our observation that the phenylalanines within the $FSFG^{Nsp1p}_{2-601}$- and $FSFG^{Nsp1p}_{1-175}$-hydrogels show comparable rigidities suggests that an FG-repeat domain with low gel-forming propensity can be incorporated into FG-hydrogels formed by N/Q-rich FG-repeats.

In summary, we find that NQTS-rich spacers between FG-motifs characterize not only the Nsp1p N-terminus, but, also FG-repeats from Nup116p, Nup100p, Nup57p, Nup49p and Nup42p. This suggests that several FG-repeat domains have the potential to contribute to the permeability barrier of the nuclear pore via the protein-protein interactions identified in this chapter. The highly charged $FSFG^{Nsp1p}_{274-601}$-domain, however, appears distinct and resembles the repeat domains of the peripheral nucleoporins Nup1p, Nup2p and Nup159p.

Structural models for amyloid-like interactions.

By ssNMR, we detected intermolecular β-sheets in a hydrogel containing a 1:1 mixture of separately ^{13}C- and ^{15}N-labeled proteins (**Fig. 5b**). In order to visualize these protein-protein interactions for a representative NQTS-rich spacer (**Fig. 6a**), we performed a molecular dynamics based protein docking using HADDOCK[107] (**Fig. 6b**, **c**). β-sheet assemblies can be stabilized by additional side chain stacking between proximal β-sheets as seen for Q/N-rich peptide-forming fibrils.[220]

FG-repeat domain	% N+Q	%S	%T	%charged (K+R+D+E)
Nup116$^{2\text{-}109;\ 167\text{-}743}$	28.4	12.1	9.9	1.9
Nup100$^{2\text{-}575}$	28.2	16.4	10.5	2.4
Nsp1$^{2\text{-}175}$	27.0	16.1	16.1	1.7
Nup57$^{2\text{-}287}$	24.1	11.9	14.0	2.5
Nup49$^{2\text{-}245}$	23.8	13.5	9.8	2.9
Nup145$^{2\text{-}211}$	22.4	16.7	13.3	2.9
Nup42$^{4\text{-}379}$	18.6	16.8	12.8	3.7
Nsp1$^{176\text{-}277}$	10.8	12.8	11.8	17.6
Nup2$^{53\text{-}541}$	10.3	16.2	8.6	27.5
Nup1$^{401\text{-}925}$	10.0	15.4	13.3	20.0
Nup159$^{454\text{-}887}$	7.4	22.2	8.6	17.8
Nsp1$^{278\text{-}601}$	6.7	14.9	4.6	34.8

Table 2. Amino acid compositions of *S. cerevisiae* nucleoporin FG-repeat domains. Positions of the FG-repeats within the respective full-length protein are indicated in superscript. Table is sorted according to the content of Gln+Asn (N+Q). The content of Ser (S), Thr (T) and of the charged residues Lys, Arg, Asp and Glu (K+R+D+E) was also calculated.

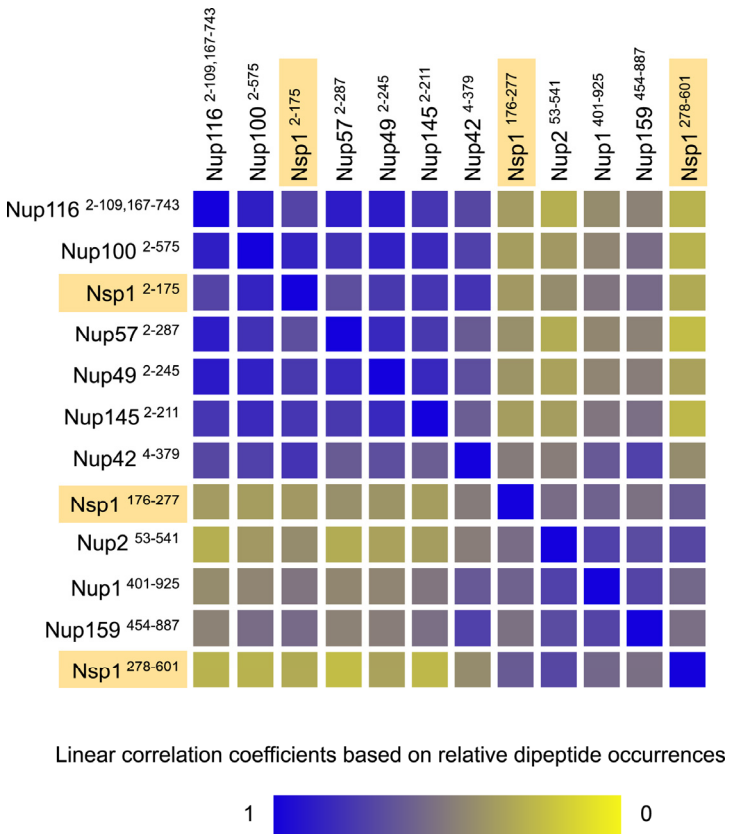

Table 3. Sequence similarity between FG-repeat domains illustrated by correlation of dipeptide occurrences. The occurrence of all possible 20^2 dipeptides were obtained for each sequences listed in Table 2 and compared pairwise by computing linear correlation coefficients, r. These are displayed using a continuous gradient from perfect correlation (blue, r = 1) to no correlation (yellow, r = 0).

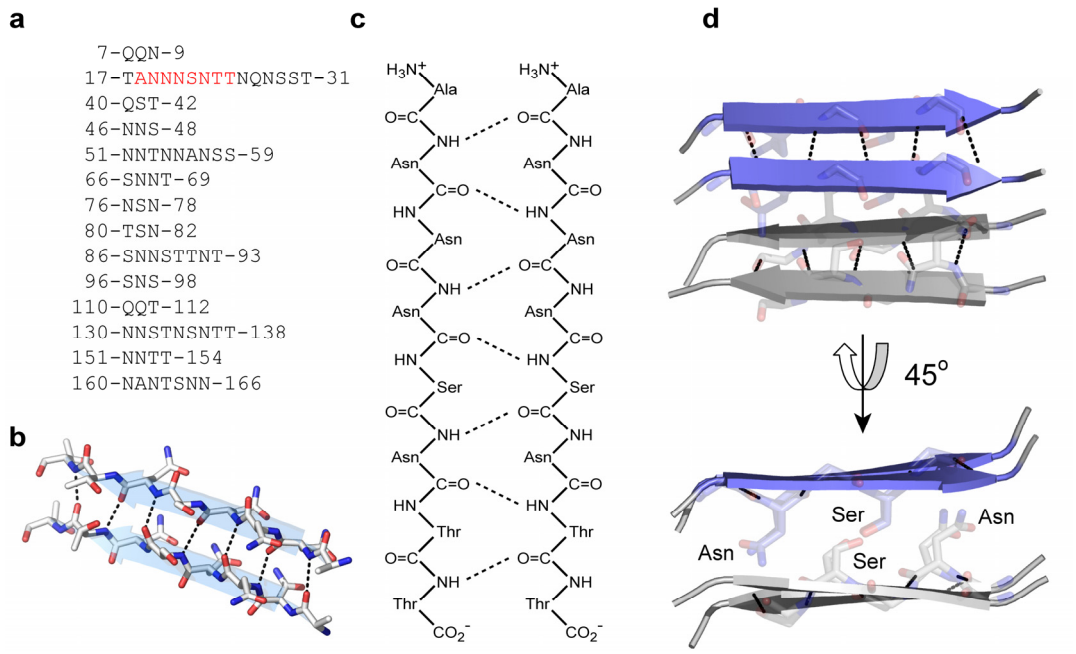

Figure 6. Structural models, created using HADDOCK (2), for interchain β-sheets between NQTS-rich spacers. (***a***) Sequences of NQTS-rich spacers found in FG^{Nsp1p}_{2-175} comprising at least 3 residues. (***b-d***) Lowest energy models as discussed in the text are shown in different orientations. Dashed black lines indicate inter-strand hydrogen bonds on the backbone level.

Although not yet confirmed unambiguously by the present ssNMR investigation, their presence would increase the strength and the number of protein contacts within the hydrogel and therefore directly impact the mesh size formed by gel contacts. For the considered sequence, docking of two β-sheets (**Fig. 6d**) creates a minimal β-unit that is characterized by inter-molecular interactions on backbone as well as side chain level. Polar contacts observed between Ser and between Asn side chains and backbone atoms resemble X-ray structures of Q/N-rich peptide-fibrils.[220] As the NQTS-rich inter FG-spacers differ in length and sequence, and probably interact in a combinatorial manner, the side chain contacts will vary considerably. Ser residues are spread widely in the sequence (**Fig. 2a**) and contribute substantially to both mobile as well as rigid segments of the hydrogel (**Fig. 1c**). Thus, the contribution of Ser to β-sheets in these NQTS-contacts most likely depends on sequential proximity to other amino acids such as Asn that reside preferentially in β-strands (**Fig. 4d**).

Gelation occurs via two distinct steps

If the identified interactions characterized the hydrogel and not just its isolated building blocks then they should correlate with gelation. Using a novel ssNMR probehead, we could simultaneously track changes in translational diffusibility of $FG/FxFG^{Nsp1p}_{2-601}$ using pulsed-field gradients (PFG) and monitor the occurrence of immobilized protein species using cross polarization (CP) experiments. **Figure 7a** displays the natural log of the proton spin-echo attenuation as a function of gradient

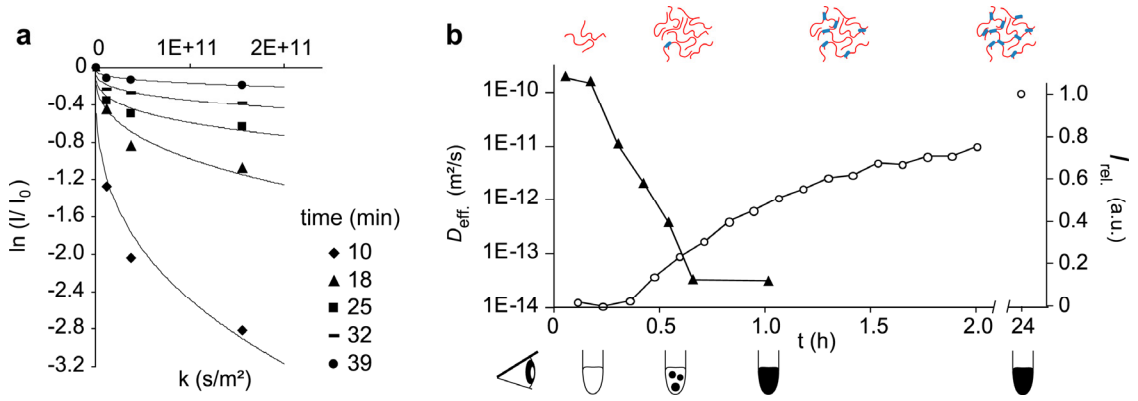

Figure 7. (***a***) Plot of the natural log of the proton spin-echo attenuation as a function of gradient strength for different time points after initiation of FG/FxFG$^{Nsp1p}_{2-601}$ gelation. (***b***) Comparison of the time-dependent decrease of the effective diffusion coefficient D_{eff} extracted from the PFG experiments (▲, logarithmic scale) and of the build-up of cross-polarization signals reflecting β-strands (○). Lines are drawn to guide the eye. The cartoon at the top illustrates the initial formation of protein clusters and the appearance of rigid β-strands. The bottom cartoon depicts formation of the gel (black) as followed by visual inspection of FG/FxFG$^{Nsp1p}_{2-601}$ (as used for NMR).

strength for different time points after initiation of FG/FxFG$^{Nsp1p}_{2-601}$ gelation (for the definition of k and experimental details see methods). Since the signal attenuation is not linear with gradient strength, FG/FxFG$^{Nsp1p}_{2-601}$ does not reside in a single folding state, but the sample most likely contains FG/FxFG$^{Nsp1p}_{2-601}$ assemblies of different sizes. In order to obtain an effective diffusion coefficient describing FG/FxFG$^{Nsp1p}_{2-601}$ self-diffusion at each time point during gelation, we fitted the data to a stretched exponential of the form $I = I_0 \exp\{(kD_{eff})^{\beta}\}$, which reflects the size distribution of the FG/FxFG$^{Nsp1p}_{2-601}$ assemblies present. Best fits to a stretched exponential decay are given as solid lines (**Fig. 7a**). The fits yield an effective self-diffusion coefficient $D_{eff.}$ for FG/FxFG$^{Nsp1p}_{2-601}$ at different time points of gelation together with an exponent β describing the width of the mass distribution of the present FG/FxFG$^{Nsp1p}_{2-601}$ clusters. The effective diffusion coefficient derived from the PFG experiments (**Fig. 7a**) decreased steeply during the first 30 minutes of gelation from a starting value of 1.7 10^{-10} m^2/s (as expected for monomeric FG/FxFG$^{Nsp1p}_{2-601}$), over almost 3 orders of magnitude (**Fig. 7b**), indicating formation of assemblies of increasing size. Interestingly, this process largely preceded the emergence of rigid β-sheet structures detected by the CP signal (**Fig. 7b**). Rigid structures became apparent only after 30 min, suggesting that decrease in diffusibility and formation of β-sheet segments are two consecutive steps during gelation. This behavior is reminiscent of the kinetic lag phase observed during amyloid formation.[221]

In conclusion, structural and kinetic ssNMR as well as mutational data suggest that both rigid hydrophilic and more dynamic hydrophobic interactions stabilize the investigated FG-hydrogel. Based on these findings, it is tempting to interpret the two observed stages of gelation as an initial hydrophobic collapse leading to high molecular weight clusters, which are subsequently stabilized by intermolecular hydrogen-bond interactions within β-sheets.

Discussion

The FG-repeat domain from Nsp1p forms an FG-hydrogel with permeability properties that resemble closely those of intact NPCs.[213] We characterized such gel for the first time by solid state NMR and found that intermolecular β-sheets between NQ-rich sequences are the most stable intragel structures. This is striking, because such interchain β-sheets are also the structural hallmark of amyloid fibrils.[220,222-224] Already in 2000, certain Nups had been recognized as N/Q-rich[219] and thereby as related to N/Q-rich amyloid-forming proteins like glutamine-extended variants of huntingtin[225] or the yeast prion Sup35p.[226] Even more recently, cellular assays revealed that several nucleoporins containing N/Q-rich domains exhibit amyloid-like characteristics *in vivo*.[227] However, the functional relevance of this parallel has remained unnoticed so far.

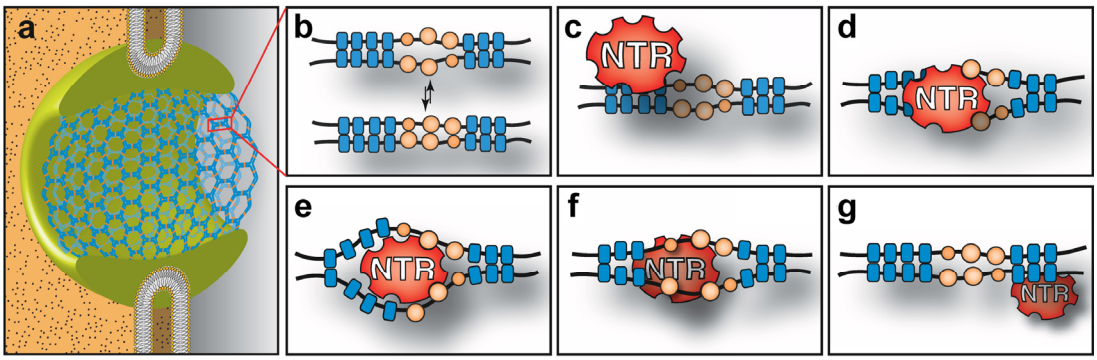

Figure 8. Illustration how an NTR might catalyze its own passage through an inter-FG repeat contact. (***a***) Schematic drawing of an NPC filled with an idealized FG-hydrogel. (***b***) FG-motif containing hydrophobic residues (orange) and vicinal residues of NQTS-rich spacers (blue) forming inter-molecular β-sheets. FG-motifs dynamically alternate between dissociated (top) and associated (bottom) states. (***c***) An NTR approaches and binds to the open state. (***d***) The binding energy is conserved by exerting strain on neighboring β-sheet elements allowing the NTR to pass (***e***). (***f***, ***g***) The mesh contact is closed by the reverse reaction.

The N/Q-rich sequences of nucleoporins are juxtaposed to FG-motifs. In contrast to previous belief, they are, however, not just functionless spacers. Instead, they engage in amyloid-like protein-protein contacts that presumably tighten the FG-hydrogel-based permeability barrier of NPCs. Such a fundamental physiological function for amyloid-type interaction is indeed remarkable, because amyloids are commonly linked to pathological conditions, such as Huntington's, Alzheimer's or Parkinson's disease and we only begin to understand their functional roles.[222] In contrast to pathological amyloids, inter FG-repeat contacts do not result in irreversible aggregates. Instead, FG-hydrogels are easily traversed by NTRs.[213]
How might this work? Key to the solution might be that inter-repeat contacts comprise two elements, namely hydrophobic interactions between FG-clusters and β-sheets between the NQTS-rich spacers. Such composite contacts appear sufficiently stable to suppress fluxes of large inert material. Thermal breathing should transiently expose mobile FG motifs and allow an approaching NTR to bind

(**Fig. 8**). Although the hydrophobic intra-gel interactions may be transient, they apparently control the association state of the β-strand segments and render them kinetically stable. This is nicely illustrated by the FG-repeat domain that lacks hydrophobic residues and also fails to form a gel (**Table 1**). Sequestering a hydrophobic FG-cluster by an NTR might therefore also open adjacent β-sheets and allow the cargo-NTR complex to pass (**Fig. 8**). Energetically, this can be seen as if the energy released by the FG-NTR interaction is spent on opening the β-sheet component of the inter-repeat contact.

Materials and Methods

E.coli expression vectors. The backbone of all plasmids used was derived from pQE80 (Qiagen, Hilden, Germany). Plasmids listed below allow for recombinant expression of indicated proteins in *Escherichia coli*.

Name	Protein name	Expressed protein	Reference
pSF345	$FG/FxFG^{Nsp1p}_{2-601}$	His_{10}-TEV-$Nsp1^{2-601}$-Cys	49
pSF654	$FSFG^{Nsp1p}_{274-601}$	His_{10}-TEV-$Nsp1^{274-601}$-Cys	This study
pSF662	$FG/FxFG^{Nsp1p}_{2-277}$	His_{10}-TEV-$Nsp1^{2-277}$-Cys	This study
pSF871	$FG/FxFG^{Nsp1p}_{2-277}$	His_{14}-TEV-$Nsp1^{2-277}$-Cys	This study
pSF872	$FG/FxFG^{Nsp1p}_{2-277}$ (T→S)	His_{14}-TEV-$Nsp1^{2-277}$(T→S)-Cys	This study
pSF873	$FG/FxFG^{Nsp1p}_{2-277}$ (N→S)	His_{14}-TEV-$Nsp1^{2-277}$(N→S)-Cys	This study
pSF921	$FG/FxFG^{Nsp1p}_{2-277}$ (FILV→S)	His_{14}-TEV-$Nsp1^{2-277}$(FILV→S)-Cys	This study
pSF902	FG^{Nsp1p}_{2-175}	His_{14}-TEV-$Nsp1^{2-175}$-Cys	This study

Abbreviations: His_{10}, His_{14}: histidine tag; TEV: TEV-protease recognition site. Encoded amino acids and introduced mutations are indicated. Residue numbers correspond to full length Nsp1p. All constructs contain an N-terminal His-tag followed by a TEV-protease recognition and an engineered cysteine at the C-terminus.

Expression, purification and labeling of FG-repeat proteins and mutants. N-terminally His-tagged proteins were expressed and purified as described for $FG/FxFG^{Nsp1p}_{2-601}$.[49] To obtain ^{13}C-labeled, ^{15}N-labeled and ^{13}C,^{15}N-double labeled proteins, protein expression was performed in isotope-labeled rich growth medium (Silantes, Mering, Germany).

Preparation of FG-repeat hydrogels for gelation- and ssNMR analyses. Starting point for gelation were salt- and solvent-free preparations of repeat domains. For that, the nickel-eluted protein was applied to a reversed-phase HPLC column, eluted in an acetonitrile gradient in 0.1 % TFA, and lyophilized. For qualitative gelation analyses, lyophilized proteins were dissolved at a concentration of 200 mg/ml in 0.1% TFA (in water), followed by quick neutralization with Tris-Base or Tris-HCl pH 8.5. Final preparations contained 160 mg/ml protein and 200 mM Tris at neutral pH.

For ssNMR experiments, lyophilized proteins were dissolved at a concentration of 200 mg/ml in 0.1 % TFA (in water or D_2O) and immediately neutralized by addition of Na_2HPO_4 (1M in H_2O) or Na_2DPO_4 (stock solution 1M in D_2O). Final preparations contained 160 mg/ml protein, 200 mM Na_2HPO_4 or Na_2DPO_4 and displayed a pH of 6.5-7.0.

Solid-state nuclear magnetic resonance. We conducted NMR experiments using 4 mm triple-resonance (^1H,^{13}C,^{15}N) probeheads at static magnetic fields of 11.7 T, 16.4 T, 18.8 T, and 20.1 T corresponding to 500 MHz, 700MHz, 800 MHz, and 850 MHz proton resonance frequencies (Bruker Biospin). A triple-resonance probe with z-gradient was available for the 18.8 T setup. The gradient strength was calibrated by measuring self-diffusion of water at 293 K. A stimulated echo sequence with sine-shaped bipolar gradient pulses was used, the diffusion time was 50 ms and the length of gradient pulses was 1 ms. An effective gradient strength at 10 A of 0.398 T/m was determined.
Through-space transfer experiments were performed at 8 kHz magic angle spinning and 283 K. Typical proton field strengths for 90° pulses and SPINAL64[77] decoupling ranged between 70 and 83 kHz. (^{13}C, ^{13}C) correlation spectra (e.g. **Fig. 1a**) were obtained using conventional proton-driven spin diffusion schemes employing mixing times between 20 and 300 ms.
1D NHHC experiments[30] summarized in **Figure 5** were performed for variable (^1H, ^1H) mixing time. Short contact times of t_{HN} = 150 µs and t_{HC} = 80 µs enclosing the (^1H, ^1H) mixing ensured cross-polarization transfer for directly bonded spin-pairs only. The 1D NHHC experiments performed for the sample containing a 1:1 mixture of ^{13}C-labeled and ^{15}N-labeled $FG/FxFG^{Nsp1p}_{2-277}$ (**Fig. 5b**) employed a short (^1H, ^1H) mixing time of 125 µs in order to probe short inter-strand distances. CP contact times enclosing the (^1H, ^1H) mixing were t_{HN} = 400 µs and t_{HC} = 200 µs. We note that additional 1D NHHC control experiments confirmed that signal intensities in **Figure 5b** did not result from insufficient suppression of direct ^{13}C signal intensities. For example, no ^{13}C signal was detected if power levels for the ^1H-^{15}N cross polarization step were set to zero.
(^1H, ^{13}C) heteronuclear correlation experiments (**Fig. 4a**) were acquired using frequency-switched Lee-Goldburg proton decoupling.[106,228]
NOESY experiments[42] (e.g. **Fig. 3**) at various (^1H, ^1H) mixing times were performed to probe through-space proximity in highly mobile protein segments.
Through-bond transfer experiments were performed at 5 kHz magic angle spinning and 293 K. (^{13}C, ^{13}C) and (^1H, ^{13}C) correlations spectra (**Fig. 1b**) were obtained using an INEPT-TOBSY scheme.[40] A TOBSY mixing time of 6.5 ms and 10 kHz GARP[229] decoupling were employed.
Pulsed-field gradient (PFG) experiments (**Fig. 7**) were performed at 5 kHz magic angle spinning and about 293 K using a 13-interval pulse sequence[43] employing sine-shaped bipolar gradient pulses of 5 ms duration. The diffusion time was 200 ms and a longitudinal eddy current delay of 5 ms was used. The signal attenuation obtained at different gradient strengths (5, 23, 41, and 83 %) at different time points during gelation did not show a linear dependency expected for one freely diffusing species (**Fig. 7a**). In order to obtain an effective diffusion coefficient, we assumed diffusion of an aggregate distribution and fitted the data to

a stretched exponential of the form $I = I_0 \exp\{(kD_{eff})^{\beta}\}$.[230] Here I and I_0 are the integrals of the Hα region in the presence and absence (5 %) of the z-gradient. $k = 4\gamma^2 x^2 \delta^2 [\Delta - (\delta - d)/2 - \delta/8]$ contains experimental parameters and constants. γ: ^{1}H gyromagnetic ratio, x: gradient strength, δ: gradient pulse length, Δ: diffusion time, d: time delay between gradient pulses). D_{eff} is the effective diffusion coefficient and β describes the width of the mass distribution of diffusing species.

Relative Cα-Cβ peak intensities per residue as reported in **Figure 1c** were computed according to

$$I_{rel}^{aa} = \frac{I_{C\alpha-C\beta}^{aa}}{n^{aa}} \Big/ \frac{I_{C\alpha-C\beta}^{aa}}{n^{aa}}\Bigg|_{\max} .$$

By dividing the integral of the Cα-Cβ (Cα-Cβ/γ for Gln) crosspeak ($I_{C\alpha-C\beta}^{aa}$) by the number of the respective amino acid (n^{aa}) in the sequence, we obtained the peak intensity per residue. Normalization against the maximum peak intensity per residues yields the relative Cα-Cβ peak intensities per residue (I_{rel}^{aa}). Peak integrals were obtained using the software Topspin 2.1 (Bruker Biospin).

Structural models for β-sheets formed by NQTS-rich spacers. An extended strand input file for a typical NQTS-rich spacer comprising residues 18 to 25 of Nsp1p (marked red in **Fig. 6a**) was generated using Pymol (DeLano Scientific). The molecular dynamic (MD) based docking of four FG_{18-25}^{Nsp1p} peptides was performed with HADDOCK[107] using standard settings. To treat the peptide as a fragment of a longer polypeptide chain, we assumed that N- and C-termini were uncharged. All residues were defined as active interaction surface. First, two peptides were docked resulting in two-stranded β-sheets. Docking results were clustered and sorted by HADDOCK score. Parallel and antiparallel orientation of the peptides occurred with similar likelihood and similar total energies. The lowest energy model obtained in this docking step is shown in **Figure 6b** and hydrogen bonds stabilizing this β-sheet on the backbone level are illustrated in **Figure 6c**. Hydrogen bonds are indicated by dashed lines in both figures. The structural model presented in **Figure 6D** represents the lowest energy structure obtained by a HADDOCK docking of two β-sheet units proceeding as described above.

Chapter 8

Summary / Samenvatting

Christian Ader

Bijvoet Center for Biomolecular Research, Utrecht University, The Netherlands

Summary

Membranes border cells from their environment. Thus, they belong to the basic prerequisites for life as we know it. Within cells, membranes are used to establish compartments dedicated to specific tasks such as providing local proximity of components, assembling specialized molecular machinery and confining their numerous functions to salutary consistency. Biological membranes are functionalized by associated proteins which account for a large fraction of all proteins encoded by the genome. Solid-state NMR (ssNMR) spectroscopy is a prime technique to investigate structure and dynamics of membrane proteins at atomic resolution (**Chapter 1**). This thesis reports on progress made in ssNMR methodology, sample preparation, and data analysis enabling the study of two diverse proteins involved in selective membrane transport. First, ssNMR spectroscopy was used in close reverence to functional data to study structure-function relations of the chimeric potassium (K^+) channel KcsA-Kv1.3 derived from the prokaryotic KcsA channel from *Streptomyces lividans*. The results provide detailed insight into structure and dynamics of K^+ channel activation and inactivation gating and reveal modulating effects of ligands, ions, and the lipidic environment on the functionally relevant conformations of the K^+ channel. Second, functional hydrogels formed by FG-repeat domains of the yeast nucleoporin Nsp1p were characterized by ssNMR. These polypeptides are part of the nuclear pore complex controlling all molecular trafficking between nucleus and cytoplasm in eukaryotic cells. The acquired data provide structural details of FG-hydrogels as well as their gelation kinetics and link amyloid-like protein-protein interactions to the selectivity barrier of the nuclear pore complex.

The topology of membrane proteins with respect to the lipid bilayer is a global structural parameter which is often difficult to obtain experimentally, but may contain valuable information for the functional interpretation of protein structure or structural rearrangements associated with ligand binding or signal transduction. **Chapter 2** describes the use of water-edited ssNMR spectroscopy to probe the topology of membrane embedded proteins. The general notion of these experiments is that magnetization transferred from selectively excited water to the protein over time reports on solvent exposure and accessibility of the membrane protein. We show for a series of α-helical transmembrane proteins that transfer efficiencies are comparable in these systems and that magnetization transfer can be described by a diffusion model linking the initial rate for water-protein magnetization transfer to the ratio between the protein volume und the water-accessible protein surface. This relationship provided an experimental way to monitor structural rearrangement of the chimeric K^+ channel KcsA-Kv1.3 as response to pH-induced gating. Additionally, the water-accessible surface of the protein could be investigated with residue-specific resolution by extending water-edited spectroscopy to multidimensional correlation spectra. In the future this technique should prove useful for structure-function studies of other membrane proteins like ligand activated ion channels or catalytically active outer membrane proteins. Also, the structural organization of insoluble protein assemblies like amyloid fibrils could be estimated from water-edited ssNMR spectroscopy.

KcsA and also the chimeric mutant KcsA-Kv1.3 can be activated by changing the pH from neutral to pH 4.0 on its intracellular site. Shortly after activation, the measured K^+ current in patch clamp experiments elapses and the channel enters into an inactivated state. These conductive and non-conductive states are fundamental to the gating cycle of ion channels ensuring electric excitability of cells like neurons. For KcsA the inactivation process is called C-type inactivation and it is intrinsic to the pore domain of the channel. Therefore, this type of inactivation is based on a rearrangement of the channel that is fundamentally different from N-type inactivation where N-terminal ball peptides physically block the ion permeation pathway. **Chapter 3** reports chemical shift changes observed for KcsA-Kv1.3 in asolectin liposomes at pH 7.5 and pH 4.0. They reveal two distinct regions, named gates, in the pore domain of the potassium channel that exhibit structural changes upon pH induced gating. Dependence of the Cα and Cβ chemical shifts on the dihedral angles Φ and Ψ allowed us to approximate nature and magnitude of the structural rearrangements within the gates upon channel activation and inactivation. Our data suggest that activation gating is related to the bending of transmembrane helices that close the ion permeation pathway in KcsA crystal structures obtained at neutral pH. This rearrangement is in agreement with previous EPR data, crystal structures of other K^+ channels as well as the water-edited ssNMR data introduced in Chapter 2. Inactivation gating on the other hand is related to transition from a conductive to a collapsed conformation of the selectivity filter. This unique structure entails the potassium selectivity and specificity of the channel. Crystal structures obtained by the group of Roderick MacKinnon revealed that its conformation is potassium sensitive. Using ssNMR we could now link these structures to the functionally relevant states of the channel's inactivation gate.

Due to the pharmacological significance of potassium channels, their interactions with synthetic ligands are of considerable interest. Derivatives of tetraphenylporphyrines represent a recent class of compounds that strongly affect channel gating. For a representative porphyrin ligand, binding to KcsA-Kv1.3 was shown to occur with nanomolar affinity. In addition, porphyrin is able to compete with the scorpion toxin KTX for binding to the channel. **Chapter 3** provides a conformational analysis of porphyrin bound KcsA-Kv1.3 revealing that the ligand similar to channel inactivation induces a collapsed conformation of the selectivity filter. Comparison to previous results obtained for the KTX bound channel shows that ligands binding to a similar site at the potassium channel can induce and stabilize distinct conformations. We used the ssNMR data to conduct a molecular dynamics driven *in silico* protein-ligand docking. In agreement with the KcsA crystal structures obtained at high and low concentration of K^+, the resulting binding mode suggests that filter collapse is linked to a locally limited K^+ concentration.

Detailed analyses of ^{13}C chemical shifts were used to characterize structural changes of KcsA-Kv1.3 related to channel gating as well as ligand binding. The results epitomize general, ssNMR-based, studies examining local structural rearrangements of membrane proteins in a bilayers setting and establish conformational details of the channel's gating cycle. This information provided the fundamental basis for more comprehensive studies of channel gating discussed in the following chapters.

Chapter 4 summarizes the impact of the permeant ion, K^+, on gating states of the KcsA-Kv1.3 K^+ channel. We found, using ssNMR, that the resting state of KcsA-Kv1.3 in asolectin liposomes can be stabilized at pH 4.0 over the inactivated state if the potassium concentration exceeds ~10 mM. This finding was complemented by electrophysiological studies that detected distinct potassium binding events affecting channel inactivation. By combining ssNMR titration experiments performed with proteoliposomal preparations of KcsA-Kv1.3 with the distinct effects of the ligands described in Chapter 3, we identified side chains located in the two gates of the channel forming part of an interaction surface that couples activation and inactivation gate. On this basis, we suggest that K^+ stabilizes the conductive conformation of the selectivity filter via the intrinsic K^+ binding sites. The conductive filter conformation then stabilizes the helices responsible for activation gating in a straight conformation resulting in a closed channel in its resting state. Furthermore, the availability of a resting channel even at pH 4.0 allowed us to spectroscopically characterize protonation states of glutamate residues that were suggested to be crucial for pH sensing and initializing the gating cycle of KcsA. Indeed, we could confirm that protonation of Glu118 and Glu120 correlates with activation gate opening as seen by chemical shift analysis and water-edited spectroscopy. Protonation of these residues leads to an excess of positive charges at the helix bundle crossing. The bending of transmembrane helices resulting in an activated K^+ channel should, therefore, be induced by electrostatic repulsion of these charged residues as proposed previously based on mutational studies.

The lipidic environment can strongly influence membrane protein structure and function on different structural levels, ranging from specific lipid-protein binding sites to indirect lipid effects, for example based on the membrane lateral pressure. **Chapter 5** describes data dissecting structural stability of tetrameric KcsA-Kv1.3 and its gating states as a function of the lipid setting. We followed tetramer dissociation induced by increasing concentrations of trifluoroethanol by ssNMR in a site resolved manner. Comparison of the results with biochemical data suggested that the molecular nature of individual lipids bound to the non-annular lipid binding site of KcsA changes the stability of the K^+ channel tetramer. Moreover, we found that phosphatidic acid as well as phosphatidylethanolamin in conjunction with potassium ions stabilized the resting state of KcsA-Kv1.3 at pH 4.0. These results revealed that physical parameters of the lipid bilayer such as lipid intrinsic curvature or even hydrophobic mismatch might affect the states of the K^+ channel's gating cycle in addition to non-annular binding. The study introduces a novel framework to study such lipid effects by ssNMR spectroscopy.

Protein dynamics play an essential role for molecular recognition and protein function. Considering ion channels, especially local mobility within the selectivity filter is of particular interest. As the filter has to bind and release K^+ at a fast rate and, at the same time, has the potential to alternate between conductive and collapsed conformations, assessment of its local dynamics under defined, native like conditions is of great significance. **Chapter 6** describes the use of residue-specific ^{15}N longitudinal relaxation rates as a probe to study mobility of the membrane embedded KcsA-Kv1.3 channel by ssNMR. We observed increased

local mobility for two widely conserved glycine residues within the selectivity filter. These distinct dynamics might be related to ion occupancy and play a crucial role for structural adaptation related to ion permeation and the transition of the filter between its conductive and collapsed conformation during its gating cycle. In summary, we show that T_1 relaxation rates as obtained for KcsA-Kv1.3 reconstituted in lipid bilayers provide a favorable means to follow site specific dynamics in larger membrane embedded proteins. In the particular case of K^+ channels, this framework may be used in the future to study the dynamical details associated with ion and ligand binding or channel inactivation.

FG-repeat domains are essential building blocks of the permeability barrier of nuclear pore complexes (NPCs) controlling all nucleo-cytoplasmic exchange. They allow free passage of small molecules, but suppress the flux of macromolecules larger than 30 kDa and thereby prevent an uncontrolled intermixing of nuclear and cytoplasmic contents. However, the permeability barrier also permits a rapid passage of even large cargoes, provided these are bound to appropriate nuclear transport receptors (NTRs). These fundamental properties are well reproduced by hydrogels formed by isolated FG-domains providing an in vitro model for nuclear transport. While it has been reported that FG-domains bind NTRs, their constitutive protein-protein interactions suppressing passive flux and yet establishing selective permeability are unknown. In **Chapter 7** we describe the use of ssNMR spectroscopy for the investigation of such hydrogels. We showed that transient hydrophobic interactions as well as intermolecular β-sheets between Asn-rich spacer regions stabilize the selective hydrogel formed by the 62 kDa FG/FxFG repeat domain of the yeast nuclear pore complex protein Nsp1p. The latter interactions also characterize neuronal inclusions or prions formed by Asn/Gln-rich amyloid proteins. This points towards a fully unexpected physiological function of such inter-chain β-structures. Time-resolved solid-state NMR and mutational data suggest that β-sheet formation depends on the hydrophobic interactions also crucial for NTR binding. This interdependence provides a plausible explanation for how contacts between FG-repeats gain the kinetic stability to suppress passive fluxes through nuclear pores and yet allow rapid NTR passage.
Hydrogels define a unique state of certain proteins. This study provided the first detailed structural and dynamical characterization of a protein hydrogel. Additionally, combination of cross-polarization experiments and pulsed-field gradients represents a novel approach to study gelation in a time-resolved manner. The presented techniques should be beneficial for the analysis of natural and synthetic protein hydrogels and the insights obtained might help to design peptides that form functional hydrogels for technological and pharmaceutical use.

Samenvatting

Membranen schermen cellen af van hun omgeving. Ze behoren dus tot de basisvoorwaarden voor het leven zoals wij dat kennen. Binnen cellen worden membranen gebruikt om compartimenten te maken die toegewijd zijn aan specifieke taken zoals het verschaffen van plaatselijke nabijheid van componenten, het samenvoegen van gespecialiseerde moleculaire machinerie en het beperken van hun talloze functies tot een productieve samenhang. Biologische membranen worden functioneel door geassocieerde eiwitten die een groot deel vormen van alle eiwitten die geëncodeerd worden door het genoom. Vaste stof NMR (ssNMR) spectroscopie is een voorname techniek om de structuur en dynamiek van membraaneiwitten met atomaire resolutie te bestuderen (**Hoofdstuk 1**). Dit proefschrift rapporteert over vooruitgangen gemaakt in ssNMR methodologie, monsterbereiding en data-analyse, wat de bestudering van twee verschillende eiwitten betrokken bij selectief membraantransport mogelijk maakte. Ten eerste is ssNMR in nauwe samenhang met functionele gegevens toegepast om structuur-functie relaties te bestuderen van het chimaere kalium (K^+)-kanaal KcsA-Kv1.3, dat is afgeleid van het prokaryote KcsA-kanaal uit *Streptomyces lividans*. De resultaten geven gedetailleerd inzicht in de structuur en dynamica van de activerings- en deactiveringsgating van het K^+-kanaal en onthullen modulerende effecten van liganden, ionen en de lipide-omgeving op de functioneel relevante conformaties van het K^+-kanaal. Ten tweede werden met behulp van ssNMR functionele hydrogels, gevormd door FG-repeat domeinen van het gist nucleosporine Nsp1p, gekarakteriseerd. Deze polypeptiden zijn onderdeel van het nucleaire poriecomplex dat al het moleculaire verkeer tussen celkern en cytoplasma in eukaryote cellen controleert. Naast de kinetiek van hun gelvorming verschaffen de verkregen resultaten details van hydrogelstructuren en verbinden ze amyloïd-achtige eiwit-eiwit interacties met de selectiviteitbarrière van het poriecomplex van de celkern.

De topologie van membraaneiwitten ten opzichte van de lipide bilaag is een algemene structurele parameter die vaak moeilijk experimenteel te bepalen is, maar waardevolle informatie kan bevatten voor de functionele interpretatie van een eiwit structuur of een structurele reorganisatie ten gevolge van ligand-binding of signaal transductie. **Hoofdstuk 2** beschrijft het gebruik van water-edited ssNMR spectroscopie om de topologie van membraan-geïnserteerde eiwitten te toetsen. De algemene gedachte achter deze experimenten is dat magnetisatie die in de tijd overgebracht wordt van selectief aangeslagen water naar het eiwit, informatie verschaft over blootstelling aan het oplosmiddel en de toegankelijkheid van het membraaneiwit. We tonen voor een serie α-helische transmembraaneiwitten dat de overdrachtsefficiënties in deze systemen vergelijkbaar zijn en dat magnetisatieoverdracht beschreven kan worden door een diffusiemodel dat de initiële snelheid van water-eiwit magnetisatieoverdracht koppelt aan de verhouding tussen het eiwitvolume en het water-toegankelijke eiwitoppervlak. Deze relatie leverde een experimentele wijze om de structurele reorganisatie van het chimaere K^+-kanaal KcsA-Kv1.3 te volgen als respons op pH-geïnduceerde gating. Daarnaast kon het water-toegankelijke eiwit oppervlak worden bestudeerd met residue-specifieke resolutie door water-edited spectroscopie uit te breiden naar

multidimensionale correlatie-spectra. In de toekomst zou deze techniek bruikbaar moeten blijken voor structuur-functie studies aan andere membraaneiwitten zoals ligand-geactiveerde ion-kanalen of katalytisch actieve buitenmembraan eiwitten. Tevens zou de structurele organisatie van onoplosbare multimeren zoals amyloïd-fibrillen met water-edited ssNMR spectroscopie benaderd kunnen worden.

KcsA en zijn chimaere mutant KcsA-Kv1.3 kunnen geactiveerd worden door aan de intracellulaire kant de pH van neutraal tot pH 4.0 te veranderen. Uit "patch clamp"-experimenten blijkt dat kort na de activering de gemeten K^+-stroom verdwijnt en het kanaal komt in een ongeactiveerde toestand. Deze geleidende en niet-geleidende toestanden zijn fundamenteel voor de gating-cyclus van ion-kanalen doordat ze de gevoeligheid voor elektrische prikkeling van cellen zoals neuronen waarborgen. Voor KcsA wordt het inactiveringsproces een C-type inactivering genoemd en het is gelokaliseerd op het poriedomein van het kanaal. Dit type inactivering is gebaseerd op de reorganisatie van het kanaal en dit is fundamenteel anders dan de N-type inactivering waar N-terminale "ball peptides" de ionen-stromingsweg fysiek blokkeren. **Hoofdstuk 3** rapporteert over chemical shift veranderingen geobserveerd voor KcsA-Kv1.3 in asolectine liposomen bij pH 7.5 en pH 4.0. Deze duiden op twee verschillende gebieden in het poriedomein van het kaliumkanaal, gates genaamd, die structuurveranderingen ondergaan na pH-geïnduceerde gating. De afhankelijkheid van de Cα en Cβ chemical shifts van de dihedrale hoeken ϕ en ψ stond ons toe om de aard en grootte van de structurele reorganisaties in de gates als gevolg van kanaalactivering en -deactivering te benaderen. Onze data suggereren dat activeringsgating is gekoppeld aan de buiging van transmembraanhelices, hetgeen de ion-stromingsweg blijkt te sluiten in KcsA kristalstructuren verkregen bij neutrale pH. Deze reorganisatie komt overeen met bestaande EPR data, kristalstructuren van andere K^+-kanalen, en de water-edited ssNMR data die geïntroduceerd werden in Hoofdstuk 2. Aan de andere kant, inactiveringsgating is gerelateerd aan de overgang van een conductieve naar een verstoorde conformatie van de selectiviteitfilter. Deze unieke structuur is verantwoordelijk voor de kaliumselectiviteit en -specificiteit van het kanaal. Kristalstructuren verkregen door de groep van Roderick MacKinnon toonden aan dat deze conformatie kaliumgevoelig is. Met behulp van ssNMR konden we nu deze structuren aan de functioneel relevante toestanden van de inactiveringsgate van het kanaal koppelen.
Door het farmacologisch belang van kaliumkanalen zijn hun interacties met synthetische liganden van aanzienlijke interesse. Afgeleiden van tetrafenylporfyrines vertegenwoordigen een nieuwe klasse van verbindingen die sterk de kanaalgating beïnvloeden. Voor een representatief porfyrine-ligand was aangetoond dat KcsA-Kv1.3 binding optreedt met nanomolaire affiniteit. Daarnaast is porfyrine in staat met het schorpioen toxine KTX te concurreren voor binding aan het kanaal. **Hoofdstuk 3** geeft een conformationele analyse van porfyrine-gebonden KcsA-Kv1.3, die aantoont dat het ligand, net als kanaaldeactivering, een verstoorde conformatie van de selectiviteitfilter induceert. Vergelijking met voorgaande resultaten verkregen voor het KTX-gebonden kanaal laat zien dat liganden die op dezelfde positie op het kaliumkanaal binden verschillende conformaties kunnen induceren en stabiliseren. We gebruikten ssNMR om een door moleculaire dynamica gedreven in silico eiwit-ligand docking te sturen. In

overeenstemming met de KcsA kristalstructuren verkregen bij hoge en lage kalium-concentratie suggereert de resulterende bindingswijze dat de verstoring van de filter gekoppeld is aan een plaatselijk gelimiteerde K^+- concentratie.
Gedetailleerde analyses van ^{13}C chemical shifts werden gebruikt om structuurveranderingen van KcsA-Kv1.3 te karakteriseren ten gevolge van kanaal-gating en ligand-binding. De resultaten vertegenwoordigen algemene, op ssNMR gebaseerde studies, die plaatselijke structuurveranderingen van membraaneiwitten in een bilaag-omgeving onderzoeken, en leggen conformationele details van de gating-cyclus van het kanaal bloot. Deze informatie leverde de fundamentele basis voor de uitgebreidere studies van kanaal-gating die bediscussieerd worden in de volgende hoofdstukken.

Hoofdstuk 4 vat de invloed van het permeante ion, K^+, op de gating-toestanden van het KcsA-Kv1.3 kanaal samen. Met ssNMR vonden we dat de rusttoestand van KcsA-Kv1.3 in asolectine liposomen gestabiliseerd kan worden bij pH 4.0, ten nadele van de inactieve toestand, wanneer de kaliumconcentratie ~10mM overschrijdt. Deze vondst werd gecomplementeerd door elektrofysiologische studies die typische kaliumbindingsgebeurtenissen aangeven die kanaal-inactivering beïnvloedden. Door ssNMR titratie-experimenten, uitgevoerd met proteoliposomale KcsA-Kv1.3 preparaten, te combineren met de verschillende effecten van de liganden beschreven in Hoofdstuk 3, hebben we in de twee gates van het kanaal zijketens geïdentificeerd die onderdeel vormen van een interactieoppervlak dat de activatie- aan de inactivatie-gate koppelt. Op basis van dit suggereren we dat K^+ de conductieve conformatie van de selectiviteitfilter stabiliseert via de interne K^+-bindingsplekken. Vervolgens stabiliseert de conformatie van de geleidingsfilter de helices die verantwoordelijk zijn voor activeringsgating in een rechte conformatie, hetgeen resulteert in een gesloten kanaal in zijn rusttoestand. De beschikbaarheid van een kanaal dat zelfs bij pH 4.0 in rust verkeert, stond ons daarna toe om de protoneringstoestanden van glutamaat-residuen, waarvan gesuggereerd wordt dat ze cruciaal zijn voor de pH-perceptie en het initialiseren van de gating-cyclus van KcsA, spectroscopisch te karakteriseren. We konden na chemical shift analyse en water-edited spectroscopie bevestigen dat protonering van Glu118 en Glu120 correleert met de opening van de activerings-gate. Protonering van deze residuen leidt tot een overmaat aan positieve lading bij de helix-bundel kruising. Het buigen van transmembraanhelices dat resulteert in een geactiveerd K^+-kanaal zou derhalve geïnduceerd moeten worden door de elektrostatische afstoting van deze geladen residuen, hetgeen voorheen reeds voorgesteld werd op grond van mutationele studies.

De lipide-omgeving kan de structuur en functie van een membraaneiwit sterk beïnvloeden op verschillende structurele niveaus, variërend van specifieke lipide-eiwit bindingsplekken tot indirecte lipide-effecten, bijvoorbeeld gebaseerd op de zijwaartse druk in het membraan. **Hoofdstuk 5** beschrijft data die de structurele stabiliteit van tetrameer KcsA-Kv1.3 en zijn gatings-toestanden als functie van het lipide-systeem ontleedt. Met ssNMR volgden we de tetrameer dissociatie die geïnduceerd werd door toenemende concentraties trifluorethanol op een positie-specifieke wijze. Vergelijking van de resultaten met biochemische data suggereerde dat de moleculaire aard van individuele lipiden gebonden aan de niet-annulaire

lipide-bindingspositie van KcsA de stabiliteit van het K^+-kanaal tetrameer verandert. Bovendien vonden we dat zowel 1,2-diacylglycerol 3-fosfaat als fosfatidyl-ethanolamine in samenwerking met kalium-ionen de rusttoestand van KcsA-Kv1.3 bij pH 4.0 stabiliseerde. Deze resultaten toonden aan dat algemene fysische parameters van de lipide bilaag, zoals membraankromming, de toestanden van de K^+-kanaalgatingstoestanden zouden kunnen beïnvloeden. De studie introduceert een nieuw kader om zulke lipide-effecten te kunnen bestuderen met ssNMR.

Eiwit-dynamica speelt een essentiële rol in moleculaire herkenning en eiwit functie. Met betrekking tot ion-kanalen is in het bijzonder de lokale mobiliteit in de selectiviteitfilter interessant. Omdat het filter K^+ met hoge snelheid moet binden en vrijlaten, en tegelijkertijd de potentie heeft om tussen geleidende en verstoorde conformaties te schakelen, is de bepaling van zijn lokale dynamica bij gedefinieerde, natuurlijke condities van groot belang. **Hoofdstuk 6** beschrijft het gebruik van residue-specifieke ^{15}N-longitudinale relaxatiesnelheden als een manier om de mobiliteit van het membraan-geïnserteerde KcsA-Kv1.3 kanaal met ssNMR te bestuderen. We observeerden toegenomen plaatselijke mobiliteit voor twee sterk geconserveerde glycine-residuen in de selectiviteitfilter. Deze typische dynamica zou gerelateerd kunnen zijn aan de ion-bezetting en een cruciale rol kunnen spelen bij de structurele aanpassing gekoppeld aan de ionendoorlaatbaarheid en de overgang van de filter tussen zijn conductieve en verstoorde conformatie tijdens zijn gating-cyclus. Samenvattend, we laten zien dat T_1 relaxatie-snelheden, zoals verkregen voor KcsA-Kv1.3 gereconstitueerd in lipide-bilagen, een gunstige methode vormen om positie-specifieke dynamica in grotere membraan-geïnserteerde eiwitten te volgen. In het geval van K^+-kanalen kan deze methode in de toekomst gebruikt worden om de details van de dynamica met betrekking tot ion- en ligand-binding of kanaal-inactivering te bestuderen.

FG-repeat domeinen zijn essentiële bouwstenen van de permeabiliteitbarrière van nucleaire porie-complexen (NPCs) die alle nucleo-cytoplasmatische uitwisseling controleren. Ze staan vrije doorgang van kleine moleculen toe, maar onderdrukken de doorstroom van macromoleculen groter dan 30 kDa en voorkomen daarbij een ongecontroleerde vermenging van de inhoud van de celkern en het cytoplasma. Echter, de permeabiliteitbarrière staat zelfs de snelle doorvoer van grote deeltjes toe, met als voorwaarde dat ze gebonden zijn aan de juiste nucleaire transport receptoren (NTRs). Deze fundamentele eigenschappen worden goed nagebootst door hydrogels gevormd door geïsoleerde FG-domeinen wat een in vitro model levert voor nucleair transport. Terwijl gerapporteerd is dat FG-domeinen aan NTRs binden, zijn de onderliggende eiwit-eiwit interacties die de passieve flux onderdrukken en tegelijkertijd de selectieve permeabiliteit bepalen, onbekend. In **Hoofdstuk 7** beschrijven we het gebruik van ssNMR spectroscopie om zulke hydrogels te onderzoeken. We toonden aan dat naast tijdelijke hydrofobe interacties ook inter-moleculaire β-sheets tussen Asn-rijke gebieden de selectieve hydrogel stabiliseren die gevormd wordt door het 62 kDa FG/FxFG-repeat domein van het gist NPC-eiwit Nsp1p. De laatstgenoemde interacties karakteriseren ook neuronale inclusies van prionen gevormd door Asn/Gln-rijke amyloïd-eiwitten. Dit wijst op een volledig onverwachte fysiologische functie voor zulke inter-keten β-

structuren. SsNMR als functie van de tijd en mutatie-data suggereren dat β-sheet vorming afhangt van de hydrofobe interacties die ook cruciaal zijn voor NTR-binding. Deze onderlinge afhankelijkheid levert een aannemelijke verklaring voor hoe contacten tussen FG-repeats de kinetische stabiliteit veroorzaken om passieve stroming door nucleaire poriën te onderdrukken en toch een snelle NTR-passage toe te staan.

Hydrogels definiëren een unieke toestand van bepaalde eiwitten. Deze studie leverde de eerste gedetailleerde structuur- en dynamica-karakterisering van een eiwit-hydrogel. Bovendien vormt de combinatie van cross-polarisatie experimenten en pulsed-field gradiënten een nieuwe benadering om gelatinering te bestuderen in de tijd. De gepresenteerde technieken zouden nuttig kunnen zijn voor de analyse van natuurlijke en synthetische eiwit-hydrogels, en de verkregen inzichten kunnen bijdragen aan het ontwerpen van peptiden die functionele hydrogels kunnen vormen voor technologisch en farmaceutisch gebruik.

Bibliography

1. Berman, H.M. et al. The Protein Data Bank. *Nucl. Acids Res.* **28**, 235-242 (2000).
2. Wallin, E. & van Heijne, G. Genome-wide analysis of integral membrane proteins from eubacterial, archaean, and eukaryotic organisms. *Protein Sci.* **7**, 1029-1038 (1998).
3. Yildirim, M.A., Goh, K.-I., Cusick, M.E., Barabasi, A.-L. & Vidal, M. Drug-target network. *Nat. Biotech.* **25**, 1119-1126 (2007).
4. Warschawski, D. (http://www.drorlist.com/nmr/MPNMR.html).
5. White, S. (http://blanco.biomol.uci.edu/Membrane_Proteins_xtal.html).
6. Andrew, E.R., Bradbury, A. & Eades, R.G. Removal of Dipolar Broadening of Nuclear Magnetic Resonance Spectra of Solids by Specimen Rotation. *Nature* **183**, 1802-1803 (1959).
7. Lowe, I.J. Free Induction Decays of Rotating Solids. *Phys. Rev. Lett.* **2**, 285 (1959).
8. Junge, F. et al. Large-scale production of functional membrane proteins. *Cell. Mol. Life Sci.(CMLS)* **65**, 1729-1755 (2008).
9. Etzkorn, M. et al. Secondary structure, dynamics, and topology of a seven-helix receptor in native membranes, studied by solid-state NMR spectroscopy. *Angew. Chem. Int. Ed.* **46**, 459-462 (2007).
10. Schneider, R. et al. Solid-State NMR Spectroscopy Applied to a Chimeric Potassium Channel in Lipid Bilayers. *J. Am. Chem. Soc.* **130**, 7427-7435 (2008).
11. Seidel, K. et al. Structural characterization of Ca^{2+}-ATPase-bound phospholarnban in lipid bilayers by solid-state nuclear magnetic resonance (NMR) Spectroscopy. *Biochemistry* **47**, 4369-4376 (2008).
12. Cortes, D.M. & Perozo, E. Structural Dynamics of the Streptomyces lividans K^+ Channel (SKC1): Oligomeric Stoichiometry and Stability. *Biochemistry* **36**, 10343-10352 (1997).
13. Lange, A. et al. Toxin-induced conformational changes in a potassium channel revealed by solid-state NMR. *Nature* **440**, 959-962 (2006).
14. Legros, C. et al. Generating a High Affinity Scorpion Toxin Receptor in KcsA-Kv1.3 Chimeric Potassium Channels. *J. Biol. Chem.* **275**, 16918-16924 (2000).
15. Herzfeld, J. & Lansing, J.C. Magnetic resonance studies of the bacteriorhodopsin pump cycle. *Annu. Rev. Biophys. Biomol. Struct.* **31**, 73-95 (2002).
16. Opella, S.J. & Marassi, F.M. Structure Determination of Membrane Proteins by NMR Spectroscopy. *Chem. Rev.* **104**, 3587-3606 (2004).
17. Pines, A., Gibby, M.G. & Waugh, J.S. Proton-Enhanced Nuclear Induction Spectroscopy. A Method for High Resolution NMR of Dilute Spins in Solids. *J. Chem. Phys.* **56**, 1776-1777 (1972).
18. Hartmann, S.R. & Hahn, E.L. Nuclear Double Resonance in the Rotating Frame. *Phys. Rev.* **128**, 2042 (1962).
19. Seidel, K. et al. Protein solid-state NMR resonance assignments from (^{13}C,^{13}C) correlation spectroscopy. *Phys. Chem. Chem. Phys.* **6**, 5090-5093 (2004).

20. Baldus, M. Cross polarization in the tilted frame: assignment and spectral simplification in heteronuclear spin systems. *Mol. Phys.* **95**, 1197 - 1207 (1998).
21. Wishart, D.S. & Nip, A.M. Protein chemical shift analysis: a practical guide. *Biochem. Cell Biol.* **76**, 153-163 (1998).
22. Cavalli, A., Salvatella, X., Dobson, C.M. & Vendruscolo, M. Protein structure determination from NMR chemical shifts. *Proc. Natl. Acad. Sci. U.S.A.* **104**, 9615-9620 (2007).
23. Heise, H., Luca, S., de Groot, B.L., Grubmüller, H. & Baldus, M. Probing Conformational Disorder in Neurotensin by Two-Dimensional Solid-State NMR and Comparison to Molecular Dynamics Simulations. *Biophys. J.* **89**, 2113-2120 (2005).
24. Jaroniec, C.P., Tounge, B.A., Herzfeld, J. & Griffin, R.G. Frequency Selective Heteronuclear Dipolar Recoupling in Rotating Solids: Accurate ^{13}C-^{15}N Distance Measurements in Uniformly ^{13}C,^{15}N-labeled Peptides. *J. Am. Chem. Soc.***123**, 3507-3519 (2001).
25. Takegoshi, K., Nomura, K. & Terao, T. Selective Homonuclear Polarization Transfer in the Tilted Rotating Frame under Magic Angle Spinning in Solids. *J. Magn. Reson.* **127**, 206-216 (1997).
26. De Paepe, G., Lewandowski, J.R., Loquet, A., Böckmann, A. & Griffin, R.G. Proton assisted recoupling and protein structure determination. *J. Chem. Phys.* **129**, 245101-21 (2008).
27. Takegoshi, K., Nakamura, S. & Terao, T. ^{13}C-^{1}H dipolar-assisted rotational resonance in magic-angle spinning NMR. *Chem. Phys. Lett.* **344**, 631-637 (2001).
28. Tang, M., Waring, A.J. & Hong, M. Intermolecular Packing and Alignment in an Ordered b-Hairpin Antimicrobial Peptide Aggregate from 2D Solid-State NMR. *J. Am. Chem. Soc.* **127**, 13919-13927 (2005).
29. Lange, A. et al. A concept for rapid protein-structure determination by solid-state NMR spectroscopy. *Angew. Chem. Int. Ed.* **44**, 2089-2092 (2005).
30. Lange, A., Luca, S. & Baldus, M. Structural Constraints from Proton-Mediated Rare-Spin Correlation Spectroscopy in Rotating Solids. *J. Am. Chem. Soc* **124**, 9704-9705 (2002).
31. Ulrich, A.S. Solid state ^{19}F NMR methods for studying biomembranes. *Prog. Nucl. Magn. Reson. Spectrosc.* **46**, 1-21 (2005).
32. Nadaud, P.S., Helmus, J.J., Hofer, N. & Jaroniec, C.P. Long-Range Structural Restraints in Spin-Labeled Proteins Probed by Solid-State Nuclear Magnetic Resonance Spectroscopy. *J. Am. Chem. Soc.* **129**, 7502-7503 (2007).
33. Goldman, M. & Shen, L. Spin-Spin Relaxation in LaF_3. *Phys. Rev.* **144**, 321-331 (1966).
34. Kumashiro, K.K. et al. A Novel Tool for Probing Membrane Protein Structure: Solid-State NMR with Proton Spin Diffusion and X-Nucleus Detection. *J. Am. Chem. Soc.* **120**, 5043-5051 (1998).
35. Lesage, A. et al. Polarization Transfer over the Water-Protein Interface in Solids. *Angew. Chem. Int. Ed.* **47**, 5851-5854 (2008).
36. Huster, D. Investigations of the structure and dynamics of membrane-associated peptides by magic angle spinning NMR. *Prog. Nucl. Magn. Reson. Spectrosc.* **46**, 79-107 (2005).

37. Giraud, N. et al. Site-Specific Backbone Dynamics from a Crystalline Protein by Solid-State NMR Spectroscopy. *J. Am. Chem. Soc.* **126**, 11422-11423 (2004).
38. Franks, W.T. et al. Magic-Angle Spinning Solid-State NMR Spectroscopy of the b1 Immunoglobulin Binding Domain of Protein G (GB1): ^{15}N and ^{13}C Chemical Shift Assignments and Conformational Analysis. *J. Am. Chem. Soc.***127**, 12291-12305 (2005).
39. Wylie, B.J., Franks, W.T. & Rienstra, C.M. Determinations of ^{15}N Chemical Shift Anisotropy Magnitudes in a Uniformly ^{15}N,^{13}C-Labeled Microcrystalline Protein by Three-Dimensional Magic-Angle Spinning Nuclear Magnetic Resonance Spectroscopy. *J. Phys. Chem. B* **110**, 10926-10936 (2006).
40. Andronesi, O.C. et al. Determination of membrane protein structure and dynamics by magic-angle-spinning solid-state NMR spectroscopy. *J. Am. Chem. Soc.* **127**, 12965-12974 (2005).
41. Gawrisch, K., Eldho, N.V. & Polozov, I.V. Novel NMR tools to study structure and dynamics of biomembranes. *Chem. Phys. Lipids* **116**, 135-151 (2002).
42. Jeener, J., Meier, B.H., Bachmann, P. & Ernst, R.R. Investigation of Exchange Processes by 2-Dimensional Nmr- Spectroscopy. *J. Chem. Phys.* **71**, 4546-4553 (1979).
43. Cotts, R.M., Hoch, M.J.R., Sun, T. & Markert, J.T. Pulse Field Stimulated Echo Methods for Improved NMR Diffusion Measurements in Heterogeneous Systems. *J. Magn. Reson.* **83**, 252-266 (1989).
44. Gawrisch, K. & Gaede, H.C. Measurement of Lateral Diffusion Rates in Membranes by Pulsed Magnetic Field Gradient, Magic Angle Spinning-Proton Nuclear Magnetic Resonance. *Methods Mol. Biol.* Vol. 400 257-265 (2007).
45. Schrempf, H. et al. A prokaryotic potassium ion channel with two predicted transmembrane segments from Streptomyces lividans. *EMBO J.* **14**, 5170-5178 (1995).
46. Zhou, Y., Morais-Cabral, J.H., Kaufman, A. & MacKinnon, R. Chemistry of ion coordination and hydration revealed by a K^+ channel-Fab complex at 2.0Å resolution. *Nature* **414**, 43-48 (2001).
47. Perozo, E., Cortes, D.M. & Cuello, L.G. Three-dimensional architecture and gating mechanism of a K^+ channel studied by EPR spectroscopy. *Nat. Struct. Mol. Biol.* **5**, 459-469 (1998).
48. Alber, F. et al. The molecular architecture of the nuclear pore complex. *Nature* **450**, 695-701 (2007).
49. Frey, S., Richter, R.P. & Görlich, D. FG-Rich Repeats of Nuclear Pore Proteins Form a Three-Dimensional Meshwork with Hydrogel-Like Properties. *Science* **314**, 815-817 (2006).
50. Terry, L.J., Shows, E.B. & Wente, S.R. Crossing the Nuclear Envelope: Hierarchical Regulation of Nucleocytoplasmic Transport. *Science* **318**, 1412-1416 (2007).
51. MacKinnon, R. Potassium Channels and the Atomic Basis of Selective Ion Conduction (Nobel Lecture). *Angew. Chem. Int. Ed.* **43**, 4265-4277 (2004).
52. Shimizu, H. et al. Global Twisting Motion of Single Molecular KcsA Potassium Channel upon Gating. *Cell* **132**, 67-78 (2008).
53. Jares-Erijman, E.A. & Jovin, T.M. FRET imaging. *Nat. Biotech.* **21**, 1387-1395 (2003).
54. Klare, J.P. et al. The archaeal sensory rhodopsin II/transducer complex: a model for transmembrane signal transfer. *FEBS Lett.* **564**, 219-224 (2004).

55. Liang, B., Bushweller, J.H. & Tamm, L.K. Site-Directed Parallel Spin-Labeling and Paramagnetic Relaxation Enhancement in Structure Determination of Membrane Proteins by Solution NMR Spectroscopy. *J. Am. Chem. Soc.* **128**, 4389-4397 (2006).
56. Hong, M. Structure, Topology, and Dynamics of Membrane Peptides and Proteins from Solid-State NMR Spectroscopy. *J. Phys. Chem. B* **111**, 10340-10351 (2007).
57. Gallagher, G.J., Hong, M. & Thompson, L.K. Solid-State NMR Spin Diffusion for Measurement of Membrane-Bound Peptide Structure: Gramicidin A. *Biochemistry* **43**, 7899-7906 (2004).
58. Huster, D., Yao, X. & Hong, M. Membrane Protein Topology Probed by ^{1}H Spin Diffusion from Lipids Using Solid-State NMR Spectroscopy. *J. Am. Chem. Soc.* **124**, 874-883 (2002).
59. Lesage, A., Emsley, L., Penin, F. & Böckmann, A. Investigation of Dipolar-Mediated Water-Protein Interactions in Microcrystalline Crh by Solid-State NMR Spectroscopy. *J. Am. Chem. Soc.* **128**, 8246-8255 (2006).
60. Willard, L. et al. VADAR: a web server for quantitative evaluation of protein structure quality. *Nucl. Acids Res.* **31**, 3316-3319 (2003).
61. Liu, Y.-S., Sompornpisut, P. & Perozo, E. Structure of the KcsA channel intracellular gate in the open state. *Nat. Struct. Mol. Biol.* **8**, 883-887 (2001).
62. Royant, A. et al. X-ray structure of sensory rhodopsin II at 2.1-A resolution. *Proc. Natl. Acad. Sci. U.S.A.* **98**, 10131-10136 (2001).
63. Cortes, D.M., Cuello, L.G. & Perozo, E. Molecular Architecture of Full-Length KcsA: Role of Cytoplasmic Domains in Ion Permeation and Activation Gating. *J. Gen. Physiol.* **117**, 165-180 (2001).
64. Schmidt-Rohr, K. & Spiess, H.W. *Multidimensional Solid-State NMR and Polymers* (Academic Press, London/San Diego, 1994).
65. Lange, A., Seidel, K., Verdier, L., Luca, S. & Baldus, M. Analysis of proton-proton transfer dynamics in rotating solids and their use for 3D structure determination. *J. Am. Chem. Soc.* **125**, 12640-12648 (2003).
66. Böckmann, A. et al. Water–Protein Hydrogen Exchange in the Micro-Crystalline Protein Crh as Observed by Solid State NMR Spectroscopy. *J. Biomol. NMR* **32**, 195-207 (2005).
67. Bernèche, S. & Roux, B. Molecular dynamics of the KcsA K(+) channel in a bilayer membrane. *Biophys. J.* **78**, 2900-2917 (2000).
68. Boiteux, C., Kraszewski, S., Ramseyer, C. & Girardet, C. Ion conductance vs. pore gating and selectivity in KcsA channel: Modeling achievements and perspectives. *J. Mol. Model.* **13**, 699-713 (2007).
69. Jiang, Y. et al. The open pore conformation of potassium channels. *Nature* **417**, 523-526 (2002).
70. Long, S.B., Campbell, E.B. & MacKinnon, R. Crystal Structure of a Mammalian Voltage-Dependent Shaker Family K^+ Channel. *Science* **309**, 897-903 (2005).
71. Ader, C. et al. A structural link between inactivation and block of a K^+ channel. *Nat. Struct. Mol. Biol.* **15**, 605-612 (2008).
72. Assink, R.A. Nuclear Spin Diffusion between Polyurethane Microphases. *Macromolecules* **11**, 1233-1237 (1978).
73. Egger, N., Schmidt-Rohr, K., Blümich, B., Domke, W.D. & Stapp, B. Solid state NMR investigation of cationic polymerized epoxy resins. *J. Appl. Polym. Sci.* **44**, 289-295 (1992).

74. Andronesi, O.C. et al. Characterization of Alzheimer's-like Paired Helical Filaments from the Core Domain of Tau Protein Using Solid-State NMR Spectroscopy. *J. Am. Chem. Soc.* **130**, 5922-5928 (2008).
75. Hubbell, W.L., Cafiso, D.S. & Altenbach, C. Identifying conformational changes with site-directed spin labeling. *Nat. Struct. Mol. Biol.* **7**, 735-739 (2000).
76. Sompornpisut, P., Roux, B. & Perozo, E. Structural refinement of membrane proteins by restrained molecular dynamics and solvent accessibility data. *Biophys. J.*, **95**, 5349-5361 (2008).
77. Fung, B.M., Khitrin, A.K. & Ermolaev, K. An Improved Broadband Decoupling Sequence for Liquid Crystals and Solids. *J. Magn. Reson.* **142**, 97-101 (2000).
78. Hille, B. *Ionic Channels of Excitable Membranes*, 3 ed. Sinauer Associates Inc., Sunderland, MA (2001).
79. Yellen, G. The moving parts of voltage-gated ion channels. *Q. Rev. Biophys.* **31**, 239-295 (1998).
80. Bean, B.P. The action potential in mammalian central neurons. *Nat. Rev. Neurosci.* **8**, 451-465 (2007).
81. Starkus, J.G., Kuschel, L., Rayner, M.D. & Heinemann, S.H. Ion Conduction through C-Type Inactivated Shaker Channels. *J. Gen. Physiol.* **110**, 539-550 (1997).
82. Starkus, J.G., Kuschel, L., Rayner, M.D. & Heinemann, S.H. Macroscopic Na^+ Currents in the "Nonconducting" Shaker Potassium Channel Mutant W434F. *J. Gen. Physiol.* **112**, 85-93 (1998).
83. Valiyaveetil, F.I., Leonetti, M., Muir, T.W. & MacKinnon, R. Ion Selectivity in a Semisynthetic K^+ Channel Locked in the Conductive Conformation. *Science* **314**, 1004-1007 (2006).
84. Bernèche, S. & Roux, B. A Gate in the Selectivity Filter of Potassium Channels. *Structure* **13**, 591-600 (2005).
85. Cordero-Morales, J.F., Cuello, L.G. & Perozo, E. Voltage-dependent gating at the KcsA selectivity filter. *Nat. Struct. Mol. Biol.* **13**, 319-322 (2006).
86. Cordero-Morales, J.F. et al. Molecular determinants of gating at the potassium-channel selectivity filter. *Nat. Struct. Mol. Biol.* **13**, 311-318 (2006).
87. Cordero-Morales, J.F. et al. Molecular driving forces determining potassium channel slow inactivation. *Nat. Struct. Mol. Biol.* **14**, 1062-1069 (2007).
88. Blunck, R., Cordero-Morales, J.F., Cuello, L.G., Perozo, E. & Bezanilla, F. Detection of the Opening of the Bundle Crossing in KcsA with Fluorescence Lifetime Spectroscopy Reveals the Existence of Two Gates for Ion Conduction. *J. Gen. Physiol.* **128**, 569-581 (2006).
89. Long, S.B., Tao, X., Campbell, E.B. & MacKinnon, R. Atomic structure of a voltage-dependent K^+ channel in a lipid membrane-like environment. *Nature* **450**, 376-382 (2007).
90. Gradl, S.N., Felix, J.P., Isacoff, E.Y., Garcia, M.L. & Trauner, D. Protein Surface Recognition by Rational Design: Nanomolar Ligands for Potassium Channels. *J. Am. Chem. Soc.* **125**, 12668-12669 (2003).
91. Baker, K.A., Tzitzilonis, C., Kwiatkowski, W., Choe, S. & Riek, R. Conformational dynamics of the KcsA potassium channel governs gating properties. *Nat. Struct. Mol. Biol.* **14**, 1089-1095 (2007).

92. Chill, J.H., Louis, J.M., Delaglio, F. & Bax, A. Local and global structure of the monomeric subunit of the potassium channel KcsA probed by NMR. *Biochim. Biophys. Acta, Biomembr.* **1768**, 3260-3270 (2007).
93. Chill, J.H., Louis, J.M., Miller, C. & Bax, A. NMR study of the tetrameric KcsA potassium channel in detergent micelles. *Protein Sci.* **15**, 684-698 (2006).
94. Takeuchi, K., Takahashi, H., Kawano, S. & Shimada, I. Identification and Characterization of the Slowly Exchanging pH-dependent Conformational Rearrangement in KcsA. *J. Biol. Chem.* **282**, 15179-15186 (2007).
95. Yu, L. et al. Nuclear Magnetic Resonance Structural Studies of a Potassium Channel-Charybdotoxin Complex. *Biochemistry* **44**, 15834-15841 (2005).
96. Matthews, E.E., Zoonens, M. & Engelman, D.M. Dynamic Helix Interactions in Transmembrane Signaling. *Cell* **127**, 447-450 (2006).
97. Valiyaveetil, F.I., Zhou, Y. & MacKinnon, R. Lipids in the Structure, Folding, and Function of the KcsA K^+ Channel. *Biochemistry* **41**, 10771-10777 (2002).
98. Cuello, L.G., Romero, J.G., Cortes, D.M. & Perozo, E. pH-Dependent Gating in the Streptomyces lividans K^+ Channel. *Biochemistry* **37**, 3229-3236 (1998).
99. Heginbotham, L., LeMasurier, M., Kolmakova-Partensky, L. & Miller, C. Single Streptomyces lividans K^+ Channels: Functional Asymmetries and Sidedness of Proton Activation. *J. Gen. Physiol.* **114**, 551-560 (1999).
100. Luca, S. et al. Secondary chemical shifts in immobilized peptides and proteins: A qualitative basis for structure refinement under Magic Angle Spinning. *J. Biomol. NMR* **20**, 325-331 (2001).
101. Neal, S., Nip, A.M., Zhang, H. & Wishart, D.S. Rapid and accurate calculation of protein ^{1}H, ^{13}C and ^{15}N chemical shifts. *J. Biomol. NMR* **26**, 215-240 (2003).
102. Brünger, A.T. et al. Crystallography & NMR system: A new software suite for macromolecular structure determination. *Acta Crystallogr. D Biol. Crystallogr.* **54**, 905-921 (1998).
103. Morris, A.L., MacArthur, M.W., Hutchinson, E.G. & Thornton, J.M. Stereochemical quality of protein structure coordinates. *Proteins* **12**, 345-364 (1992).
104. Lockless, S.W., Zhou, M. & MacKinnon, R. Structural and thermodynamic properties of selective ion binding in a K^+ channel. *PLoS Biol.* **5**, e121 (2007).
105. Jiang, Y. et al. X-ray structure of a voltage-dependent K^+ channel. *Nature* **423**, 33-41 (2003).
106. Bielecki, A., Kolbert, A.C. & Levitt, M.H. Frequency-switched pulse sequences: Homonuclear decoupling and dilute spin NMR in solids. *Chem. Phys. Lett.* **155**, 341-346 (1989).
107. Dominguez, C., Boelens, R. & Bonvin, A.M.J.J. HADDOCK: A Protein-Protein Docking Approach Based on Biochemical or Biophysical Information. *J. Am. Chem. Soc.* **125**, 1731-1737 (2003).
108. Woodhull, A.M. Ionic Blockage of Sodium Channels in Nerve. *J. Gen. Physiol.* **61**, 687-708 (1973).
109. Lenaeus, M.J., Vamvouka, M., Focia, P.J. & Gross, A. Structural basis of TEA blockade in a model potassium channel. *Nat. Struct. Mol. Biol.* **12**, 454-459 (2005).
110. Ernst, R.R., Bodenhausen, G. & Wokaun, A. *Principles of Nuclear Magnetic Resonance in One and Two Dimensions*, Clarendon Press, Oxford (1987).

111. Huster, D., Arnold, K. & Gawrisch, K. Investigation of Lipid Organization in Biological Membranes by Two-Dimensional Nuclear Overhauser Enhancement Spectroscopy. *J. Phys. Chem. B* **103**, 243-251 (1999).
112. Schüttelkopf, A.W. & van Aalten, D.M.F. PRODRG: a tool for high-throughput crystallography of protein-ligand complexes. *Acta Crystallogr. D Biol. Crystallogr.* **60**, 1355-1363 (2004).
113. Delcour, A.H., Martinac, B., Adler, J. & Kung, C. Modified reconstitution method used in patch-clamp studies of Escherichia coli ion channels. *Biophys. J.* **56**, 631-636 (1989).
114. Hille, B. (ed.) *Ion channels of excitable membranes, 3rd ed.*, Sinauer, Sunderland, Mass. (2001).
115. Armstrong, C.M. Voltage-Gated K Channels. *Sci. STKE* **2003**, re10 (2003).
116. Liu, Y., Holmgren, M., Jurman, M.E. & Yellen, G. Gated Access to the Pore of a Voltage-Dependent K^+ Channel. *Neuron* **19**, 175-184 (1997).
117. Doyle, D.A. et al. The Structure of the Potassium Channel: Molecular Basis of K^+ Conduction and Selectivity. *Science* **280**, 69-77 (1998).
118. Holmgren, M., Shin, K.S. & Yellen, G. The Activation Gate of a Voltage-Gated K^+ Channel Can Be Trapped in the Open State by an Intersubunit Metal Bridge. *Neuron* **21**, 617-621 (1998).
119. Perozo, E., Cortes, M.D. & Cuello, L.G. Structural Rearrangements Underlying K^+-Channel Activation Gating. *Science* **285**, 73-78 (1999).
120. Jiang, Y. et al. Crystal structure and mechanism of a calcium-gated potassium channel. *Nature* **417**, 515-522 (2002).
121. Kelly, B.L. & Gross, A. Potassium channel gating observed with site-directed mass tagging. *Nat. Struct. Mol. Biol.* **10**, 280-284 (2003).
122. Liu, Y., Jurman, M.E. & Yellen, G. Dynamic Rearrangement of the Outer Mouth of a K^+ Channel during Gating. *Neuron* **16**, 859-867 (1996).
123. Zheng, J. & Sigworth, F.J. Selectivity Changes during Activation of Mutant Shaker Potassium Channels. *J. Gen. Physiol.* **110**, 101-117 (1997).
124. Kiss, L. & Korn, S.J. Modulation of C-type inactivation by K^+ at the potassium channel selectivity filter. *Biophys. J.* **74**, 1840-1849 (1998).
125. Ogielska, E.M. & Aldrich, R.W. Functional Consequences of a Decreased Potassium Affinity in a Potassium Channel Pore. Ion Interactions and C-Type Inactivation. *J. Gen. Physiol.* **113**, 347-358 (1999).
126. Gao, L., Mi, X., Paajanen, V., Wang, K. & Fan, Z. From the Cover: Activation-coupled inactivation in the bacterial potassium channel KcsA. *Proc. Natl. Acad. Sci. U.S.A.* **102**, 17630-17635 (2005).
127. Kurata, H.T. & Fedida, D. A structural interpretation of voltage-gated potassium channel inactivation. *Prog. Biophys. Mol. Biol.* **92**, 185-208 (2006).
128. Chakrapani, S., Cordero-Morales, J.F. & Perozo, E. A Quantitative Description of KcsA Gating II: Single-Channel Currents. *J. Gen. Physiol.* **130**, 479-496 (2007).
129. Baukrowitz, T. & Yellen, G. Modulation of K^+ current by frequency and external $[K^+]$: A tale of two inactivation mechanisms. *Neuron* **15**, 951-960 (1995).
130. Baukrowitz, T. & Yellen, G. Use-dependent blockers and exit rate of the last ion from the multi-ion pore of a K^+ channel. *Science* **271**, 653-656 (1996).
131. Panyi, G. & Deutsch, C. Cross Talk between Activation and Slow Inactivation Gates of Shaker Potassium Channels. *J. Gen. Physiol.* **128**, 547-559 (2006).

132. Panyi, G. & Deutsch, C. Probing the cavity of the slow inactivated conformation of shaker potassium channels. *J. Gen. Physiol.* **129**, 403-418 (2007).
133. Thompson, A.N., Posson, D.J., Parsa, P.V. & Nimigean, C.M. Molecular mechanism of pH sensing in KcsA potassium channels. *Proc. Natl. Acad. Sci. U.S.A.* **105**, 6900-6905 (2008).
134. Claydon, T.W. et al. A Direct Demonstration of Closed-State Inactivation of K^+ Channels at Low pH. *J. Gen. Physiol.* **129**, 437-455 (2007).
135. Zagotta, W.N. & Aldrich, R.W. Voltage-dependent gating of Shaker A-type potassium channels in Drosophila muscle. *J. Gen. Physiol.* **95**, 29-60 (1990).
136. Demo, S.D. & Yellen, G. The inactivation gate of the Shaker K^+ channel behaves like an open-channel blocker. *Neuron* **7**, 743-753 (1991).
137. Roeper, J., Lorra, C. & Pongs, O. Frequency-Dependent Inactivation of Mammalian A-Type K^+ Channel KV1.4 Regulated by Ca^{2+}/Calmodulin-Dependent Protein Kinase. *J. Neurosci.* **17**, 3379-3391 (1997).
138. Ader, C. et al. Structural Rearrangements of Membrane Proteins Probed by Water-Edited Solid-State NMR Spectroscopy. *J. Am. Chem. Soc.* **131**, 170-176 (2009).
139. Keim, P., Vigna, R.A., Morrow, J.S., Marshall, R.C. & Gurd, F.R.N. Carbon 13 Nuclear Magnetic Resonance of Pentapeptides of Glycine Containing Central Residues of Serine, Threonine, Aspartic and Glutamic Acids, Asparagine, and Glutamine. *J. Biol. Chem.* **248**, 7811-7818 (1973).
140. Zachariae, U. et al. The molecular mechanism of toxin-induced conformational changes in a potassium channel: Relation to C-type inactivation. *Structure* **16**, 747-754 (2008).
141. Zakharian, E. & Reusch, R.N. Streptomyces lividans potassium channel KcsA is regulated by the potassium electrochemical gradient. *Biochem. Biophys. Res. Commun.* **316**, 429-436 (2004).
142. LeMasurier, M., Heginbotham, L. & Miller, C. KcsA: It's a Potassium Channel. *J. Gen. Physiol.* **118**, 303-314 (2001).
143. Hurst, R.S., Roux, M.J., Toro, L. & Stefani, E. External barium influences the gating charge movement of Shaker potassium channels. *Biophys. J.* **72**, 77-84 (1997).
144. Engelman, D.M. Membranes are more mosaic than fluid. *Nature* **438**, 578-580 (2005).
145. Singer, S.J. & Nicolson, G.L. The fluid mosaic model of the structure of cell membranes. *Science* **175**, 720-731 (1972).
146. Andersen, O.S. & Koeppe, R.E. Bilayer Thickness and Membrane Protein Function: An Energetic Perspective. *Annu. Rev. Biophys. Biomol. Struct.* **36**, 107-130 (2007).
147. Lee, A.G. How lipids affect the activities of integral membrane proteins. *Biochim. Biophys. Acta, Biomembr.* **1666**, 62-87 (2004).
148. Marsh, D. Protein modulation of lipids, and vice-versa, in membranes. *Biochim. Biophys. Acta, Biomembr.* **1778**, 1545-1575 (2008).
149. Alvis, S.J., Williamson, I.M., East, J.M. & Lee, A.G. Interactions of Anionic Phospholipids and Phosphatidylethanolamine with the Potassium Channel KcsA. *Biophys. J.* **85**, 3828-3838 (2003).
150. Deol, S.S., Domene, C., Bond, P.J. & Sansom, M.S.P. Anionic Phospholipid Interactions with the Potassium Channel KcsA: Simulation Studies. *Biophys. J.* **90**, 822-830 (2006).

151. Demmers, J.A.A., van Dalen, A., de Kruijff, B., Heck, A.J.R. & Killian, J.A. Interaction of the K^+ channel KcsA with membrane phospholipids as studied by ESI mass spectrometry. *FEBS lett.* **541**, 28-32 (2003).
152. Marius, P., Alvis, S.J., East, J.M. & Lee, A.G. The Interfacial Lipid Binding Site on the Potassium Channel KcsA Is Specific for Anionic Phospholipids. **89**, 4081-4089 (2005).
153. Marius, P., Alvis, S.J., East, J.M. & Lee, A.G. The Interfacial Lipid Binding Site on the Potassium Channel KcsA Is Specific for Anionic Phospholipids. *Biophys. J.* **89**, 4081-4089 (2005).
154. Williamson, I.M., Alvis, S.J., East, J.M. & Lee, A.G. Interactions of Phospholipids with the Potassium Channel KcsA. *Biophys. J.* **83**, 2026-2038 (2002).
155. Williamson, I.M., Alvis, S.J., East, J.M. & Lee, A.G. The potassium channel KcsA and its interaction with the lipid bilayer. *Cell. Mol. Life Sci. (CMLS)* **60**, 1581-1590 (2003).
156. van Dalen, A., Sander, H., Killian, J.A. & de Kruijff, B. Influence of lipids on membrane assembly and stability of the potassium channel KcsA. *FEBS lett.* **525**, 33-38 (2002).
157. Barrera, F.N. et al. Protein self-assembly and lipid binding in the folding of the potassium channel KcsA. *Biochemistry* **47**, 2123-2133 (2008).
158. Molina, M.L. et al. Influence of C-Terminal Protein Domains and Protein-Lipid Interactions on Tetramerization and Stability of the Potassium Channel KcsA. *Biochemistry* **43**, 14924-14931 (2004).
159. Legros, C. et al. Engineering-Specific Pharmacological Binding Sites for Peptidyl Inhibitors of Potassium Channels into KcsA. *Biochemistry* **41**, 15369-15375 (2002).
160. Krishnan, M.N., Trombley, P. & Moczydlowski, E.G. Thermal Stability of the K^+ Channel Tetramer: Cation Interactions and the Conserved Threonine Residue at the Innermost Site (S4) of the KcsA Selectivity Filter. *Biochemistry* **47**, 5354-5367 (2008).
161. Raja, M., Spelbrink, R.E.J., de Kruijff, B. & Killian, J.A. Phosphatidic acid plays a special role in stabilizing and folding of the tetrameric potassium channel KcsA. *FEBS lett.* **581**, 5715-5722 (2007).
162. Barrera, F.N. et al. Unfolding and Refolding in Vitro of a Tetrameric, alpha-Helical Membrane Protein; The Prokaryotic Potassium Channel KcsA. *Biochemistry* **44**, 14344-14352 (2005).
163. van den Brink-van der Laan, E., Chupin, V., Killian, J.A. & de Kruijff, B. Stability of KcsA Tetramer Depends on Membrane Lateral Pressure. *Biochemistry* **43**, 4240-4250 (2004).
164. van den Brink-van der Laan, E., Chupin, V., Killian, J.A. & de Kruijff, B. Small Alcohols Destabilize the KcsA Tetramer via Their Effect on the Membrane Lateral Pressure. *Biochemistry* **43**, 5937-5942 (2004).
165. Uysal, S. et al. Crystal structure of full-length KcsA in its closed conformation. *Proc. Natl. Acad. Sci. U.S.A.* **106**, 6644-6649 (2009).
166. Umigai, N. et al. Topogenesis of Two Transmembrane Type K^+ Channels, Kir 2.1 and KcsA. *J. Biol. Chem.* **278**, 40373-40384 (2003).
167. Bogdanov, M., Mileykovskaya, E. & Dowhan, W. Lipids in the Assembly of Membrane Proteins and Organization of Protein Supercomplexes. *Subcell. Biochem.* **49**, 197-239 (2008).

168. Bos, M.P., Robert, V. & Tommassen, J. Biogenesis of the Gram-Negative Bacterial Outer Membrane. *Annu. Rev. Microbiol.* **61**, 191-214 (2007).
169. Sanders, C.R. & Myers, J.K. Disease-related misassembly of membrane proteins. *Annu. Rev. Biophys. Biomol. Struct.***33**, 25-51 (2004).
170. Van Dalen, A., Schrempf, H., Killian, J.A. & De Kruijff, B. Efficient membrane assembly of the KcsA potassium channel in Escherichia coli requires the protonmotive force *EMBO Rep.* **1**, 340-346 (2000).
171. van Dalen, A., van der Laan, M., Driessen, J.A., Killian, J.A. & De Kruijff, B. Components required for membrane assembly of newly synthesized K^+ channel KcsA. *FEBS lett.* **511**, 51-58 (2002).
172. Heginbotham, L., Kolmakova-Partensky, L. & Miller, C. Functional Reconstitution of a Prokaryotic K^+ Channel. *J. Gen. Physiol.* **111**, 741-749 (1998).
173. Guidoni, L., Torre, V. & Carloni, P. Potassium and Sodium Binding to the Outer Mouth of the K^+ Channel. *Biochemistry* **38**, 8599-8604 (1999).
174. Smock, R.G. & Gierasch, L.M. Sending Signals Dynamically. *Science* **324**, 198-203 (2009).
175. Boehr, D.D., McElheny, D., Dyson, H.J. & Wright, P.E. The Dynamic Energy Landscape of Dihydrofolate Reductase Catalysis. *Science* **313**, 1638-1642 (2006).
176. Mittermaier, A. & Kay, L.E. New Tools Provide New Insights in NMR Studies of Protein Dynamics. *Science* **312**, 224-228 (2006).
177. Seelig, J. Deuterium Magnetic-Resonance - Theory and Application to Lipid-Membranes. *Q. Rev. Biophys.* **10**, 353-418 (1977).
178. Herzfeld, J., Roufosse, A., Haberkorn, R.A., Griffin, R.G. & Glimcher, M.J. Magic Angle Sample Spinning in Inhomogeneously Broadened Biological-Systems. *Philos. Trans. R. Soc. London, Ser. B* **289**, 459-469 (1980).
179. Gennis, R.B. *Biomembranes: Molecular Structure and Function*, Springer, New York (1989).
180. Andrew, E.R., Bradbury, A. & Eades, R.G. Nuclear Magnetic Resonance Spectra from a crystal rotated at high speed. *Nature* **182**, 1659 (1958).
181. Traaseth, N.J. et al. Structural and Dynamic Basis of Phospholamban and Sarcolipin Inhibition of Ca^{2+}-ATPase. *Biochemistry* **47**, 3-13 (2008).
182. Dürr, U.H.N., Waskell, L. & Ramamoorthy, A. The cytochromes P450 and b5 and their reductases-Promising targets for structural studies by advanced solid-state NMR spectroscopy. *Biochim. Biophys. Acta, Biomembr.* **1768**, 3235-3259 (2007).
183. Allen, T.W., Kuyucak, S. & Chung, S.H. Molecular dynamics study of the KcsA potassium channel. *Biophys. J.* **77**, 2502-2516 (1999).
184. Aqvist, J. & Luzhkov, V. Ion permeation mechanism of the potassium channel. *Nature* **404**, 881-884 (2000).
185. Shrivastava, I.H., Capener, C.E., Forrest, L.R. & Sansom, M.S.P. Structure and Dynamics of K Channel Pore-Lining Helices: A Comparative Simulation Study. *Biophys. J.* **78**, 79-92 (2000).
186. Shrivastava, I.H. & Sansom, M.S.P. Simulations of Ion Permeation Through a Potassium Channel: Molecular Dynamics of KcsA in a Phospholipid Bilayer. *Biophys. J.* **78**, 557-570 (2000).
187. Bernèche, S. & Roux, B. Energetics of ion conduction through the K^+ channel. *Nature* **414**, 73-77 (2001).

188. Morais-Cabral, J.H., Zhou, Y. & MacKinnon, R. Energetic optimization of ion conduction rate by the K^+ selectivity filter. *Nature* **414**, 37-42 (2001).
189. Domene, C. & Sansom, M.S.P. Potassium Channel, Ions, and Water: Simulation Studies Based on the High Resolution X-Ray Structure of KcsA. *Biophys. J.* **85**, 2787-2800 (2003).
190. Zhou, Y. & MacKinnon, R. The Occupancy of Ions in the K^+ Selectivity Filter: Charge Balance and Coupling of Ion Binding to a Protein Conformational Change Underlie High Conduction Rates. *J. Mol. Biol.* **333**, 965-975 (2003).
191. Valiyaveetil, F.I., Sekedat, M., MacKinnon, R. & Muir, T.W. Glycine as a d-amino acid surrogate in the K^+-selectivity filter. *Proc. Natl. Acad. Sci. U.S.A.* **101**, 17045-17049 (2004).
192. Zhou, M. & MacKinnon, R. A Mutant KcsA K^+ Channel with Altered Conduction Properties and Selectivity Filter Ion Distribution. *J. Mol. Biol.* **338**, 839-846 (2004).
193. VanDongen, A.M.J. K channel gating by an affinity-switching selectivity filter. *Proc. Natl. Acad. Sci. U.S.A.* **101**, 3248-3252 (2004).
194. Mani, R. et al. Membrane-dependent oligomeric structure and pore formation of a beta-hairpin antimicrobial peptide in lipid bilayers from solid-state NMR. *Proc. Natl. Acad. Sci. U.S.A.* **103**, 16242-16247 (2006).
195. Torchia, D.A. Solid-State Nmr-Studies of Protein Internal Dynamics. *Annu. Rev. Biophys. Bioeng.* **13**, 125-144 (1984).
196. Cole, H.B.R. & Torchia, D.A. An Nmr-Study of the Backbone Dynamics of Staphylococcal Nuclease in the Crystalline State. *Chem. Phys.* **158**, 271-281 (1991).
197. Giraud, N. et al. Quantitative analysis of backbone dynamics in a crystalline protein from nitrogen-15 spin-lattice relaxation. *J. Am. Chem. Soc.* **127**, 18190-18201 (2005).
198. Baldus, M. Correlation experiments for assignment and structure elucidation of immobilized polypeptides under magic angle spinning. *Prog. Nucl. Magn. Reson. Spectrosc.* **41**, 1-47 (2002).
199. Cady, S.D. & Hong, M. Amantadine-induced conformational and dynamical changes of the influenza M2 transmembrane proton channel. *Proc. Natl. Acad. Sci. U.S.A.* **105**, 1483-1488 (2008).
200. Etzkorn, M. et al. Plasticity of the PAS domain and a potential role for signal transduction in the histidine kinase DcuS. *Nat. Struct. Mol. Biol.* **15**, 1031-1039 (2008).
201. Petkova, A.T. et al. Backbone and side chain assignment strategies for multiply labeled membrane peptides and proteins in the solid state. *J. Magn. Reson.* **160**, 1-12 (2003).
202. Görlich, D. & Kutay, U. Transport between the cell nucleus and the cytoplasm. *Annu. Rev. Cell Dev. Biol.* **15**, 607-660 (1999).
203. Macara, I.G. Transport into and out of the nucleus. *Microbiol. Mol. Biol. Rev.* **65**, 570-594 (2001).
204. Strawn, L.A., Shen, T., Shulga, N., Goldfarb, D.S. & Wente, S.R. Minimal nuclear pore complexes define FG repeat domains essential for transport. *Nat. Cell Biol.* **6**, 197-206 (2004).
205. Denning, D.P. & Rexach, M.F. Rapid evolution exposes the boundaries of domain structure and function in natively unfolded FG nucleoporins. *Mol. Cell Proteomics* **6**, 272-82 (2007).

206. Denning, D.P., Patel, S.S., Uversky, V., Fink, A.L. & Rexach, M. Disorder in the nuclear pore complex: the FG repeat regions of nucleoporins are natively unfolded. *Proc. Natl. Acad. Sci. U. S. A.* **100**, 2450-5 (2003).
207. Rout, M.P. & Wente, S.R. Pores for thought: nuclear pore complex proteins. *Trends Cell Biol.* **4**, 357-65 (1994).
208. Bayliss, R. et al. Interaction between NTF2 and xFxFG-containing nucleoporins is required to mediate nuclear import of RanGDP. *Journal of Molecular Biology* **293**, 579-593 (1999).
209. Bayliss, R., Littlewood, T. & Stewart, M. Structural basis for the interaction between FxFG nucleoporin repeats and importin-beta in nuclear trafficking. *Cell* **102**, 99-108 (2000).
210. Bednenko, J., Cingolani, G. & Gerace, L. Importin beta contains a COOH-terminal nucleoporin binding region important for nuclear transport. *J. Cell Biol.***162**, 391-401 (2003).
211. Ribbeck, K. & Görlich, D. The permeability barrier of nuclear pore complexes appears to operate via hydrophobic exclusion. *EMBO J.* **21**, 2664-2671 (2002).
212. Iovine, M.K., Watkins, J.L. & Wente, S.R. The GLFG repetitive region of the nucleoporin Nup116p interacts with Kap95p, an essential yeast nuclear import factor. *J. Cell Biol.* **131**, 1699-1713 (1995).
213. Frey, S. & Görlich, D. A saturated FG-repeat hydrogel can reproduce the permeability properties of nuclear pore complexes. *Cell* **130**, 512-523 (2007).
214. Patel, S.S., Belmont, B.J., Sante, J.M. & Rexach, M.F. Natively Unfolded Nucleoporins Gate Protein Diffusion across the Nuclear Pore Complex. **129**, 83-96 (2007).
215. Frey, S. & Görlich, D. submitted. (2009).
216. Ribbeck, K. & Görlich, D. Kinetic analysis of translocation through nuclear pore complexes. *EMBO J.* **20**, 1320-1330 (2001).
217. Siemer, A.B. et al. Observation of Highly Flexible Residues in Amyloid Fibrils of the HET-s Prion. *J. Am. Chem. Soc.***128**, 13224-13228 (2006).
218. Wang, Y. & Jardetzky, O. Probability-based protein secondary structure identification using combined NMR chemical-shift data. *Protein Sci.* **11**, 852-861 (2002).
219. Michelitsch, M.D. & Weissman, J.S. A census of glutamine/asparagine-rich regions: Implications for their conserved function and the prediction of novel prions. *Proc. Natl. Acad. Sci. U.S.A.* **97**, 11910-11915 (2000).
220. Sawaya, M.R. et al. Atomic structures of amyloid cross-beta spines reveal varied steric zippers. *Nature* **447**, 453-457 (2007).
221. Harper, J.D. & Lansbury, P.T. Models of Amyloid seeding in Alzheimer's disease and Scarpie: Mechanistic Truths and Physiological Consequences of the Time-Dependent Solubility of Amyloid Proteins. *Annu. Rev. Biochem.* **66**, 385-407 (1997).
222. Chiti, F. & Dobson, C.M. Protein Misfolding, Functional Amyloids, and Human Disease. *Annu. Rev. Biochem.* **75**, 333-366 (2006).
223. Nelson, R. et al. Structure of the cross-beta spine of amyloid-like fibrils. *Nature* **435**, 773-778 (2005).
224. van der Wel, P.C.A., Lewandowski, J.R. & Griffin, R.G. Solid-State NMR Study of Amyloid Nanocrystals and Fibrils Formed by the Peptide GNNQQNY from Yeast Prion Protein Sup35p. *J. Am. Chem. Soc.* **129**, 5117-5130 (2007).
225. Bates, G. Huntingtin aggregation and toxicity in Huntington's disease. *The Lancet* **361**, 1642-1644 (2003).

226. DePace, A.H., Santoso, A., Hillner, P. & Weissman, J.S. A Critical Role for Amino-Terminal Glutamine/Asparagine Repeats in the Formation and Propagation of a Yeast Prion. *Cell* **93**, 1241-1252 (1998).
227. Alberti, S., Halfmann, R., King, O., Kapila, A. & Lindquist, S. A Systematic Survey Identifies Prions and Illuminates Sequence Features of Prionogenic Proteins. *Cell* **137**, 146-158 (2009).
228. Lee, M. & Goldburg, W.I. Nuclear-Magnetic-Resonance Line Narrowing by a Rotating rf Field. *Phys. Rev.***140**, 1261-1271 (1965).
229. Shaka, A.J., Barker, P.B. & Freeman, R. Computer-optimized decoupling scheme for wideband applications and low-level operation. *J. Magn. Reson. (1969)* **64**, 547-552 (1985).
230. Walderhaug, H., Hansen, F.K., Abrahmsen, S., Persson, K. & Stilbs, P. Associative thickeners: NMR self-diffusion and rheology studies of aqueous solutions of hydrophobically modified poly(oxyethylene) polymers. *J. Phys. Chem.* **97**, 8336-8342 (1993).

Acknowledgement

First, I thank Marc Baldus for the supervision of my doctoral studies. I am very grateful for his expert advice, the great environment and all his time and support.

I am indebted to J. Antoinette Killian (Utrecht University, The Netherlands), Stefan Becker (Max-Planck-Institute for Biophysical Chemistry, Germany), Dirk Görlich (Max-Planck-Institute for Biophysical Chemistry, Germany), Werner Maas (Bruker Biospin, USA), Olaf Pongs (University Hospital Hamburg-Eppendorf, Germany), Dirk Trauner (University of California, Berkeley, USA), and their coworkers Karin Giller, Erica C. E. Kremer, Iris Ohmert, Erica M. Wilson, Steffen Frey, Sönke Hornig, Vitya Vardanyan, and Phanindra Velisetty for fruitful cooperation and all their ideas, expertise and dedication.

I am grateful to Claudia Steinem, Rolf Boelens, Eike Brunner, Christian Griesinger, and Hans-Robert Kalbitzer for introducing me to NMR, supporting my studies and providing stimulating research environments. This work would not have been possible without outstanding teachers sharing their knowledge and fascination for science.

I thank my colleagues Gitta Angerstein, Henrike Heise, Marie Renault, Abishek Cukkemane, Itzam de Gortari, Manuel Etzkorn, Ashutosh Kumar, Adam Lange, Henrik Müller, Deepak Nand, Robert Schneider, Karsten Seidel, and Vinish Vadrian for their scientific contributions and for being such a marvelous team. Furthermore, I thank all members of the Department of NMR-based Structural Biology at the Max-Planck-Institute for Biophysical Chemistry and the NMR Spectroscopy Research Group at the Bijvoet Center for Biomolecular Research at Utrecht University for their support, friendliness, and the great time we shared.

I am grateful to Hans Wienk for helping me with the Dutch summary which is part of this thesis.

Financial support from the Stiftung Stipendium Fonds des Verbandes der Chemischen Industrie, the Max-Planck Society, DFG and NWO is gratefully acknowledged.

This thesis is dedicated with love and gratitude to my family and friends.

Curriculum vitae

Christian Ader was born on January 7, 1981 in Pforzheim, Germany. From October 2001 to July 2006, he studied biochemistry at the University of Regensburg, Regensburg, Germany and Wesleyan University, Middletown CT, USA. The Diploma thesis was performed under the supervision of Eike Brunner investigating nucleotide binding proteins by solid-state NMR spectroscopy (ssNMR). From October 2006 to July 2008, he worked as PhD student in the group of Marc Baldus at the Max-Planck-Institute for Biophysical Chemistry in Göttingen, Germany. The PhD work comprised ssNMR studies of selective membrane transport systems and was continued from August 2008 to September 2009 at the Bijvoet Center for Biomolecular Research at Utrecht University, Utrecht, The Netherlands.

List of publications

Listed are original and invited articles as well as unpublished manuscripts.

Iuga, A., Spoerner, M., **Ader, C.**, Brunner, E. & Kalbitzer, H. R. Rapid assignment of solution ^{31}P NMR spectra of large proteins by solid-state spectroscopy. *Biochem. Biophys. Res. Commun.* **346**, 301-305 (2006).

Iuga, A., **Ader, C.,** Gröger, C. & Brunner, E. Applications of solid-state ^{31}P NMR spectroscopy. *Annu. Rep. NMR Spectrosc.* **60**, 145-189 (2007).

Ader, C., Spoerner, M., Kalbitzer, H. R. & Brunner, E. Solid-state ^{31}P NMR spectroscopy of precipitated guanine nucleotide-binding protein Ras in complexes with its effector molecules Raf Kinase and RalGDS. *J. Phys. Chem. B* **111**, 2752 - 2757 (2007).

Ader, C., Schneider, R., Seidel, K., Etzkorn, M. & Baldus, M. Magic-angle-spinning NMR spectroscopy applied to small molecules and peptides in lipid bilayers. *Biochem. Soc. Trans.* **35**, 991-995 (2007).

Schneider, R., **Ader, C.,** Lange, A., Giller, K., Hornig, S., Pongs, O., Becker, S. & Baldus, M. Solid-state NMR spectroscopy applied to a chimeric potassium channel in lipid bilayers. *J. Am. Chem. Soc.* **130**, 7427-7435 (2008).

Ader, C., Schneider, R., Hornig, S., Velisetty, P., Wilson, E. M., Lange, A., Giller, K., Ohmert, I., Martin-Eauclaire, M. F., Trauner, D., Becker, S., Pongs, O. & Baldus, M. A structural link between inactivation and block of a K^+ channel. *Nat. Struct. Mol. Biol.* **15**, 605-612 (2008).

Ader, C., Schneider, R., Seidel, K., Etzkorn, M., Becker, S. & Baldus, M. Structural rearrangements of membrane proteins probed by water-edited solid-state NMR spectroscopy. *J. Am. Chem. Soc.* **131**, 170-176 (2009).

Seidel, K., Etzkorn, M., Schneider, R., **Ader, C.** & Baldus, M. Comparative analysis of NMR chemical shift predictions for proteins in the solid phase. *Solid State Nucl. Magn. Reson.* **35**, 235-242 (2009).

Ader, C., Pongs, O., Becker, S. & Baldus, M. Protein dynamics detected in a membrane-embedded potassium channel using two-dimensional solid-state NMR spectroscopy. *Biochim. Biophys. Acta, Biomembr.* **In press.**

Ader, C., Schneider, R., Hornig, S., Velisetty, P., Vardanyan, V., Giller, K., Ohmert, I., Becker, S., Pongs, O. & Baldus, M. Coupling of activation and inactivation gate in a K^+ channel: potassium and ligand sensitivity. *EMBO J.* **In press.**

Ader, C., Frey, S., Maas, W., Görlich, D. & Baldus M. Amyloid-like interactions within nucleoporin FG-hydrogels. **Manuscript under review.**

Ader, C., Becker, S. & Baldus, M. Membrane Associated Systems: Structural Studies by MAS NMR. *Encycl. Nucl. Magn. Reson.* **Manuscript under review.**

Poyraz, Ö., Schmidt, H., Seidel, K., **Ader, C.,** Delissen, F., Tenenboim, H., Goosmann, C., Brinkmann, V., Thünemann, A. F., Zychlinsky, A., Lange, A., Baldus, M., Griesinger, C., & Kolbe, M. Protomer refolding directs assembly of the type three secretion needle. **Manuscript in preparation.**

Ader, C. *et al.* The conformational stability of K^+ channel gating states depends on the lipid bilayer. **Manuscript in preparation.**